Johannes Gutenberg-Universität Mainz
Department Chemie

Single-atom gas chromatography studies on quartz glass to determine the volatility and reactivity of polonium

Master's thesis

To obtain the academic degree master of science

submitted by Katharina Hermainski

1. Examiner: Prof. Dr. Christoph Düllmann
2. Examiner: Prof. Dr. Michael Block

Ich, Katharina Hermainski, Matrikelnummer 2754560, versichere, dass ich meine Masterarbeit selbstständig verfasst und keine anderen als die angegebenen schriftlichen und elektronischen Quellen, sowie andere Hilfsmittel benutzt habe. Alle Ausführungen, die anderen Schriften wörtlich oder sinngemäß entnommen wurden, habe ich kenntlich gemacht.

I, Katharina Hermainski, matriculation number 2754560, certify that I have written my master's thesis independently and that I have not used any written and electronic sources or other aids other than those indicated. I have marked all statements that have been taken from other writings, either verbatim or in spirit.

Mainz, der 15.05.2024 K. Hermainski

Acknowledgements

First of all, I would like to thank my supervisor Prof. Dr. Christoph Düllmann for the opportunity to complete my master's thesis in his working group. I would like to thank you for the trust you have placed in me from the very beginning and for the many research opportunities you have given me. Without this support, I would have been denied an exciting field of research.

I would also like to thank Dr. Jochen Ballof for his detailed proofreading of my work. I am grateful that you took so much time and I am sure that your helpful and constructive comments have greatly improved this thesis. In addition, I would also like to thank you for your support regarding the experiments in Řež.
Furthermore, I would like to thank my second examiner, Prof. Dr. Michael Block, for taking the time to read and evaluate my thesis.

My special thanks also go to Dr. Alexander Yakushev and Dominik Dietzel for their guidance in my work and for always answering my questions. The professional discussions I was allowed to have with you were always very instructive and helped me to gain a deeper understanding of our research. Thank you very much for your support in the design and realisation of all the experiments conducted as part of this thesis.

I would also like to thank my czech colleagues from the Czech Technical University in Prague, especially Prof. Dr. Jan John and Dr. Pavel Bartl, as well as Prof. Dr. Jon Petter Omtvedt from the University of Oslo, for their professional support of our experiments in Řež. Without our collaboration, the thermochromatographic experiments carried out in this thesis would not have been possible.

Thanks also to Dr. Pavol Mošaťfor his professional and linguistic support during our beam time in Řež. Also, I would like to thank him and Dr. Jadambaa Khuyagbaatar for the setup of the COMPACT detector for the experiments with $^{216}\mathrm{Po}$.
For the technical assistance of the experiments, I would like to thank in particular Jörg Krier, who, despite a heavy workload, always found time to help with the realisation of the experiments carried out here.
For the preparation of the $^{224}\mathrm{Ra}$ source, I also want to thank Andrea Tzeitel Loria Basto, Christoph Mokry and Jörg Runke.

My very special thanks also go to my life companion and friend Michel Hindersin, who has always supported me throughout my entire studies, in both the good and bad times. I would like to thank him explicitly for his extensive support in writing the code for the Monte Carlo simulation.
I would also especially like to thank my parents for their intensive support throughout my studies. Thanks to you, as well as Michel Hindersin, there was always someone I could confide in.

Abstract

The underlying principles governing our current periodic table of elements are challenged by the influence of relativistic effects due to growing nuclear charge, especially in the heaviest, so-called superheavy elements (SHE). In order to better understand the influence of relativistic effects on the chemistry of all elements of the periodic table, the SHE and their homologues are analysed by gas chromatography. A first step towards the investigation of the chemically still uncharacterised element 116, livermorium, is the chemical analysis of its lighter homologue polonium. In this thesis, the adsorption enthalpy of elemental $^{204}\mathrm{Po}$ on quartz glass in helium was determined to be (-86 $\pm$ 5) kJ/mol through thermochromatography. On quartz glass with a high concentration of silanol groups, a chemical reaction of polonium with the surface was observed. The adsorption enthalpy of elemental $^{204}\mathrm{Bi}$ as the daughter of $^{204}\mathrm{Po}$ and the homologue of the superheavy element moscovium on quartz glass was determined to be $-157^{+6}_{-8}\,\mathrm{kJ/mol}$ during the same thermochromatography experiments. Isothermal studies of elemental $^{216}\mathrm{Po}$ revealed that the adsorption enthalpy of polonium on quartz and on Teflon is of a similar order of magnitude. The experiments carried out here thus lay the foundation for future chemical experiments with the superheavy element livermorium and help to better interpret the results of the chemistry experiments with moscovium, the heavier homologue of bismuth. The demonstrated surface reaction of polonium with quartz clearly underlines the importance of the knowledge of the exact surface structure for the interpretation of the data obtained, not only in chromatographic experiments with homologues but also with SHE.

Die grundlegenden Prinzipien, die unserem derzeitigen Periodensystem der Elemente zugrunde liegen, werden durch den Einfluss relativistischer Effekte aufgrund der zunehmenden Kernladung, insbesondere bei den schwersten, so genannten superschweren Elementen (SHE), in Frage gestellt. Um den Einfluss relativistischer Effekte auf die Chemie aller Elemente des Periodensystems besser zu verstehen, werden die SHE und ihre Homologen mit Hilfe von Gaschromatographie analysiert. Ein erster Schritt zur Untersuchung des chemisch noch uncharakterisierten Elements 116, Livermorium, ist die chemische Analyse des leichteren Homologen Polonium. In dieser Arbeit wurde die Adsorptionsenthalpie von elementaren $^{204}\mathrm{Po}$ auf Quarzglas in Helium durch Thermochromatographie auf (-86 $\pm$ 5) kJ/mol bestimmt. Auf Quarzglas mit einer hohen Konzentration von Silanolgruppen wurde eine chemische Reaktion von Polonium mit der Oberfläche beobachtet. Die Adsorptionsenthalpie des elementaren $^{204}\mathrm{Bi}$ als Tochter von $^{204}\mathrm{Po}$ und Homolog des superschweren Elements Moscovium auf Quarzglas wurde bei denselben Thermochromatographie-Experimenten als $-157^{+6}_{-8}\,\mathrm{kJ/mol}$ bestimmt. Isothermale Untersuchungen von elementarem $^{216}\mathrm{Po}$ ergaben, dass die Adsorptionsenthalpie von Polonium auf Quarz und auf Teflon in einer ähnlichen Größenordnung liegt. Die hier durchgeführten Experimente legen somit den Grundstein für zukünftige chemische Experimente mit dem superschweren Element Livermorium und helfen, die Ergebnisse der chemischen Experimente mit Moscovium, dem schwereren Homologen von Bismuth, besser zu interpretieren. Die nachgewiesene Oberflächenreaktion von Polonium mit Quarz unterstreicht deutlich die Bedeutung der Kenntnis der genauen Oberflächenstruktur für die Interpretation der erhaltenen Daten, nicht nur bei chromatographischen Experimenten mit Homologen, sondern auch mit SHE.

Contents

1

Introduction

Early on in the history of chemistry, chemists sought a regularity in the properties of the elements. One of the best-known concepts proposed was Dimitri Ivanovich Mendeleev's ordering of the elements according to atomic mass.[1] The breakthrough to our modern periodic table was then achieved by Mosley, who discovered the emission of characteristic X-rays by also with X-rays irradiated elements. Mosley was able to show that the wavelength of the emitted X-ray was dependent on an integer Z, which was identical to the number of protons of the element. From then on, the elements were no longer ordered by mass, but by this atomic number Z, which marked the birth of our modern periodic table.[2] The periodic table provides the basis for the description of periodic trends, such as the atomic radius or the ionization energy, and the sole positioning of an element allows important conclusions to be drawn about its chemical properties.[2,3]

As Z increases, another aspect that has often been dismissed in the past becomes increasingly important for the chemical properties of an element: Due to the higher nuclear charge in the atomic nucleus, the electrons with the probability of residing at the atomic nucleus (s- and $p_{1/2}$-electrons) move at ever higher velocities. This leads to a higher relativistic mass of these electrons and ultimately also to a change from the non-relativistic to relativistic orbitals.[4–9] The impact of these relativistic effects on chemical properties has often been neglected to this day, although many of the properties of lighter elements cannot be explained without taking these effects into account.[10,11] For instance, the most stable oxidation state of lead, the golden luster of gold and the presence of liquid mercury at room temperature can only be explained by the existence of relativistic effects.[12–16] Even the spectra of the lightest molecule H_2^+ cannot be fully explained without taking relativistic effects into account.[17]
In order to better understand the fundamental influence of relativistic effects on all elements of the periodic table, the study of superheavy elements (SHE) is particularly suitable due to the high nuclear charge of these elements. As SHE do not occur naturally on earth and often only have very short half-lives, they have to be produced atom by atom via heavy ion fusion. Consequently, the chemical study of SHE requires new approaches and strategies for experiments that enable the study of single-atoms.[4–9,18]

As a strategy for experiments with SHE, gas chromatography in columns with surfaces such as quartz or gold has proven to be particularly effective. Such experiments allow fast chemistry due to the ability of the atom to switch between the adsorbed and free state in the column quickly. With the help of simulations, the adsorption enthalpy can be extracted from the deposition temperature in the column as a measure of the volatility and reactivity of the element.[4–6,8,9,18–20]

The interpretation of the result of such chromatography experiments with SHE requires a sound knowledge of the chemical properties of the homologues of the investigated element in order to understand the influence of possible relativistic effects on the chemistry of SHE.[4–6,20] Therefore, in this thesis, polonium as a chemical homologue of element 116, livermorium, will be analysed with single-atom gas chromatography to pave the way for future investigations of the chemically yet uncharacterised superheavy element. For this purpose, the adsorption enthalpy of $^{204}\mathrm{Po}$, which was produced by fusion-evaporation reaction of $^{206}\mathrm{Pb}$ with $^{3}\mathrm{He}$, was determined on differently reactive quartz surfaces in different gas atmospheres.
The decay of $^{204}\mathrm{Po}$ made it possible to determine the adsorption enthalpy of the daughter $^{204}\mathrm{Bi}$ on quartz in helium, which is the homologue of the superheavy element moscovium.
In addition to the thermochromatography experiments with the long-lived $^{204}\mathrm{Po}$, isothermal chromatography experiments with the short-lived (145 ms)[21] $^{216}\mathrm{Po}$ gained from a $^{224}\mathrm{Ra}$ source were conducted on quartz glass and Teflon.

The investigations in this thesis offer insight into the chemistry of polonium as a homologue of livermorium. Additionally, they demonstrate the significance of the surface structure for gas chromatography, not only for the study of homologues but also for the study of SHE. The studies with $^{204}\mathrm{Bi}$ on quartz contribute to a better interpretation of the data of the superheavy element moscovium obtained by chromatography experiments.[22] The experiments carried out with $^{216}\mathrm{Po}$ on quartz and Teflon form the basis for the development of further apparatuses to better analyse the chemistry of this short-lived nuclide, as well as its superheavy homologue. Summarised, this thesis contributes to laying the groundwork for the first chemical investigation of the still chemically uncharacterised element 116, livermorium and adds to a better understanding of the chemistry of the superheavy element moscovium.

2

Theoretical background

2.1 Nuclear stability and production of the heaviest elements

2.1.1 Nuclear stability of (superheavy) elements

One of the most important properties of an atomic nucleus is the number of its neutrons and protons, as well as its mass, since the difference between the experimental mass and the sum of the masses of all nucleons represents the binding energy of the nuclide.[18,23] Knowledge of the mass is therefore of fundamental importance, not only for the stability of a nuclide, but also for predicting the energetics of nuclear reactions (see section 2.1.2) and spontaneous radioactive transformation processes, as transformation always leads to a change in binding energy (the so-called Q-value).[18] To describe the binding energy per nucleon and therefore the nuclear stability of a nuclide, mainly the liquid drop model (LDM) or the shell model, as well as variations of both models, are utilized.[18,23–25]

The liquid drop model

The liquid drop model was one of the first models to describe the binding energy of nuclei before the shell model (see below) became established.[5] As the name suggests, this model describes the atomic nucleus as an incompressible drop of liquid in which charge (protons) and mass are evenly distributed. It follows that all nucleons have the same distance to each other and the nuclear volume always remains the same during deformation.[18,23,24] The quantification of the binding energy is achieved within the LDM semiempirically using the Weizsäcker formula (equation 2.1), without taking quantum mechanics into account.[23,26]

$$B = \underbrace{c_V \cdot A}_{\text{volume}} - \underbrace{c_S \cdot A^{\frac{2}{3}}}_{\text{surface}} - \underbrace{c_C \cdot \frac{Z(Z-1)}{A^{\frac{1}{3}}}}_{\text{Coulomb}} - \underbrace{c_A \cdot \frac{(A-2Z)^2}{A}}_{\text{asymmetry}} + \underbrace{\delta}_{\text{pairing}} \text{ MeV} \tag{2.1}$$

Here, B is the binding energy, A is the mass, Z is the number of protons, the parameters c_V to c_A are proportionality constants obtained by mathematical fitting of empirical data and δ is the

pairing term.[23]
The first term of the equation, the *volume term*, reflects the attractive interaction between the nucleons within the nuclear volume.[18,23] The lack of binding partners on the surface of the nucleus and the resulting loss of binding energy is taken into account by the negative *surface term*.[18,23] The *Coulomb term* considers the Coulomb repulsion of the protons which lowers the binding energy inside the nucleus. The *symmetry term* reflects the stability of symmetric nuclei with the same proton and neutron numbers. The last term, the *pairing term*, takes the increased stability of nuclei with an even number of protons and neutrons (even-even-nuclei) and decreased stability of odd-odd-nuclei into account. This term is in principle of quantum mechanical origin but is only taken into account by an empirically derived expression and has no underlying physical explanation.[18,23]

When comparing the binding energies per nucleon predicted by the LDM and those derived from mass measurements, it is noticeable that the prediction of the LDM deviates strongly from the experimental results for certain proton and neutron numbers (see figure 2.1). Over time, in addition to the significantly increased stability of these nuclei, further experimental evidence for these "magic numbers" was found. This includes a high occurrence of nuclides with magic numbers in the universe and very high nucleon separation energies.[18,23–25] Since the binding energy per nucleon cannot be described by the LDM at these magic numbers, another model, the shell model, has to be utilized in these cases.

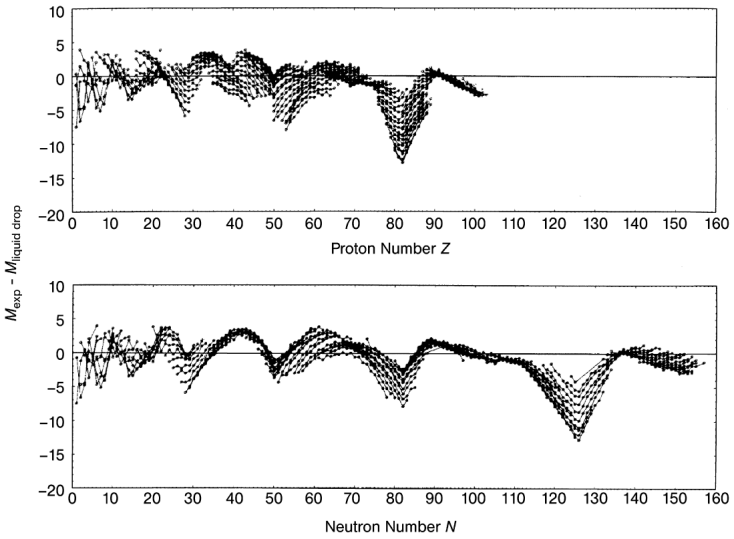

Figure 2.1: Deviation of the experimentally determined mass from the mass predicted by the LDM as a function of the proton number (top) and the neutron number (bottom, taken from [18], reprinted with permission from Wiley and Sons).

The nuclear shell model

The shell model replaces the interactions between individual nucleons with an averaged potential generated by the inert core nucleons that acts on each valence nucleon.[18,24] With a given potential, the Schrödinger equation can then be solved for the non-relativistic case. The nucleons

therefore populate shells in a similar way to the electrons surrounding the nucleus in an atom. Each nucleon can be described by an individual set of quantum numbers.[4,18,23] The principal quantum number n defines the shell, the orbital quantum number $\vec{l}$ determines the subshell with the names s, p, d, f and so on, the magnetic quantum number reflects the projection of the orbital angular momentum onto the nucleons in the corresponding orbital and the spin quantum number describes the intrinsic angular momentum of a nucleon.[23] In contrast to the LDM, each nucleon is therefore unique due to its own set of quantum numbers. As for electrons, the Pauli principle also applies to nucleons.[23]

Mayer and Suess solved the Schrödinger equation assuming a spherical, harmonic oscillator and were thus able to determine shell closures at the proton and neutron numbers 2, 8 and 20 which accounted for the increased stability of nuclides at these magic numbers.[27,28] However, higher experimentally observed magic numbers could not be explained yet.[18,23,25] In order to be able to explain the higher magic numbers with shell closures, the interaction between the orbital angular momentum and the spin of the nucleons, the so-called spin-orbit coupling (see section 2.2.1 for details), must also be taken into account.[24] This interaction results in a new quantum number $\vec{j}$, the total angular momentum, which in turn leads to a splitting of the nuclear levels, with which higher magic numbers can then also be explained.[23,25]

In the so-called independent-particle shell model (IPM) described above, the nucleons move almost independently of each other and the two-body interaction of the nucleons is only described via an averaged field. This approach is only strictly valid in the vicinity of the magic numbers.[18,25] Outside of magic numbers, further residual interactions, such as the attractive interaction between two paired nucleons, must be taken into account (transition to the interacting shell model).[24,25] Furthermore, the potential of a spherical harmonic oscillator is of course only applicable for spherical nuclides which occur around magic numbers.[24] For deformed nuclides, the Nilsson model can be used, which takes deformations into account via an additional quantum number Ω, which cancels the degeneracy of the individual $\vec{j}$-states.[18,24]

The existence of SHE

The existence of elements is, according to the LDM, limited by the half-life against spontaneous fission.[29,30] This half-life is in turn determined by the ratio of the long-ranged, repulsive Coulomb force between the protons and the short-ranged, attractive nuclear force between all nucleons.[5,8,18,30] Within the framework of the LDM, the stability against spontaneous fission can be determined via the fissility parameter X, which reflects the ratio between the Coulomb energy and the surface energy (see equation 2.1).[24,30] With increasing fissility parameters, the fission half-life determined with this model decreases sharply with Z in the region of the actinides and reaches 10^{-14} s for rutherfordium (Z = 104, see figure 2.2).[5,6,9,31] This time is regarded as the minimum lifetime for classifying an element, as it corresponds to the time an atom needs to form its electron shell.[4,32,33] Accordingly, the transactinides should not exist in the scope of the liquid drop model and the elements from rutherfordium onwards, called superheavy elements, therefore exist solely due to stabilizing nuclear shell effects.[5,6,29,32] The stabilisation against spontaneous fission is indeed so pronounced in this area that most of the

heaviest elements have a dominant α-decay branch in contrast to decay by spontaneous fission.[18]

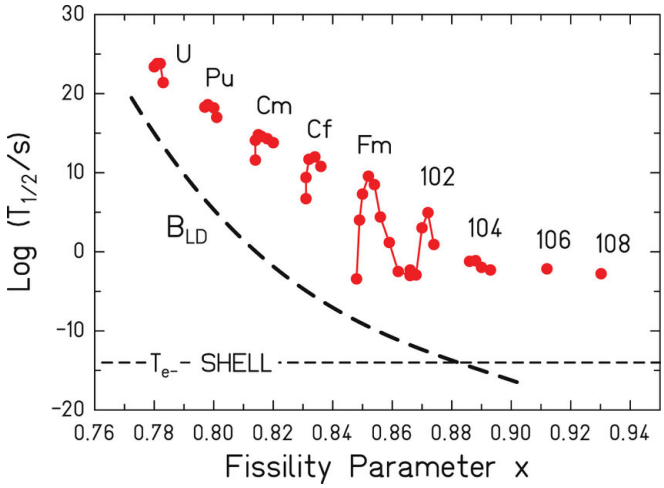

Figure 2.2: Experimentally obtained spontaneous fission half-lives of the even-even isotopes of the transuranium elements (red circles) in comparison to the spontaneous fission half-lives calculated with the fission barrier B_{LD} according to the liquid drop model (bold dashed line) plotted against the fissility parameters X. The time required to form the electron shell T_{e^-} is indicated as a dashed line (figure from G. Münzberg, 2004, see [34] and [35], reprinted with permission from Springer Nature).

According to the shell model, particular stability is attributed to nuclides with closed proton and neutron shells, which consequently raises the question of shell closures and thus increased stability in SHE as a form of "island of stability" in a sea of unstable, short-lived nuclei.[6] The first theoretical predictions by Myers and Swiatecki predicted shell closure at a proton number of 126 and a neutron number of 184.[4,8,29] Later, different modern calculations resulted in proton numbers of 114, 120 or 126, but confirmed the neutron number of 184.[6,8,29,36] Except for the proton number of 114 (flerovium), it has not yet been possible to produce nuclides with these predicted magic numbers. Although the element with the highest proton number (element 118, oganesson) is already in the vicinity of the predicted shell closure, the most neutron-rich nuclides in the current Karlsruher chart of nuclides (^{294}Ts and ^{293}Lv with N = 177, see figure 2.3) are still far away from the predicted magic number of 184.

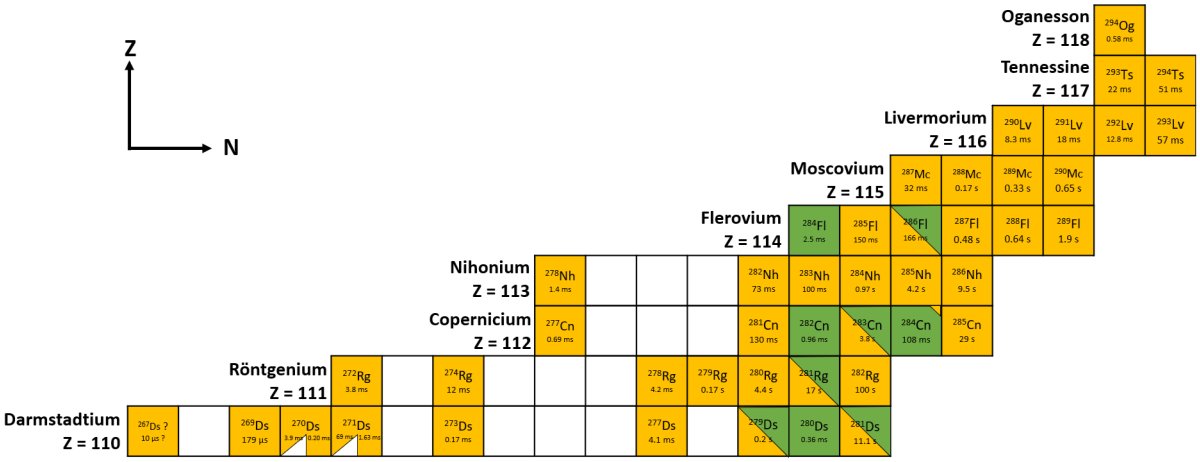

Figure 2.3: Excerpt of the chart of nuclides from element 110, darmstadtium, to the heaviest known element 118, oganesson. The colors correspond to those of the Karlsruher chart of nuclides (yellow: α-decay, green: Spontaneous fission, modified from [37]).

Today it is known from measurements (until element 102, nobelium) and predictions of electric quadrupole moments that most heavy nuclei are deformed and not spherical.[32,38] The previously named predicted shell closures (of which none could be determined experimentally yet) however always assume spherical nuclei. As briefly described in section 2.1.1, deformations according to the Nilsson model lead to a cancellation of the degeneracy of proton and neutron energy levels of spherical nuclides, resulting in further shell closures in deformed nuclei. This results in further predicted magic numbers for deformed nuclides at Z=108 and N=162, which connect the still undiscovered island of the SHE with the known elements and challenges the thought of an "island of stability" in a "sea of instability".[5,6,8,29–31,39] Where exactly the shell closures of the SHE are located, how long-lived the said nuclides with shell closures really are and where the end of the periodic table lies, remains unanswered to this day. Finding this answer is above all dependent on new technical developments in accelerator technology and new approaches for the synthesis of even heavier and more neutron rich elements and isotopes.[29,33,40]

2.1.2 Production of superheavy elements via heavy ion fusion

The production of elements heavier than uranium in a high-flux reactor by successive neutron capture and β^--decay ends with fermium, as there is no β^--unstable isotope of this element. Transfermium and superheavy elements must therefore be produced by (heavy ion) fusion at accelerator facilities by selecting a suitable target and projectile.[5,6,29]

Since heavy ion fusions are endothermic (negative Q-value), the kinetic energy of the projectile must be at least equal to the Q-value.[4,18,41,42] In addition, when a projectile approaches the target, the Coulomb repulsion between the two nuclei must also be taken into account. Classically, this Coulomb barrier must be exceeded by the kinetic energy of the projectile in addition to the Q-value in order to enable direct contact between the projectile and the target.[29,41–44] If the kinetic energy of the projectile is less than the Coulomb barrier, elastic and inelastic scattering are the main reaction pathways.[4,42]

When the distance between the two nuclei becomes sufficiently small, the short-range, attractive nuclear force takes effect forming a dinuclear system and individual nucleons can be exchanged at the contact point.[29,41–44] The number of collective nucleons, which can move in the nuclear volume of both formally individual nuclei, can increase until both nuclei have completely united and form the so-called compound nucleus (CN).[44] If the system fissions before the CN has formed, the process is referred to as quasi-fission which is one of the main hindrance factors to the synthesis of SHE.[29,43–45] The CN is an intermediate state in which, according to Bohr, the excess kinetic energy of the projectile is evenly distributed among all nucleons as excitation energy so that the nucleus formed is in thermal equilibrium.[18] This intermediate state between the entrance and the exit channel has a significantly longer lifetime (10^{-16} s) than the passing time of a nucleus (10^{-21} s).[18]
If the collision between the projectile and the target is not central, a rotation is induced and, in addition to the Coulomb barrier, an angular momentum barrier is created. The generated angular momentum is proportional to the so-called impact parameter b, which reflects the distance between the location of the impact on the target nucleus and its center. If the angular momentum of the CN is above the critical value L_{crit}, the CN can fission immediately after its formation to discard its excitation energy (fusion fission).[43]
In addition to dissipating the excitation energy by fission, the CN can also de-excite by emitting particles, preferably neutrons (as these are not confined by the Coulomb barrier), forming the so-called evaporation residue (EVR). This fusion-evaporation reaction leads to the production of the desired superheavy element. The evaporation of neutrons is a step-by-step process, whereby each evaporation competes to dissipating the excitation energy by fission.[9,29,41–44]

Each evaporated neutron contributes to a loss of approximately 10 MeV of excitation energy (8 MeV because of the binding energy and 2 MeV due to the kinetic energy of the neutron).[9] The competition between neutron evaporation and fission is won by the faster process, which in the majority of cases is fission. High excitation energies thus reduce the probability of survival of the CN, as this competition must be won more often.[9,29,41–44] Considering SHE, the macroscopic fission barrier disappears completely (see section 2.1.1) and the stability against fission is solely due to shell effects. In addition to the angular momentum and the Coulomb barrier, deformations must therefore also be taken into account for the synthesis of SHE, since increasing deformation leads to damping of the shell effects and thus a decrease in the fission barrier.[43,44]
The probability that the EVR is formed (expressed by the effective cross-section) can be summarised by equation 2.2.[9]

$$\sigma_{\mathrm{EVR}} = \sigma_{\mathrm{cap}} \cdot p_{\mathrm{CN}} \cdot W_{\mathrm{surv}} \tag{2.2}$$

Where σ_{cap} is the capture cross section (i.e. the probability that the projectile approaches the target in the range of the attractive nuclear potential), p_{CN} is the fusion probability with which the CN is formed and W_{surv} is the probability that the CN survives fission and becomes the EVR.[9]

In order to keep the excitation energy of the CN low (an approach called **cold fusion**), heavier projectiles and lead or bismuth targets are selected due to their smaller, meaning more negative,

binding energies.[46] Due to the low excitation energy between 10 and 20 MeV, fewer neutrons have to be evaporated until the CN has cooled down completely and thus the probability of survival against fission increases. However, since the Coulomb barrier is proportional to the product of the atomic number of the projectile and the target, the Coulomb barrier in these more symmetric reactions is large compared to hot fusion. Thus, the formation of the CN is less likely and quasi-fission becomes more favourable.[7,29,42–44]
An alternative strategy is **hot fusion**, in which lighter projectiles and heavy (actinide) targets are used. Although this strategy leads to a lower Coulomb barrier, the excitation energy of the CN is also significantly higher (40-50 MeV), and the survival probability of the CN decreases.[9,29,42–44] The probability of success of both fusion approaches, represented by the cross-section, decreases exponentially with the atomic number. This was remedied by using the doubly magic nucleus $^{48}\mathrm{Ca}$ as a projectile, which in turn led to the discovery of elements 112 to 118 (see also figure 2.3).[8]

Nuclides with sufficiently long lifetimes are essential for chemistry experiments with SHE. Hot fusions with nuclei that are as neutron-rich as possible are therefore used for such experiments as the nuclei produced in this way are closer to the β-stability line and therefore have longer half-lives.[9]

2.2 Chemistry of superheavy elements

2.2.1 Relativistic effects

Superheavy elements are not only interesting from a physical point of view due to their sole existence or the unique nuclear structures (rings, tori or (semi)bubbles),[32] but also for chemistry, as the ultimate test for the validity of the order of our periodic table for the heaviest elements, since the increasing influence of relativistic effects may fundamentally change their chemical behaviour.[6] Although these effects have long been dismissed as unimportant for valence electrons and thus for chemistry, they are indispensable even for the interpretation of chemical effects of lighter elements.[10–12,32] For example, the diverse oxidation states of the early actinides, the most stable oxidation state of lead, the golden luster of gold, the high rate constants of singlet-triplet transitions in 4d- and 5d-elements and even the spectra of the lightest molecule H_2^+ can only be fully explained by relativistic effects.[12–17,47] The three relativistic effects (direct and indirect relativistic effect, as well as spin-orbit coupling) scale approximately with the atomic number to the square, which is why the SHE are the elements with the most pronounced relativistic effects of the entire periodic table.[4–6,9]

In hydrogen-like atoms, the electron moves in a circular motion around the atomic nucleus according to Bohr's atomic model, if the centrifugal force and the Coulomb attraction are equal (equation 2.3).[9]

$$\frac{Ze^2}{4\pi\epsilon_0 r^2} = \frac{m_e v^2}{r} \tag{2.3}$$

Here, Z is the atomic number of the element, e is the elementary charge, ϵ_0 is the vacuum permittivity, m_e is the mass of the electron, v is the velocity and r is the radius of the circular

motion.
If the quantum mechanical condition $m_e v r = n\hbar$ is inserted into equation 2.3 and the equation is rearranged after r, it becomes clear that the radius of the circular motion of the electron is a function of its mass (equation 2.4).[12–14,48]

$$r = n^2 \cdot \frac{4\pi\epsilon_0\hbar^2}{Zm_e e^2} \tag{2.4}$$

This electron mass is in turn a function of the velocity at which the electron moves around the nucleus (equation 2.5).[12–14,48]

$$m_e = \frac{m_0}{\sqrt{1 - \left(\frac{v}{c}\right)^2}} \tag{2.5}$$

Where m_0 is the mass of the electron at rest and c is the velocity of light.
In order to maintain the circular motion around the nucleus even at high Coulombic forces (and correspondingly with large atomic numbers), the electron must move at ever greater speeds. The higher velocity causes the relativistic mass of the electron to increase, which in turn leads to a decrease in the radius of orbit. These effects accordingly lead to a contraction of those orbitals in which the electrons have a probability of residing at the atomic nucleus (s- and $p_{1/2}$-orbitals) which is called the **direct relativistic effect**.[8,13,14,32] For a long time it was believed that this contraction only affected inner orbitals and not those that play a role in chemistry.[10–12] However, this assumption is easily refuted by the high ionization energy of lead: Due to the contraction and thus subsequent energetic stabilization of the 6s-orbital, more energy must be applied to remove electrons from this orbital and the ionization potential increases. It follows that the most stable oxidation state of lead is +2 and not +4 as the main group of the element would suggest. This phenomenon is known as the inert-pair-effect and also applies to other elements such as thallium and tin.[12–14]

Due to the contraction of the orbitals near the nucleus, the positive charge of the atomic nucleus is more strongly shielded by the electrons in the contracted orbitals. The effective nuclear charge which is still perceptible from the orbitals without a probability of residing at the nucleus ($p_{3/2}$-, d- and f-orbitals) is therefore much lower than the real nuclear charge. These orbitals are thus no longer as strongly attracted to the atomic nucleus and expand, which leads to energetic destabilization (known as the **indirect relativistic effect**).[12–14]

The third relativistic effect is the **spin-orbit coupling (*SOC*)**, which leads to a splitting of the electron levels depending on the total angular momentum $\vec{j}$ if the orbital quantum number $\vec{l}$ is greater than zero. The total angular momentum is the vector sum of the orbital angular momentum and the spin and, in contrast to the last two, is still a good quantum number for heavy elements. The SOC is stronger for inner shells with the same orbital quantum number and decreases with increasing orbital quantum number for the same principle quantum number. For SHE, the splitting by the SOC reaches a similar magnitude as typical binding energies and is thus decisive for the chemistry of the heaviest elements. Consequently, the orbitals are no longer characterized by the orbital quantum number $\vec{l}$, but by the total angular momentum quantum number $\vec{j}$, which leads to the transition from non-relativistic to relativistic orbitals.[12–14,49]

2.2.2 Single-atom gas chromatography

General background

In classical chemistry, the equilibrium of a reaction is described by the law of mass action, which takes into account the activities or usually the concentrations of the species involved.[50] However, when investigating superheavy elements, only individual atoms can be studied due to the extremely low production rates and short half-lives.[4,7] It is of course not possible to specify the concentration in a specific phase for individual atoms, as the atom is either in the considered state or not. The solution to this problem is to use the probability of finding the atom in a particular phase instead of the concentration of atoms in the given state.[51,52] In order to determine the probability of the atom in a given phase with sufficient statistical certainty, the atom must be given the opportunity to switch quickly and frequently between the two states. This condition is given in chromatography processes in which the atom or molecule can alternate between a stationary phase and a gaseous or liquid mobile phase. For extremely short-lived nuclides (half-lives of seconds to a couple hundred milliseconds), the use of gas chromatography is particularly interesting due to the rapid separation and transport process, which can follow directly after the production of the nuclide.[4,5,19,20]
Especially for the study of superheavy elements, fully automated chemical apparatuses such as TASCA (Transactinide separator and chemistry apparatus) at the GSI Helmholtzzentrum für Schwerionenforschung have proven their worth, in which the element to be analysed is brought into the chromatography column directly after production and following physical pre-separation by rapid transport through gas jets (often by attachment to aerosol particles).[53,54] Detectors coated with gold or SiO_2 such as the COLD (Cryo online detector) or COMPACT (Cryo online multidetector for physics and chemistry of transactinides) detector are also frequently used in the analysis of SHE, as the detector can be used as the chromatography column at the same time.[4,6]
By adding reactive gases directly downstream of the target, (more volatile) species such as chlorides (utilized for the separation of $RfCl_4$),[55] oxides (utilized for the investigation of HsO_4)[56] or hydroxides can also be formed (see subsection below for a short summary of the conducted chemistry experiments of SHE). Since gas chromatography does not allow speciation of the analyzed species, the chosen chemical environment may only allow one chemical form.[4,6,19,20]

In gas chromatography, the atom or molecule moves on average along the gas flow of the inert carrier gas. If it collides with the surface of the stationary phase, it can be adsorbed if it loses its translational and internal energy and thus comes into equilibrium with the surface.[57,58] The ratio of the residence times in these two states depends on the adsorption enthalpy of the species under consideration, as well as the temperature and the column material. The mean time an atom or molecule spends adsorbed on the column wall $\bar{\tau}$ is described by the Frenkel equation[19,59,60]

$$\bar{\tau} = \tau_0 \cdot \exp\left(\frac{-\Delta H_{\mathrm{ads}}}{RT}\right), \tag{2.6}$$

where ΔH_{ads} is the adsorption enthalpy, R is the ideal gas constant, τ_0 is the period of oscillation of the atom or molecule on the surface and T is the temperature.[19,59,60]

The adsorption can either be of a physical (physisorption) or chemical nature (chemisorption).[50,57,58,60–64]

In **physisorption** (physical adsorption), the atom or molecule is bound to the surface by weak, long-range Van der Waals interactions (comparable to a condensation process). In this case, the strength of the interaction is primarily dependent on the polarizability of the adsorbed molecule/atom and the surface, as well as the distance between the interacting partners. Through physisorption, energy is released which manifests itself through vibrations in the crystal lattice of the solid phase. As the atom finds itself in a (shallow) potential well due to adsorption, desorption is always an activated process. In contrast to chemisorption, the molecule or atom retains its chemical identity.[50,57,60–62,64]
Chemisorption (chemical adsorption) leads to the formation of a chemical (often covalent) bond with the surface, mostly at those sites where the coordination number of the substrate can be maximised. The process may be dissociative, and/or involve the change of oxidation numbers or ligands which requires an energy barrier to be overcome (formation of a surface compound). The adsorption process is, compared to physisorption, irreversible and the desorbed compound has a chemically different form than the adsorbed one. Chemisorption is usually characterised by a significantly higher adsorption enthalpy (deeper potential well) and a shorter distance between the adsorbed atom and the surface. In most cases, it is an exothermic process, as the degrees of freedom decrease (negative entropy). Chemisorption is an elementary step for heterogeneous catalysis, which can follow this adsorption process.[50,57,60–64]
Figure 2.4 a) shows an one-dimensional plot of the potential energy against the distance to the surface to compare physisorption to chemisorption.

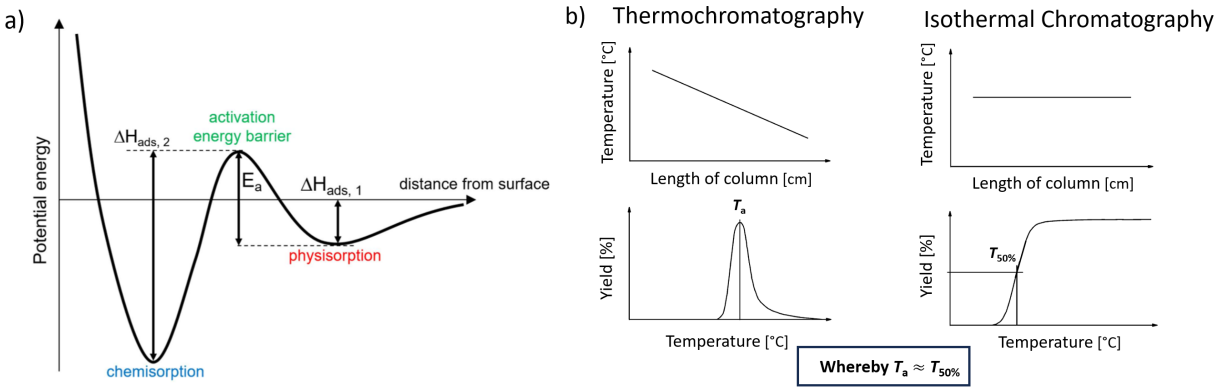

Figure 2.4: One-dimensional plot of the potential energy against the distance to the surface (a). The model shown assumes that an energy barrier E_a can be overcome after physisorption, which then leads to stronger chemisorption (taken from [65]). As well as comparison of isothermal and thermochromatography (b, modified from [4], reprinted with permission from ACS Publications. Copyright 2013 American Chemical Society).

The column material and the species under consideration are one of the decisive factors as to which type of adsorption is observed. Quartz glass and metal surfaces such as gold have proven to be particularly suitable as column materials, as they are non-reactive towards the carrier gases, but reactive towards the often volatile atoms or molecules in question.[4] The nature and chemical purity of the surface is of fundamental importance for determining the adsorption enthalpy and the type of adsorption, as the surface can differ locally to such an extent that different binding

sites on the surface have very different adsorption enthalpies.[50,64,66,67]
The exact relationship between physisorption and chemisorption is still not fully understood. The simplest model (see figure 2.4 left) assumes that a physisorbed atom or molecule can be chemisorbed by overcoming the energy barrier E_a.[50,62] However, further investigations indicate that an atom can also be trapped directly in a (metastable) chemisorption potential well, as this allows a large part of the atom's energy to be released more quickly by vibrational relaxation and equilibrium with the surface is reached faster.[57,58]

Two strategies, isothermal chromatography (IC) or thermochromatography (TC), can be used for the chemical studies of SHE in the gas phase.[4,5,19,20]
In **isothermal gas chromatography**, an inert carrier gas (mobile phase) flows through a column at a constant, i.e. isothermal, temperature. The adsorption enthalpy of the element or molecule determines how long it remains adsorbed on the stationary phase. If the species in question is adsorbed for a very long time, the atom or molecule decays in the column. The fraction of the atoms which pass through the column (called breakthrough) is measured and by repeating the experiment at different temperatures, an integrated chromatogram can be obtained. The half-life of the nuclide in question acts as a internal clock for the system, since at a breakthrough of 50%, the retention time of the species under consideration corresponds exactly to the half-life of the nuclide. The adsorption enthalpy can then be calculated from the known retention time and the temperature.[4,5,19]
Isothermal measurements require real zero measurements, which means very long measurement times, especially when investigating SHE. It must also be examined in depth whether a technical defect has caused the zero measurement. Alternatively, **thermochromatography** can be used to analyse the chemistry of SHE. In thermochromatography, an often negative temperature gradient is applied to the column. If the atom moves through the column, it is adsorbed at a certain temperature for so long that it decays there. The adsorption enthalpy can in turn be determined from this deposition temperature.[4,5,19,20]
Figure 2.4 b) shows a comparison of the two chromatographic methods described above.

Chemical studies of the heaviest elements

Since the first investigation of rutherfordium in the 1960s, chemical investigations of transactinides using the methods described above have now reached element 115, moscovium.[22] The studies of the last decades have contributed to a better understanding of the chemistry of the halides and oxyhalides of the elements rutherfordium (Z=104), dubnium (Z=105), seaborgium (Z=106) and bohrium (Z=107), as well as the oxyhydroxides and even the hexacarbonyl of seaborgium and the tetroxide of hassium (Z=108).[4,7–9,55,56,68] The elements copernicium (Z=112) and flerovium (Z=114), which were predicted to have a behaviour similar to that of noble gases due to their fully occupied s- and $p_{1/2}$-orbitals respectively, were investigated in elemental form by thermochromatography.[67,69] These investigations showed that the superheavy elements exhibited similarities with their lighter homologues, despite the strongly pronounced relativistic effects, which therefore underlines the structure of our current periodic table. However, the chemical properties of the elements meitnerium (Z=109), darmstadtium (Z=110), röntgenium (Z=111) and the 7p-elements from livermorium (Z=116) onwards remain unknown to this day, mainly because of the lack of long-lived isotopes for chemistry.[4,7–9]

2.2.3 Monte Carlo simulation

The determination of the adsorption enthalpy is no longer carried out using the ideal gas chromatography model based on the laws of molecular kinetics, but by using a Monte Carlo simulation according to Zvára.[59,60] Generally speaking, the Monte Carlo method is a statistical model based on random numbers which is based on the assumption that the behaviour of an ensemble can be represented by a large number of random samples. The main difficulty with this method is to determine the exact distribution of the parameters (normal distribution, uniform, exponential or other).[70]
In this case, certain variables such as the lifetime or the adsorption time on the column wall are sampled by random distributions. The experimental parameters such as the gas flow, temperature and pressure are defined as input parameters for the program and the adsorption enthalpy is varied until the best agreement between simulated and experimental data is achieved.[19,59,60]

A random lifetime is assumed for each simulated atom, which is determined according to an exponential distribution based on the half-life of the nuclide. In offline measurements where the column is scanned after the experiment with a detector, only those atoms can be measured whose lifetime corresponds to at least the experiment time. In this case, the lifetime corresponds to the duration of the experiment.[19,59,60]

During diffusion in the gas, the atom or molecule changes its flight vector with each collision with gas atoms, which is why diffusion can be understood as random flights which can be described by statistical theory. The diffusion coefficient is proportional to the frequency of the random directional changes and the mean length of one "jump" and can be understood as a measure of the mobility of the atom in the gas phase.[19,59,60] In this simulation, the diffusion coefficient D is approximated using the semi-empirical Gilliland formula (equation 2.7).[71]

$$D = \frac{0.0044 \cdot T^{\frac{3}{2}}}{p\left[\left(\frac{M_1}{\rho_1}\right)^{\frac{1}{3}} + \left(\frac{M_2}{\rho_2}\right)^{\frac{1}{3}}\right]^2} \cdot \sqrt{\frac{1}{M_1} + \frac{1}{M_2}}\ \mathrm{cm^2 s^{-1}} \tag{2.7}$$

Here, T is the temperature at the current position in the column, M is the molar mass and ρ is the density of the species under consideration or of the carrier gas.[59,60,71]
It is known that the diffusion coefficient is not exactly proportional to $T^{1.5}$ but the proportionality seems to vary between $D \propto T^{1.5}$ and $T^{1.7}$. Following, equation 2.7 has, in some occasions, an inaccurate temperature dependence. However, more accurate formulae require molecular parameters such as exact collision distances or collision integrals, which are often unknown.[60,72,73]

Depending on the gas flow and the diffusion coefficient, the atom travels a certain distance, called jump length, before it hits the wall for the first time. The average jump length can be calculated using equation 2.8.[19,59,60]

$$\bar{\eta} = (11 - 16\Re + 6\Re^2) \cdot \frac{Q}{24\pi D} \tag{2.8}$$

In this equation, $\Re$ is the ratio of the residence time in the gas phase to the total residence time in this column segment and Q is the gas flow rate.[19,59,60]

This equation is based on the consideration that the travelled distance of very probable short displacements are approximately equal to zero and that the long jumps have a significantly lower probability. The equation is only valid if laminar flow is given and longitudinal diffusion is neglected.[60]
Based on the average jump length, a random jump length is calculated (following and exponential distribution) until which the atom hits the wall and is adsorbed there. The simulation thus assumes that every collision with the surface leads to adsorption.

After each jump, the time that the atom has spent in the gas phase (called flight time) is calculated (equation 2.9) and both the position of the atom and the elapsed time are updated. If the elapsed time is greater than the lifetime (or if the position of the atom is greater than the length of the column) the iteration cycle is terminated and the position of the atom is saved.[19,59,60]

$$t_f = \frac{2\pi r^2 \cdot \eta_j}{\left(Q \cdot \frac{p_0}{p} \cdot \frac{T_{\text{start}}}{T_0}\right) + \left(Q \cdot \frac{p_0}{p} \cdot \frac{T_{\text{end}}}{T_0}\right)} \tag{2.9}$$

Where r is the radius of the column, η_j is the based on the mean jump length exponentially distributed random jump length, p is the pressure, T_0 and p_0 are the temperature and the pressure under standard conditions, T_{start} is the temperature at the beginning of the jump and T_{end} is the temperature at the end of the jump.[19,59,60]

After the jump, the atom is adsorbed on the wall and the mean adsorption time is calculated using the Frenkel equation (equation 2.6). The exact adsorption time is then exponentially distributed around the mean adsorption time due to the Boltzmann factor.[59,60] It is assumed that the frequency of the vibration of the atom or molecule on the surface depends solely on the nature of the surface. Possible temperature dependencies or translation energies of the atom in collision with the surface are neglected.

After the adsorption time has elapsed, the desorbed atom can, in principle, move in a random spatial direction due to random diffusion. As the atom is very close to the column wall, there is a high probability that it will hit the column wall again and will be adsorbed once more. In this Monte Carlo model, the average number of these collisions is expressed by equation 2.10.[19,59,60]

$$\bar{v} = \frac{\pi r^2}{Q \cdot \frac{p_0}{p} \cdot \frac{T_{\text{end}}}{T_0}} \cdot \sqrt{\frac{2RT_{\text{end}}}{\pi \cdot M}} \tag{2.10}$$

The mean number of collisions is then used together with the mean adsorption time of one adsorption and the mean jump length to calculate the duration of the entire adsorption cycle (equation 2.11).[19,59,60]

$$\tau = -\bar{v} \cdot \bar{\tau} \cdot \bar{\eta} \cdot \ln\left(1 - \text{random}\right) \tag{2.11}$$

Whereby *random* is a random number between zero and one.[19,59,60]
After the adsorption cycle, the passed time is again updated and compared with the lifetime.[59,60]
Figure 2.5 left shows the programme flow chart of the Monte Carlo method according to Zvára.

The Zvára method described above does not take into account the difference between physisorption and chemisorption and thus neglects the possibilities of forming new species through reactions with the surface. A corresponding extension of the Monte Carlo method was published in 2024 by D. Dietzel et al.[65] In this extension, it is assumed that a physisorbed atom or molecule can transition to the chemisorbed state by overcoming an energy barrier E_a (see figure 2.4 left). When the atom or molecule transitions to the chemisorbed state, the newly formed second species acquires a new adsorption enthalpy, with which it continues the adsorption-desorption cycle. The probability of penetrating the energy barrier is described by equation 2.12[65]

$$P \propto 1 - \left(1 - \exp\left(-\frac{E_a}{RT}\right)\right)^{\frac{\tau}{\tau_0}}, \tag{2.12}$$

where τ is the adsorption time of one adsorption cycle and τ_0 is the period of oscillation on the surface. The exponent thus describes the number of attempts to penetrate the energy barrier E_a. The term $\exp(-E_a/RT)$ is derived from the Boltzmann distribution and describes the probability that the energy barrier will be overcome in a single attempt because the energy of the atom is above the energy barrier. The counter probability to this case is described by the term $1-\exp(-E_a/RT)$ and corresponds to the probability that the energy barrier is never overcome. The counter probability to this scenario is then the probability that the barrier is overcome in at least one of the attempts. This is the expression shown in equation 2.12.[65]
The introduced extension of the Monte Carlo method thus allows the simulation of the adsorption enthalpy of the original species and the second species formed by surface reaction, as well as the energy barrier of this reaction (for the program flow chart see figure 2.5 b).

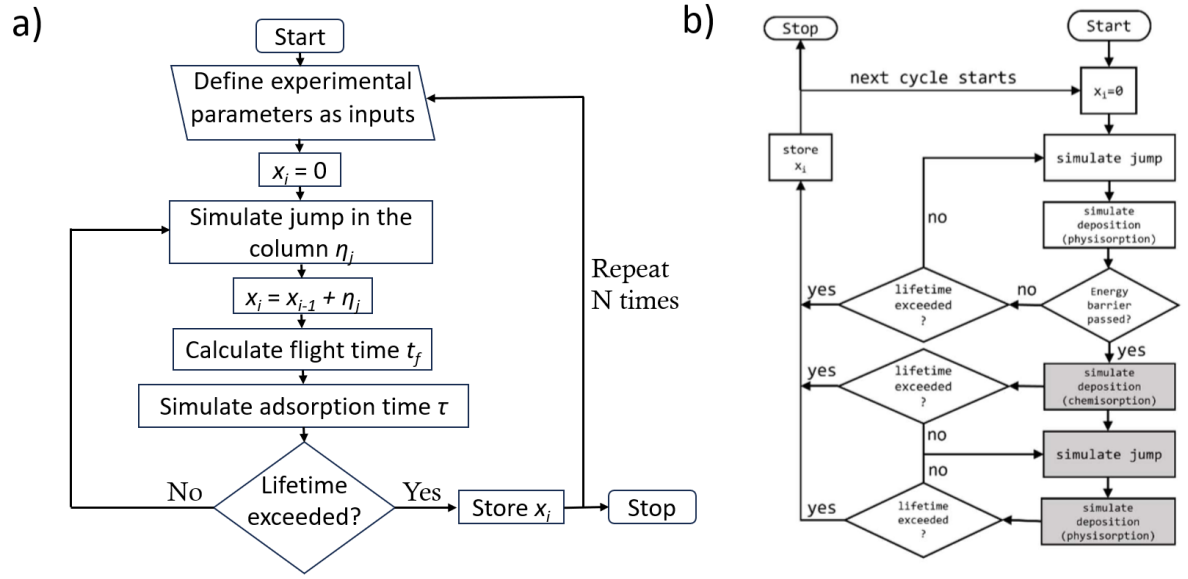

Figure 2.5: Program flow chart of the Monte Carlo method according to Zvára (a, here x_i is the current position in the column)[59] and the extended Monte Carlo method considering chemisorption and physisorption (b, taken from [65]).

2.3 The chemistry of polonium and bismuth

2.3.1 The chemistry of polonium

The discovery of polonium in 1898 by Marie Curie from the uranium ore pitchblende was the first time that non-visible quantities of an element were detected solely by its characteristic radiation (1 ton of pitchblende contain around 0.1 mg of polonium, earth's crust in total only consists of $3 \cdot 10^{-14}\%$ polonium).[74–76] Therefore, polonium is the first element of the periodic table that does not exist in macro quantities on earth which makes the study of the chemistry of the element significantly more challenging. A total of seven polonium isotopes occur in nature through the three still existing decay chains uranium, thorium and the actinium series, of which only $^{210}\mathrm{Po}$ is of relevance in nature due to its sufficiently long half-life (138.376 d, see figure 2.6).[75–78]

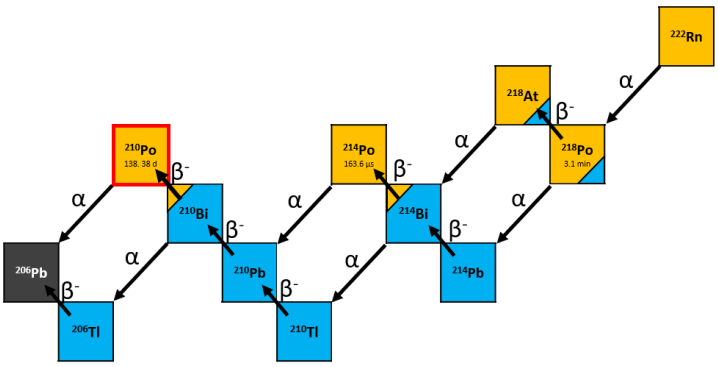

Figure 2.6: Excerpt from the uranium decay series in which three polonium isotopes occur. However, only $^{210}\mathrm{Po}$ is relevant in nature due to its longer half-life (highlighted with a red outline). The colors correspond to those of the Karlsruher chart of nuclides (blue: β^--decay, yellow: α-decay, black: stable).[37]

Polonium has a very high specific activity and is the most toxic, naturally occurring radionuclide.[76] The high toxicity not only leads to a hazard when handling polonium, it also contributes significantly to natural radiation exposure (accumulates in the spleen and the kidneys).[76,77] Polonium enters the atmosphere from the decay of $^{222}\mathrm{Rn}$ (from the uranium series) and through volcanic excavation and fracking as polonium dust.[76]
Not only the high toxicity contributes to the difficult handling of polonium but also the high specific activity which leads to self-heating of the specimens and thus influences temperature-dependent measurements, as well as the volatility of the element.[75,77] Furthermore, the high activity leads to defects in solids and the strong radiolysis leads to the destruction of solvents and unstable polonium compounds, as well as to the formation of oxidative radicals in water which leads to the oxidation of the specimen.[74,76,77,79–82]
Due to its high self-heating, polonium can be used as a heat source and for electricity production in satellites.[78] It can also serve as a neutron source together with elements that undergo (α, n)-reactions (such as beryllium).[74,75,83] Furthermore, polonium chemistry is relevant in accelerator driven systems (ADS) where lead-bismuth eutectics are used as coolants and spallation targets, as polonium is produced during operation.[84–86]
The study of the chemistry of polonium began when macroscopic quantities (milligrams) of

the isotope ^{210}Po were produced by irradiating ^{209}Bi inside a reactor.[75,77] Although the high specific activity of the isotope is not optimal for chemistry, the production of the longer-lived isotopes ^{208}Po (2.898 a) and ^{209}Po (125.2 a) would require significantly more effort.[77,87]

Polonium belongs to the group of chalcogens (group 16) and therefore has the (non-relativistic) electron configuration [Xe]4f^{14}5d^{10}6s^{2}6p^4.[74] The chemistry of the lighter homologous oxygen and sulphur is still non-metallic (these elements are insulators), but the metallic character increases down the group. The elements selenium and tellurium already have modifications with semiconductor properties and are therefore semi-metals, polonium is ultimately a metal and conducts electricity with a positive temperature resistance coefficient.[2,75,77,87–89] The melting and boiling temperatures within the group first rise to tellurium and then decrease again to polonium, which is typical for metals.[2] Furthermore, the trend towards metallic behaviour can be observed in the decreasing electronegativity and the first ionization energy.[74,81] The chemistry of polonium is very similar to that of the lighter homologue tellurium, as well as to the elements bismuth and lead of the same period which are particularly similar to polonium in terms of boiling temperature, melting temperature and density.[74,75,77,78,82,90]

Elemental polonium is a shiny silver-white metal that glows light blue in the dark due to its radioactivity.[90] The metal occurs in two allotropic phases: The α-phase, which is stable at room temperature, crystallizes in a cubic-primitive crystal lattice with a density of 9.2 g/cm^3 that is otherwise only found in the high-pressure modifications of phosphorus and antimony, and the high-temperature rhomboedric β-Phase.[74,77,78,81,88,90] The phase transformation to β-Po takes place at 36 °C with a 3% increase in volume, but due to the decay heat both phases coexist between 18 and 54 °C.[74,75,80] In contrast to the lighter homologues, polonium does not form ring (sulphur) or chain structures (selenium and tellurium) and the complexity of the structures decreases down the group.[74]
The element occurs in the oxidation states -2 (as polonide), 0, +2, +4 and +6, with the +4 oxidation state being the most stable.[2,74,76,78,87] The reduction potentials at low oxidation levels are comparable to copper, at higher oxidation levels they are similar to precious metals.[79,81] The proof of the inert-pair effect (increased occurrence of lower oxidation states due to relativistic effects, see section 2.2.1) is difficult in the case of polonium, as only the first ionization energy is known.[74]

The stability of the dimer bond decreases within the group due to the increasing atomic radius and the associated increase in bond length, still, Po_2 could be detected spectroscopically.[74,80,87] Consequently, polonium in the gaseous state can be monoatomic or dimeric. For the lighter homologues, the dimeric species dominate in the gas phase, for polonium, the dimerization equilibrium is also assumed to be on the side of the dimer.[78,80]

Polonium is, like selenium and tellurium, a highly reactive element that forms compounds with most of the elements of the periodic table (see figure 2.7 for an overview).[74] In contrast to the lighter homologues, the element is dissolved in a hydrochloric acid solution to form the pink Po^{2+}-ion, which in turn emphasizes its metallic character.[74,78] Polonium is a soft element according to the HSAB (hard and soft acids and bases) concept. Investigating the chemical properties is difficult due to the comparatively high volatility of the element.[76]

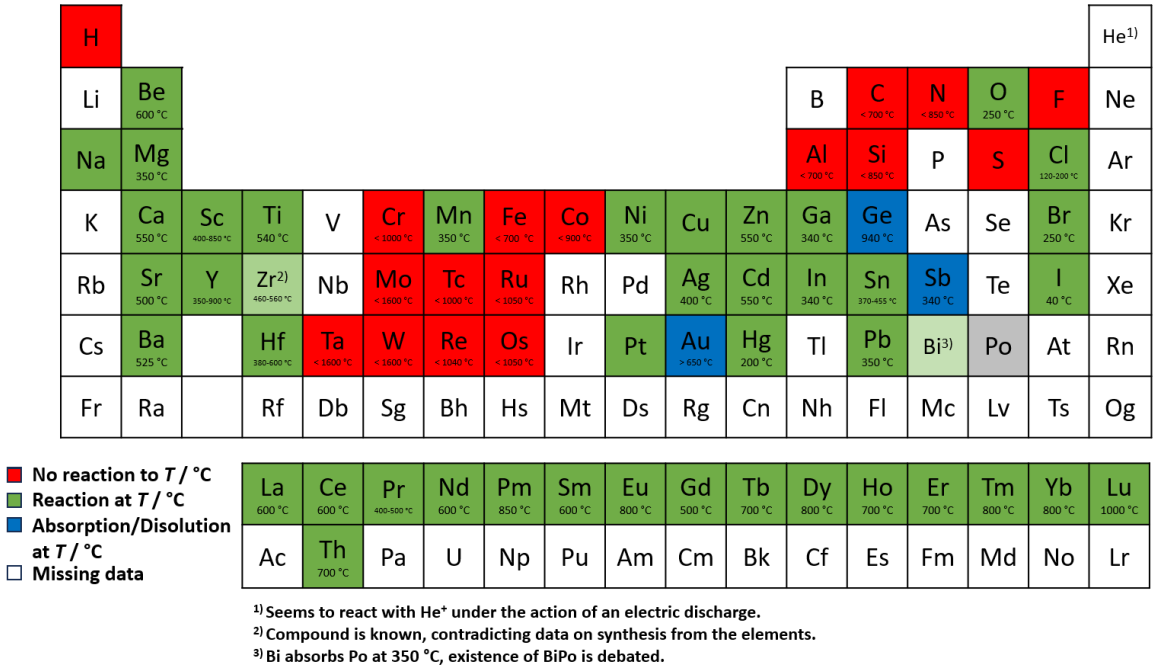

Figure 2.7: Schematic representation of the possible reactions of polonium with other elements.[87]

Polonides

Polonium occurs with more electropositive partners in the oxidation state -2, the compounds of this class are called polonides.[74,78] The reaction to form the polonides occurs at moderate temperatures (400-1000 °C) in the absence of air from the elements. In contrast to selenium and tellurium, polonium does not react with aluminium, gold, molybdenum, tantalum and tungsten. Crystal structures are known for most polonides, and are often isomorph with the selenides and tellurides.[74,75,77,90] However, the polonides seem to be more ionic in character compared to the corresponding tellurides.[77] Similar to the tellurides, the polonides are expected to have very low stability in aqueous solution.[77] In addition, most polonides dissociate at moderate temperatures and all polonides are rapidly oxidized in air, presumably due to α-radiolysis.[77] Some examples of polonides include MgPo (NiAs structure), the highly volatile HgPo (NaCl type), lead and alkaline earth polonides of the form XPo (NaCl structure), Na_2Po (CaF_2 type) and $PtPo_2$ ($Cd(OH)_2$ structure), among others.[74,75,78,87,90]

Polonium hydride

The reaction to the chalcogen hydrides from the elements becomes increasingly endothermic down the group, so that the reaction to the polonium hydride from the elements already has a reaction enthalpy of over 100 kJ/mol.[78,82] Thus, it is not possible to produce the hydride from the elements. Instead, polonium hydride can only be obtained by reduction with nascent hydrogen (addition of magnesium to hydrochloric acid) in traces under light and oxygen exclusion.[78,82] The stability of the hydrides decreases within the group of chalcogens due to the increasing atom size and thus increasing bond length. Added to this is the decreasing electronegativity: While selenium still has a higher electronegativity than hydrogen, the electronegativity to tellurium decreases so much that the bond is almost completely non-polar and covalent. The

electronegativity drops even further towards polonium, so that the H-Po bond has a polar character again with a slight positive charge on the polonium.[74] Thus, the compound is know to be thermally very unstable.[75] H_2Po is a liquid at room temperature with a boiling point of 36.1 °C and a melting point of -35.3 °C, the compound is known to be volatile.[75,82,87,90]

Polonium oxides and hydroxides

Polonium is the only element of the chalcogenides for which, in addition to the trioxide and dioxide, the monoxide can also be isolated.[75,78] The compound is produced by radiolysis from $PoSO_3$ or by adding NaOH to aqueous solutions of Po^{2+}.[74,75,78] The black compound is easily oxidized.[74,75]
The most stable oxide is PoO_2, which is already slowly formed from the elements at room temperature in air. The reaction proceeds very rapidly above 250 °C.[74,77,78,81] Furthermore, the dioxide can also be obtained by thermal decomposition of the Po(IV) hydroxide, nitrate, sulphate or selenate.[74,75] PoO_2 has a yellow, face-centred-cubic (fcc) low-temperature modification and a red tetragonal high-temperature modification.[74,75,77,81] The phase transformation between the two modifications is reversible, the oxygen content can vary in the low-temperature modification.[90] Polonium dioxide can be sublimated at 885 °C from a metal surface in an oxygen stream and decomposes into the elements at 500 °C at reduced pressure. The compound is slowly reduced in a hydrogen stream at 200 °C.[74,75,77,90] Polonium dioxide is insoluble in water (slightly soluble in basic aqueous solution) and behaves amphoterically and metallic in contrast to TeO_2 and SeO_2 (essentially acidic behaviour).[78,81] Polonium trioxide and polonium dioxide are the anhydrides of polonium acid and polonic acid respectively.[78] Many metal oxides, including Bi_2O_3, V_2O_5 and Fe_2O_3 are known to absorb polonium dioxide (forming dimeric compounds, for example $Bi_2O_3 \cdot PoO_2$) at higher temperatures.[77] Oxidation of polonium dioxide with hydrogen peroxide forms the polonate $PoO_4{}^{2-}$.[78]
The trioxide could previously only be produced in trace amounts by electrolysis with strong oxidizing agents.[74,75,79,90]

Polonium dihydroxide forms as a dark brown precipitate when a base (aqueous ammonia or diluted NaOH) is added to an aqueous Po^{2+}-solution.[74,75] The divalent hydroxide is easily oxidized.[74] It reacts basic and possibly weakly acidic and is the only known chalcogen(II) hydroxide.[75,78]
The yellowish tetravalent hydroxide precipitates from basic Po^{4+}-solution and has an acidic character. It is probably not possible to produce $Po(OH)_4$ by heating the dioxide with KOH, as polonides are formed.[74]
The amphoteric polonic acid H_2PoO_3 and the polonium acid $PoO_3 \cdot aq$ (no exact structure known) cannot be synthesized by dissolving the corresponding anhydrides in water, as they are not soluble. Instead, the oxygen acids can be prepared by adding bases to aqueous polonium solutions.[75,78]

Polonium halides

All divalent and tetravalent halogenides of polonium are known, yet only the hexafluoride is known in the hexavalent state.[74,78] The divalent and tetravalent halides, as well as the hexafluoride, can be prepared by direct halogenation from the elements. Alternatively, the

divalent halides can also be obtained by dehalogenation of the tetravalent halides (for example by heating the tetrachloride with SO_2).[74,75,78] The tetravalent halides decompose in the heat to the corresponding divalent halide and molecular halogen.[78] In general, the formation tendency of halides increases from fluoride to iodide, while the formation tendency of the tetrahalides increases from sulphur to polonium.[78] In an aqueous solution, an excess of the corresponding halide can also form complexes of the form $[PoX_5]^-$ and $[PoX_6]^{2-}$.[78]
No oxohalides are known for polonium, instead the partly unstable mixed halides $PoCl_2Br_2$, $PoCl_2I_2$ and $PoBr_2I_2$ are reported.[74]

Other known compounds

A large number of other polonium compounds are known. These include the sulphide, whose insoluble properties in water were exploited in the discovery of the element,[76] the carbonate, which is the only stable carbonate of the elements selenium, tellurium and polonium, a large number of nitrates, as well as phosphates, sulphates and the half-metallic selenates and tellurates.[74,78] The iodate, chromate, vanadate, sulphoxide and selenium oxide, as well as some organometallic compounds, have also already been prepared.[74,75] Due to the presence of polonium in the environment, the aqueous chemistry was also investigated in detail, whereby further polonium oxyhydroxide and hydroxyhalide complexes were identified.[76]
Another compound found is PoCO. The homologues selenium and tellurium react with carbon monoxide at 400 and over 400 °C respectively, and there are indications of a similar reaction with polonium leading to PoCO.[74]

Previous gas chromatographic studies of polonium

Gas chromatographic analyses of polonium have so far mainly been carried out on various metal surfaces, whereas the analysis on quartz still requires further experiments.[84–86,91,92]
One of the first thermochromatographic studies of polonium was carried out in 1979 by B. Eichler et al. in a quartz column lined with copper foils. An adsorption enthalpy of (-157 ± 9) kJ/GA (gram atom) was found for the deposition of ^{210}Po on copper in helium.[91] Subsequent isothermal investigations by H. Gäggeler et al. confirmed this enthalpy in helium on copper in the area of the error ((-181 ± 21) kJ/mol) and further investigations on silver, gold, palladium and platinum in helium using ^{211m}Po were also carried out. The most positive enthalpy was found on silver ((-165 ± 11) kJ/mol), and the most negative enthalpy on palladium ((-290 ± 8) kJ/mol). In this study, the enthalpy on quartz glass was also investigated and found to be (-123 ± 11) kJ/mol.[92] In a three-part study by E. A. Maugeri et al., the deposition of ^{206}Po in thermochromatography experiments was first investigated on gold, then on platinum, silver and palladium and finally also on stainless steel in various gas atmospheres.[84–86] The adsorption enthalpy on gold in helium was in agreement with the publication by H. Gäggeler et al. within the range of the error ((-246 ± 7) and (-253 ± 7) kJ/mol were found in two experiments). In wet and dry hydrogen, an about 50 kJ/mol more negative adsorption enthalpy was found. In wet and dry oxygen, the enthalpy was found to be around -230 kJ/mol.[84] Compared to the publication by H. Gäggeler et al., enthalpies by several 10 kJ/mol more negative were measured on the metals platinum, silver and palladium in helium by E. A. Maugeri et al.[85] On stainless steel (SS316L), a comparatively low absolute value of the adsorption enthalpy of (-146 ± 6) kJ/mol was measured in dry helium.[86] None of the above-mentioned studies discuss the possible for-

mation of polonides during the experiment. In an older study from 1980 by S. Hübener et al., the adsorption enthalpy of trace amounts of polonium in a titanium column was determined to be (-330 ± 30) kJ/mol. The high adsorption enthalpy was explained by the formation of titanium polonides on the surface of the column.[93]
The short-lived isotope ^{216}Po (145 ms)[21] has also been investigated on quartz glass by A. Vogt et al., where an enthalpy of -85 kJ/mol was found in isothermal studies (no error given).[94]
Table 2.1 shows an overview of all measured adsorption enthalpies of polonium on the different surfaces in helium only.

Table 2.1: Adsorption enthalpies of polonium (all in kJ/mol, unless marked with *) measured by gas chromatography in different studies on different surfaces in helium.

	B. Eichler et al.[91]	H. Gäggeler et al.[92]	E. A. Maugeri et al.[84–86]	S. Hübener et al.[93]	A. Vogt et al.[94]
copper	-157 ± 9*	-181 ± 21	-	-	-
silver	-	-165 ± 11	-216 ± 7	-	-
gold	-	-224 ± 11	-207 ± 7 and -214 ± 7	-	-
palladium	-	-290 ± 8	-340 ± 7	-	-
platinum	-	-187 ± 21	-246 ± 7 and -253 ± 7	-	-
quartz	-	-123 ± 11	-	-	-85
stainless steel	-	-	-146 ± 6	-	-
titanium	-	-	-	-330 ± 30	-

* adsorption enthalpy is given in kJ/GA

2.3.2 The chemistry of bismuth

Bismuth is located in the periodic table in the pentele group and has the non-relativistic electron configuration [Xe]4f^{14}5d^{10}6s^{2}6p^3. The element occurs with electropositive partners mainly in the -3 oxidation state and with more electronegative partners mainly in the +3 oxidation state, although other oxidation states like +1 and +5 are also known. However, due to the inert-pair effect, the oxidation state +5 forms less easily with bismuth and its lighter homologue arsenic than with phosphorus or antimony. The existence of the bismuth monocation Bi^+ can also be attributed to relativistic effects.[2,78,81]
Metallic bismuth has a hexagonal-rhombohedral low-temperature structure in the solid state with a density of 9.78 g/cm^3 and a cubic body-centred high-temperature modification. The melting temperature is 271.3 °C and the boiling temperature is 1580 °C. In the melt and in the gas phase, the element is present as Bi_4.
Bismuth conducts electricity and is very brittle. Down the group of pentelides, the tendency to form multi-bonds and element-element single bonds decreases, whereas the tendency to form clusters within the group increases. This is reflected in the complex structures of bismuth cations

such as Bi_5^+ (quadratic pyramid) or Bi_5^{3+} (trigonal bipyramid).
Bismuth only dissolves in oxidizing acids to form Bi^{3+}-salts. The most common coordination numbers of the element are 3, 4, 5 and 6, rarely the coordination number 2 is also found (as for example in the organometallic compound bismabenzene).[2,78,81]

Bismuth is used in low-melting alloys for electrical fuses or safety closures, in pharmaceutical products with an antispetic or astringent effects, and as a heat transfer agent in nuclear technology.[78]

Bismuth hydride

As with polonium, the reaction to form the hydride of bismuth BiH_3 is highly endothermic and the synthesis can only be carried out electrochemically. Just like polonium, BiH_3 is also thermally unstable and decomposes at temperatures above -45 °C.[2,78,81]

Bismuth oxides and hydroxides

The oxide Bi_2O_3 occurs in nature as monoclinic bismite and slowly precipitates from basic bismuth salt solutions. The compound can also be produced by heating elemental bismuth in the presence of oxygen, whereby the bismuth burns in a blue flame. The oxide is basic and does not dissolve in water and bases, but only in acids. When dissolved in oxidizing acids, the corresponding oxygenic acid $H_3BiO_3 \cdot 3\,H_2O$, can be formed. The salts of this oxygenic acid are called bismutites.
In addition to the trioxide, the bismuth pentoxide Bi_2O_5 is also known, which can be produced in an impure state by the action of strong oxidizing agents such as H_2O_2 on aqueous Bi_2O_3 suspensions at temperatures of 80-200 °C.[2,78,81]

Other known compounds

A large number of other bismuth compounds such as various halides (all trihalides, as well as the monohalides BiBr and BiI, the pentafluroide and other low-valent halides such as Bi_6Cl_7), nitrates, sulfates and other chalcogenides (the sulfides, selenides and tellurides) are known.[2,78,81]

Previous chromatographic studies of bismuth

As for polonium, chromatographic analyses of bismuth were limited to metal surfaces and still lack investigations on SiO_2.
In the same study in which the deposition of polonium on gold was investigated by E. A. Maugeri et al., the daughter of ^{206}Po, ^{206}Bi, was also investigated on gold in helium, hydrogen and oxygen atmosphere. Very similar adsorption enthalpies of (-273 $\pm$ 7) kJ/mol and (-269 $\pm$ 7) kJ/mol were found in helium and hydrogen respectively. An adsorption enthalpy of at least -340 kJ/mol was measured in oxygen.[84] In the study by H. Hübener et al., the deposition of trace amounts of bismuth in titanium columns was also measured. Here, an adsorption enthalpy of at least -335 kJ/mol was determined. As with polonium, the enthalpy was explained by the formation of the intermetallic compounds Ti_4Bi and Ti_3Bi on the surface.[93]
In contrast to polonium, theoretical calculations were carried out by V. Pershina et al. for the

adsorption of bismuth (and the superheavy element moscovium) on Au(111) and on a hydroxylated silica surface. Using the computation suite ADF BAND, an adsorption enthalpy of -280 kJ/mol (revPBE-D3BJ) could be calculated on gold and an enthalpy of -153 kJ/mol (revPBE) and of -172 kJ/mol (revPBE-D3BJ) on SiO_2. For the superheavy homologue moscovium, significantly lower adsorption enthalpies were calculated (-58 kJ/mol on SiO_2 and -205 kJ/mol on Au(111)) due to pronounced relativistic effects.[95]
Table 2.1 shows an overview of all measured adsorption enthalpies of bismuth on the different surfaces in helium only.

Table 2.2: Adsorption enthalpies of bismuth (all in kJ/mol) measured by gas chromatography in different studies on different surfaces.

	E. A. Maugeri et al.[84]	S. Hübener et al.[93]	V. Pershina et al.[95]
gold	-273 $\pm$ 7	-	-280 (revPBE-D3BJ)
quartz	-	-	-153 (revPBE) and -172 (revPBE-D3BJ)
titanium	-	$\leq$ -335 kJ/mol	-

3

Experimental

A summary of all experiments carried out with experiment abbreviations and the most important experimental parameters can be found in the appendix in table 7.2.

3.1 Experimental setups

3.1.1 Setup for thermochromatographic studies of ^{204}Po and ^{204}Bi on quartz glass

The setup used for thermochromatography can be roughly divided into three segments which are described in more detail below. In the first segment, the carrier gas used is purified using several cartridges. A reactive gas can be added to the carrier gas and the flow can be controlled via several mass flow controllers.
The second segment of the setup includes the chromatography column and multiple ovens to bake out the catcher foil containing the products produced overnight and to set the temperature gradient. The column can be cooled to room temperature at its end using a water cooling system. An activated carbon filter and a mass flow meter are located behind the column in the last section of the setup. After passing the experiment, the gas is fed into a fume hood.
The whole experimental setup is shown in figure 3.1.

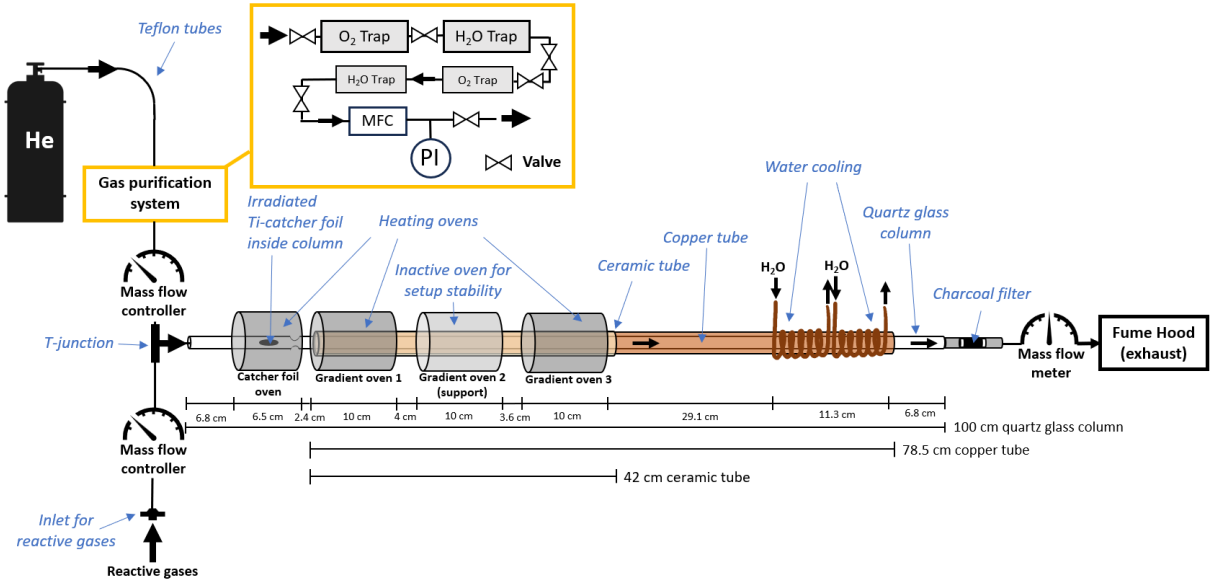

Figure 3.1: Setup of the thermochromatography apparatus for determining the adsorption enthalpy of ^{204}Po and ^{204}Bi on quartz glass in different gas atmospheres. An enlargement of the gas purification system is shown with a yellow outline. All cartridges used to purify the carrier gas are shown in grey. One mass flow controller (MFC) and a pressure indicator (PI) are installed in the gas purification system.

The carrier gas in the thermochromatography setup used here is helium (Linde, purity $\geq 99.9999\%$), which is purified through several cartridges (Spectromol Oxysorb (efficiency $H_2O < 30$ ppb, efficiency $O_2 < 5$ ppb); Spectromol Hydrosorp (efficiency $H_2O < 20$ ppb); Agilent Technologies, Big Moisture Trap, Model BMT-4 (efficiency < 5 ppb); Agilent Technologies, Big Oxygen Trap, Model BMT-4 (efficiency < 1 ppb)) to capture the impurities water and oxygen. The helium flow through the column is adjusted via a mass flow controller (MKS, Legacy Mass Flow Meter) downstream of the cartridges which is controlled by a digital power supply and read out unit (MKS, PR400B). The mass flow controller is followed by a T-junction through which a reactive gas can be added to the helium via a ball valve. The flow of this reactive gas can be adjusted via a second mass flow controller (MKS, Legacy Mass Flow Meter) upstream of the T-junction. Both gases (helium and if wanted a reactive gas) enter the quartz glass column through Teflon capillaries or capillaries made of stainless steel. All connections are done with Swagelok compression fittings made of stainless steel.

The polonium (mostly ^{204}Po but also ^{205}Po) was produced overnight at the cyclotron of the ÚJV in Řež by irradiating an enriched ^{206}Pb target (PbS, thickness 2.3 µm, area density ≈ 350 µg/cm^2, 99.51% enrichment) with ^{3}He (beam energy 50 MeV without any attenuation, about 47 MeV in the center of the target; beam current 300-500 nA), the recoils of the reaction were collected in a catcher foil (titanium, 2.5 µm). After irradiation, the catcher foil was placed directly in the thermochromatography column where it could be heated by a furnace (in the following called catcher foil oven). Since part of the produced ^{204}Po decayed before the experiment to ^{204}Bi, it was also possible to analyse the adsorption of the daughter of polonium. The quartz glass column used for thermochromatography is 100 cm long with an inner diameter of (4.0 ± 0.2) mm and an outer diameter of (6.0 ± 0.2) mm. The quartz glass column used

for the determination of the adsorption enthalpy of polonium on quartz glass in pure helium atmosphere has a constriction at 12 cm to prevent the catcher foil from slipping due to the helium flow, all other columns used do not have this constriction.
The oven that heats the catcher foil is followed by three more ovens, the first and third of which are used to set the temperature gradient. The second furnace is not heated, but is used solely to stabilize the column (all heating ovens from Heraeus Hanau; type B/A 1,7/10; maximum temperature 900-1200 °C). The ovens can be operated via associated control elements (Elektro-Automatik, Power Supply EA-PS 2042-20 B), the temperature is set by varying the applied voltage. To enable a smooth temperature gradient, the quartz column is inserted into a 78.5 cm long copper tube beginning at the first gradient oven after the catcher foil furnace, which can transport the heat from the ovens along the column. To further improve the gradient, the quartz column with copper pipe is again inserted into a 42 cm ceramic tube, which is only located at the hot end of the column. Two copper tube-coils with a length of 5.8 cm each through which water flows are attached at the end of the copper tube, to cool the column to room temperature.

An activated charcoal filter is located downstream of the column to collect any activity that was not deposited in the column. To be able to identify gas leaks, a mass flow meter (Merck, Aalborg Digital Mass Flow Meter) follows this activated carbon filter. The gas flowing through the column is finally fed into a fume hood after passing through the experiment.

3.1.2 Setup for isothermal measurements of ^{216}Po on quartz glass and Teflon

The setup for isothermal chromatography consists of a closed gas loop system in which several cartridges and mass flow controllers are installed to clean and control the gas flow. The $^{216}\mathrm{Po}$ activity is supplied from a $^{224}\mathrm{Ra}$ source built into the gas loop. The $^{220}\mathrm{Rn}$ formed from the decay of $^{224}\mathrm{Ra}$ is transported with the gas flow into a decay volume in which it can decay to $^{216}\mathrm{Po}$. The activity is then passed through the chromatography column and the COMPACT detector. The setup is explained in more detail below.
Figure 3.2 shows the whole setup schematically.

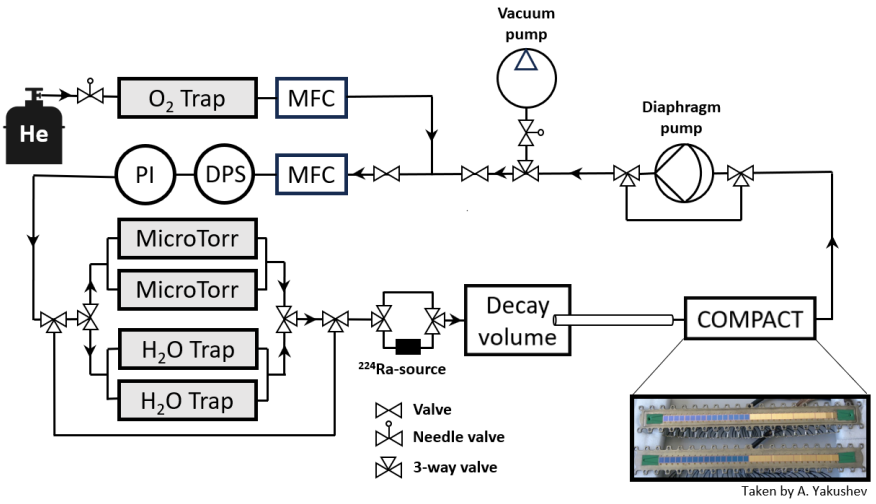

Figure 3.2: Experimental setup of the isothermal chromatography of ^{216}Po. Two mass flow controllers (MFC), a dew point sensor (DPS) and a pressure indicator (PI) are installed in the gas loop system, all cartridges used to purify the carrier gas are shown in grey. Below right a photo of the COMPACT detector is depicted (taken by A. Yakushev, GSI).

The carrier gas in this experiment is helium (Nippon Gases, purity $\geq$ 99.996%), which is purified using a gas loop system with several cartridges (Agilent Technologies, Big Oxygen Trap, Model BMT-4 (efficiency < 1 ppb); Agilent Technologies, Big Moisture Trap, Model BMT-4 (efficiency < 5 ppb); Saes Pure Gas, Inc., MicroTorr, model MC-400-902FV). A diaphragm pump (Fisher Scientific, Welch, type FB65452) ensures continuous circulation of the gas in the loop. The flow is controlled by two mass flow controllers (MKS, Legacy Mass Flow Meter). A dew point sensor (Michell Pura, PUR-TX-OEM-STD-120) and a manometer (Baratron, Capacitance Manometer) installed in the gas loop are used to measure the dew point and the pressure in the system. In this experiment however, the dew point was outside the scale (-120/-40 °C) of the measuring device.

The ^{224}Ra source, which supplied the ^{216}Po activity through the decay of ^{220}Rn, is installed downstream of the cartridges. The source was obtained by the decay of the naturally occurring nuclide ^{228}Th, which was sorbed on a cation exchange column. A solution of ^{224}Ra was gained by elution of the cation exchange column with 7 M HCl. The solution was then pipetted onto a glass microfibre filter and finally dried to serve as the source for the experiments.
A filter (Swagelok; particulate, inline welded filter; particle size $\geq$ 5 µm) behind the source prevents activity other than ^{220}Rn from being transferred to the experiment. The ^{220}Rn activity is then transported with the gas flow through PTFE (polytetrafluoroethylene) tubes and capillaries made of stainless steel into a 50 mL volume, where the activity can decay to ^{216}Po. Either a PTFE capillary can be connected directly as a chromatography column, or a quartz tube can be inserted into the decay volume (outer diameter (6.0 ± 0.2) mm, inner diameter (4.0 ± 0.2) mm). All connections are made using Swagelok compression fittings made of stainless steel. A COMPACT detector is used downstream of the column to detect the breakthrough of activity through the chromatography column. The gas can be pumped out of the system using a vacuum pump (Pfeiffer Vacuum, Adixen ACP40, multi-stage roots).

The COMPACT detector was originally developed for experiments with element 108, hassium, and combines the chromatography column for chemistry experiments with the detection.[96] The detector consists of two metal panels made of INVAR (alloy of nickel and iron) and therefore has a very low thermal expansion. A 10 mm wide, 36 mm long and 0.5 mm deep notch is incorporated into each panel, which holds 32 PIPS (passivated implanted planar silicon, 1x1 cm^2 in size, 300 µm thickness) detectors each. The two panels can be joined together vacuum-tight using indium wire, creating a 0.5 mm high channel.[96] In this experiment, the surface of the first 16 PIPS diodes was coated with SiO_2, and the surface of the last 16 diodes was coated with gold. The geometric efficiency of the detector to register an α-particle emitted from a species residing inside the column is estimated to be 75-80%.[96]
The COMPACT detector is used here exclusively for detection and not as a chromatography column, as only the breakthrough through the separate chromatography column is to be measured in the isothermal measurement carried out. In figure 3.2, a picture of the COMPACT detector used for the experiment is shown.

3.2 Procedures

3.2.1 Thermochromatographic studies of ^{204}Po and ^{204}Bi on quartz glass

Determining the adsorption enthalpy of ^{204}Po and ^{204}Bi in pure helium atmosphere (Rez2023-Po204-Bi204-TC-He)

First, the furnaces for the temperature gradient (not the furnace for baking out the catcher foil) were preheated to the desired temperature (maximum temperature (720 ± 20) °C) by regulating the applied voltage (for measured temperatures see table 7.5 to 7.7 in the appendix, for voltages see table 3.1).

Table 3.1: Voltage applied to the ovens to set the temperature gradient for the experiments Rez2023-Po204-Bi204-TC-He and Rez2023-Po204-TC-H2.

Oven	U / V
Catcher foil oven	32.00 V
Gradient oven 1	25.10 V
Gradient oven 2	-
Gradient oven 3	13.80 V

After setting the temperature gradient, a column which was previously annealed at 1000 °C in an inert gas atmosphere was inserted in the experiment and the temperature was measured from first the cold (with gas flow on) and then hot side (with gas flow turned off) of the column using a 50 cm long thermocouple (Type-K, read-out unit: Omega, HH801B). A γ-spectrum of the catcher foil that had been irradiated overnight at the cyclotron at ÙJV in Řež was measured using a HPGe-detector (ORTEC, GMX20P4-70, for relative efficiencies see appendix figure 7.1) which was calibrated beforehand with an ^{152}Eu source (using a linear function). The catcher

foil was then placed in the column (about 2 h after the end of irradiation) so that it was in the middle of its corresponding oven. The oven to heat out the catcher foil was adjusted to the desired temperature by setting the voltage on its control element. At the same time, the helium flow (50 sccm/min) was started via the mass flow controller. The catcher foil was then baked for 2 h with the gas flow running. During heating, the temperature of the ovens and the gas flow were constantly monitored. The flow rate measured at the mass flow meter behind the column fluctuated between 50 and 52 sccm/min during the experiment. As the system is open to the fume hood, atmospheric pressure can be assumed in the experiment.

After 2 h, the column was removed from the ceramic and the copper pipe (and therefore from the ovens) and both ends of the column were sealed. The column was left to cool for a few minutes and was then broken into forty-four (2.0 ± 0.2) cm pieces up to the position of the catcher foil (88 cm from the cool end). The individual column pieces, as well as the charcoal filter and the catcher foil after heating were measured with the HPGe-Detector with surrounding lead shielding to reduce the background. While the γ-spectra were being recorded, a second quartz glass column was installed in the experiment and the temperature gradient was measured again every two centimetres as described above using the thermocouple (for measured temperatures see table 7.5 to 7.7 in the appendix).

Determining the adsorption enthalpy of ^{204}Po in helium and hydrogen atmosphere (Rez2023-Po204-TC-H2)

Before the experiment, a 40% hydrogen and 60% helium mixture (Linde, purity hydrogen $\geq 99.999\%$, purity helium $\geq 99.996\%$) was connected to the gas inlet for reactive gases. A new quartz column without pre-treatment was inserted in the experiment. All ovens (not just the ovens for the gradient) were then preheated to the same temperature as in the previous experiment (for exact voltages see table 3.1). After the temperature gradient was established, it was measured quickly using the 50 cm thermocouple to confirm that the temperature did not change compared to the first experiment (Rez2023-Po204-Bi-204-TC-He).
A new catcher foil which was irradiated overnight was again placed in the same position as during the measurement in pure helium in the quartz column (about 2 h after the end of irradiation). Following, the mass flow of the hydrogen-helium mixture was set to 12.5 sccm/min at the mass flow controller for reactive gases and the mass flow of the pure helium was set to 37.5 sccm/min. With these mass flows, a total fraction of about 10% hydrogen could be achieved in the column. Again, the temperature of the ovens and the gas flow was monitored during the experiment. The measured gas flow behind the column was 55 sccm/min.

After 1.5 h, the column was removed from the heat, sealed, and again broken into forty-four (2.0 ± 0.2) cm pieces which were measured by the HPGe-detector. Finally, the charcoal filter and the catcher foil after heating were measured as well.

Determining the adsorption enthalpy of ^{204}Po in helium and oxygen atmosphere (Rez2023-Po204-TC-O2)

The reactive gas used in this experiment was oxygen (Linde, purity $\geq 99.995\%$) which was connected to the inlet for reactive gases. A new quartz tube without pre-treatment was installed

in the experiment and the ovens were preheated to a hotter temperature gradient with a maximum temperature of (1030 ± 20) °C in the catcher foil oven (for oven voltages see table 3.2).

Table 3.2: Voltage applied to the ovens to set the temperature gradient for the experiment Rez2023-Po204-TC-O2.

Oven	U / V
Catcher foil oven	36.20 V
Gradient oven 1	27.00 V
Gradient oven 2	-
Gradient oven 3	18.97 V

After the temperature gradient was established, a new catcher foil which was irradiated overnight was placed in the center of the catcher foil oven (7 h after irradiation) and the gas flow rate for oxygen was set to 5 sccm/min and the flow for helium was set to 45 sccm/min. With these settings, a total fraction of 10% oxygen was achieved in the column. Again, the gas flow and the temperature was controlled during the experiment. The measured gas flow behind the column fluctuated between 54 and 56 sccm/min.

After 1 h, the column was removed from the ovens, sealed, and again broken into forty-four (2.0 ± 0.2) cm pieces which were then measured with the HPGe-detector. It was observed that the titanium catcher foil was yellowish-white in colour after the experiment. This can be attributed to the formation of titanium oxides, most likely the formation of the dioxide. Finally, the charcoal filter and the catcher foil after heating were measured as well. During the γ-measurements, a new quartz column was installed in the experiment. After the temperature in this column reached thermal equilibrium, it was measured every two centimetres with the 50 cm thermocouple from first the cold end (with gas flow on) and then the hot end (without gas flow). For the measured temperatues see table 7.5 to 7.7 in the appendix.

3.2.2 Isothermal measurements of ^{216}Po on quartz glass and Teflon

Direct catch of ^{216}Po after the decay volume (GSI2024-Po216-IC-DC)

Before the experiment, the COMPACT detector was calibrated using α-particles of ^{215}Po (E_α = 7386.2 keV, I_α = 100%) and ^{219}Rn (E_α = 6819.1 keV, I_α = 79.4%) from an ^{227}Ac source (using a linear function).[21]
In order to determine how much activity reaches the chromatography column after the decay volume, the COMPACT detector was connected directly to the decay chamber with a PTFE capillary as short as possible (about 4 cm). The gas flow rate was set to 2900 sccm/min, the pressure in the gas loop was measured to be (1250 ± 6) hPa.
The activity reaching the detector was then measured for 1 h and 50 min. During the experiment, the pressure and the gas flow were constantly monitored.

Isothermal measurements of ^{216}Po on quartz glass (GSI2024-Po216-IC-Quartz)

Before the experiment, the gas loop was evacuated and re-filled with new helium. A 34 cm long quartz capillary which was previously annealed at 1000 °C in an inert gas atmosphere and with an outer diameter of (6.0 ± 0.2) mm and an inner diameter of (4.0 ± 0.2) mm was inserted into the decay volume and connected to the COMPACT detector with a short Teflon capillary (about 4 cm). The gas flow rate was set to 2900 sccm/min, the pressure in the gas loop was measured to be (1252 ± 6) hPa.
The activity reaching the detector was then measured for 1 h and 50 min. During the experiment, the pressure and the gas flow were constantly monitored.

Isothermal measurements of ^{216}Po on Teflon (GSI2024-Po216-IC-Teflon)

Before the experiment, the gas loop was evacuated and re-filled with new helium. A 34 cm long PTFE capillary with an outer diameter of (6.0 ± 0.2) mm and an inner diameter of (4.0 ± 0.2) mm was connected to the decay volume and to the COMPACT detector. The gas flow rate was set to 2900 sccm/min, the pressure in the gas loop was measured to be (1260 ± 6) hPa.
The activity reaching the detector was then measured for 1 h and 30 min. During the experiment, the pressure and the gas flow were constantly monitored.

4

Results

As part of this thesis, the adsorption enthalpy of polonium on quartz glass that was annealed at 1000 °C under inert gas atmosphere prior to the chromatography study in helium (section 4.1.2), as well as in helium/hydrogen and helium/oxygen atmosphere on non-pretreated quartz was determined (sections 4.1.4 and 4.1.5 respectively). In addition, it was possible to determine the adsorption enthalpy of bismuth on previously annealed quartz glass in pure helium atmosphere due to the ^{204}Bi formed from decay of ^{204}Po (section 4.1.3).
In isothermal measurements of ^{216}Po, the adsorption enthalpy on quartz glass previously annealed at 1000 °C under inert gas atmosphere (section 4.2.1) and on PTFE (section 4.2.2) in helium could be determined.

4.1 Thermochromatographic studies of ^{204}Po and ^{204}Bi on quartz glass

4.1.1 Identification of produced nuclei

Polonium was produced for the thermochromatography experiments by bombarding an enriched ^{206}Pb target with ^{3}He, the recoils were collected in a catcher foil behind the target (for details of the production see section 4.1.3). Two hours after the end of irradiation, a γ-spectrum of the catcher foil was measured (see figure 4.1 top). After the thermochromatography experiment, another γ-spectrum of the catcher foil was measured (figure 4.1 bottom). The γ-measurements are only provided to identify the produced nuclei.

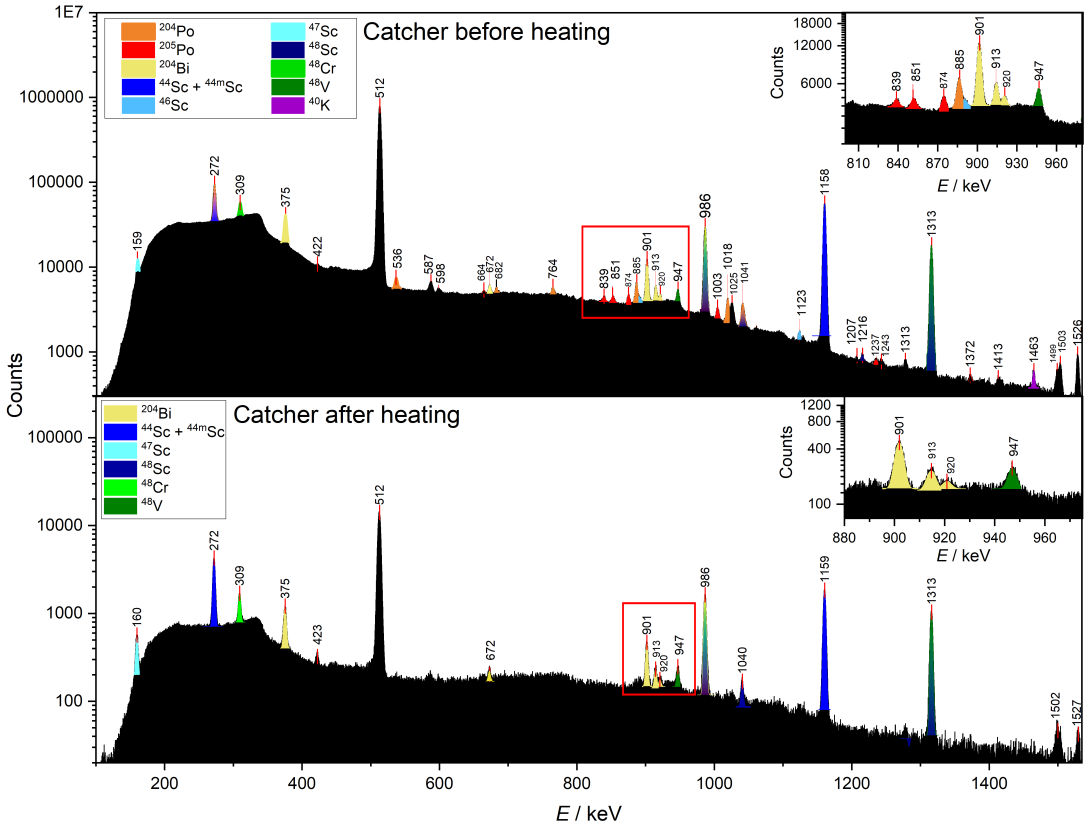

Figure 4.1: γ-spectra of the catcher foil after overnight irradiation. The upper spectrum shows the catcher before heating, the lower spectrum after heating. The measured γ-lines were assigned to isotopes using reference [21]. Multicoloured peaks symbolise the overlap of the γ-lines of multiple isotopes (this applies to the following lines: 272 keV (^{44m}Sc, ^{204}Po), 986 keV (^{204}Bi, ^{48}V, ^{48}Sc), 1041 keV (^{204}Bi, ^{48}Sc) and 1313 keV (^{48}V, ^{48}Sc), all γ-lines of ^{48}Sc overlap with the peaks of other isotopes). The peaks shown in black could not be conclusively assigned to any isotopes. The insets show an enlargement of the areas of the spectrum marked in red outline

The shift of the annihilation peak (511 keV) to slightly higher energies shows that the energy calibration is not exact. Consequently, it can be expected that all peaks are shifted to slightly higher energies. This was taken into account for assigning the γ-lines.

Due to the lack of experimental data in the desired energy range (experimental data is only available for this reaction at beam energies of 80 to 100 MeV),[97] the yields of the products of the reaction were calculated with the software LISECute++ (Code PACE4, Michigan State University) for beam energies of 50-46 MeV to be able to assign the γ-lines better. Here, 50 MeV corresponds to the maximum beam energy without attenuation, the beam energy in the center of the target should be about 47 MeV. Table 4.1 shows the yields of isotopes produced in the reaction of ^{206}Pb with ^{3}He with yields above 3% at different beam energies. As the target was not pure ^{206}Pb but also contained traces of the isotopes ^{207}Pb (0.31%) and ^{208}Pb (0.09%), the yields of the products of the reaction with ^{3}He with these target atoms were calculated as well (see table 7.3 in the appendix). These calculations were used solely to support the assignment

of the γ-lines and should not be used to accurately determine the cross sections of the respective reaction.

Table 4.1: Calculated yields and cross-sections for the reaction of $^{206}\mathrm{Pb}$ with $^{3}\mathrm{He}$ at various beam energies E_B using the software LISECute++ (Code PACE4, Michigan State University). The table only shows isotopes with yields above 3%. Here, σ symbolizes the cross-section.

Target	E_B / MeV	produced isotope	yield / %	σ / mb
$^{206}\mathrm{Pb}$	50 MeV	$^{204}\mathrm{Po}$	15.7	246
		$^{203}\mathrm{Po}$	62.5	979
$^{206}\mathrm{Pb}$	49 MeV	$^{204}\mathrm{Po}$	22.3	348
		$^{203}\mathrm{Po}$	57.3	895
$^{206}\mathrm{Pb}$	48 MeV	$^{204}\mathrm{Po}$	28.6	445
		$^{203}\mathrm{Po}$	51.9	519
		$^{201}\mathrm{Pb}$	3.2	49.8
$^{206}\mathrm{Pb}$	47 MeV	$^{204}\mathrm{Po}$	35.5	550
		$^{203}\mathrm{Po}$	43.7	677
		$^{201}\mathrm{Pb}$	4.4	68.2
$^{206}\mathrm{Pb}$	46 MeV	$^{204}\mathrm{Po}$	45.5	702
		$^{203}\mathrm{Po}$	34.0	525
		$^{201}\mathrm{Pb}$	3.8	58.6

According to the calculation, the isotope $^{203}\mathrm{Po}$ should have the highest yield at all beam energies expect for 46 MeV with $^{206}\mathrm{Pb}$ as the target atom. However, this isotope could not be found in the γ-spectrum. The reason for this is probably the rather short half-life of the isotope (36.7 min), which leads to almost complete decay at the time of measurement. The daughter of $^{203}\mathrm{Po}$, $^{203}\mathrm{Bi}$ with a half-life of 11.76 h, was also not observed in the catcher foil. The reason for this could be the absence of very strong γ-lines compared to the similarly long-lived isotope $^{204}\mathrm{Bi}$ (the most intense γ-line of $^{203}\mathrm{Bi}$ is at 820 keV with an intensity of 30%, the most intense γ-line of $^{204}\mathrm{Bi}$ is at 901 keV with an intensity of 98%) or that the code is not able to predict the yields accurately enough.[21,37]
With lower beam energies, the yield of $^{203}\mathrm{Po}$ decreases and the yield of $^{204}\mathrm{Po}$ increases, as the compound nucleus receives less excitation energy and therefore has to evaporate fewer neutrons. This isotope can be seen in the γ-spectrum of the catcher foil (orange peaks).
$^{205}\mathrm{Po}$, whose γ-lines are highlighted in red in figure 4.1, is calculated to be produced in yields lower than 3%. The fact that the γ-lines of this isotope are quite strong despite the very low calculated yields can probably be explained by the fact that the target material was not pure $^{206}\mathrm{Pb}$, but also contained traces of the isotopes $^{207}\mathrm{Pb}$ and $^{208}\mathrm{Pb}$.[37] The calculations show that the reaction of $^{3}\mathrm{He}$ with $^{207}\mathrm{Pb}$ produces both $^{204}\mathrm{Po}$ and $^{205}\mathrm{Po}$ as the main products, with $^{204}\mathrm{Po}$ being produced in higher yields at all beam energies. At lower beam energies, the yield of $^{205}\mathrm{Po}$ increases due to the decrease in the excitation energy of the CN. The reaction of $^{3}\mathrm{He}$ with $^{208}\mathrm{Pb}$ produces both $^{206}\mathrm{Po}$ and $^{205}\mathrm{Po}$, with $^{205}\mathrm{Po}$ being the main product at all beam energies. Again, the yield of the more neutron-rich isotope is favoured by lower beam energies. $^{206}\mathrm{Po}$ could not be seen in the γ-spectrum of the catcher foil, probably because of the low proportion of $^{208}\mathrm{Pb}$

in the target material. Therefore, ^{205}Po and ^{204}Po were the only polonium isotopes produced in high enough yields to be seen in the γ-spectrum.

In addition to the polonium isotopes mentioned above, the catcher foil also contains ^{204}Bi, which is calculated to be formed in low yields (< 3%) during the nuclear reaction, but mainly from the electron capture (EC) decay of ^{204}Po. ^{205}Bi was not observed in the spectrum.

The γ-spectrum of the catcher foil after heating for two hours at a maximum temperature of (720 $\pm$ 20) °C shows that almost all polonium lines disappear. However, the line at 272 keV remains, which indicates an overlap with another isotope.
In addition to the desired nuclear reaction with the target material, reactions with the titanium target backing are also possible. The yields of such reactions were calculated for the most abundant isotope of titanium, ^{48}Ti (natural abundance 73.72%),[37] at different beam energies (see table 7.4). The calculation predicts the formation of ^{48}Cr by fusion-evaporation reaction in only low yields (< 3%). However, the γ-line at 308 keV (I_γ = 100%) matches this isotope (figure 4.1 light green).[21] The daughter of ^{48}Cr, ^{48}V, is also calculated to be produced in low yields (about 5%). The corresponding γ-peaks are shown in dark green in figure 4.1.
Other reaction types than fusion-evaporation can also produce nuclei with a similar composition to that of the target or projectile. Following, several scandium isotopes and their nuclear isomers were calculated to be produced and can be found in the spectrum of the catcher foil (highlighted in different shades of blue in figure 4.1). The γ-line of ^{44m}Sc at 271 keV (I_γ = 86.7%) overlaps with the γ-line of ^{204}Po which is why this peak was not used for evaluation.[21]

The comparison of the γ-spectrum of the catcher foil before and after two hours of heating shows that both polonium isotopes could be completely evaporated from the foil. A large part of the ^{204}Bi, as well as the scandium isotopes, ^{48}Cr and ^{48}V, could not be heated out of the foil.

4.1.2 Determination of the adsorption enthalpy of ^{204}Po in pure helium atmosphere (Rez2023-Po204-Bi204-TC-He)

To determine the enthalpy of adsorption of polonium on quartz glass (which was previously annealed at 1000 °C under inert gas atmosphere) in pure helium, an experiment was carried out as described in section 3.2.1. As described in the previous section, several γ-lines of ^{204}Po and ^{205}Po were identified (536 keV (intensity of 13.2%), 764 keV (11.5%), 885 keV (29.9%), 1018 keV (24.1%) of ^{204}Po and 851 keV (25.5%), 874 keV (37%), 1003 keV (28.8%) of ^{205}Po).[21]
The strongest lines of both isotopes were fitted with a Gaussian function and this fit was then integrated. As described above, the 272 keV γ-line of ^{204}Po could not be used for evaluation due to overlapping with the γ-line of ^{44m}Sc.
For a sufficient baseline correction, care was taken to average the baseline of the Gaussian fit over a sufficiently long interval. The integral of the Gaussian function therefore already contains a baseline correction. The use of this method is justified in this case, as the baseline to the right and left of the peaks under consideration was of about the same height. Figure 4.2 shows the γ-spectrum of the column section between 62 and 64 cm with the Gauss fit of the 885 keV γ-line with an intensity of 29.9% of ^{204}Po to determine the net peak area.

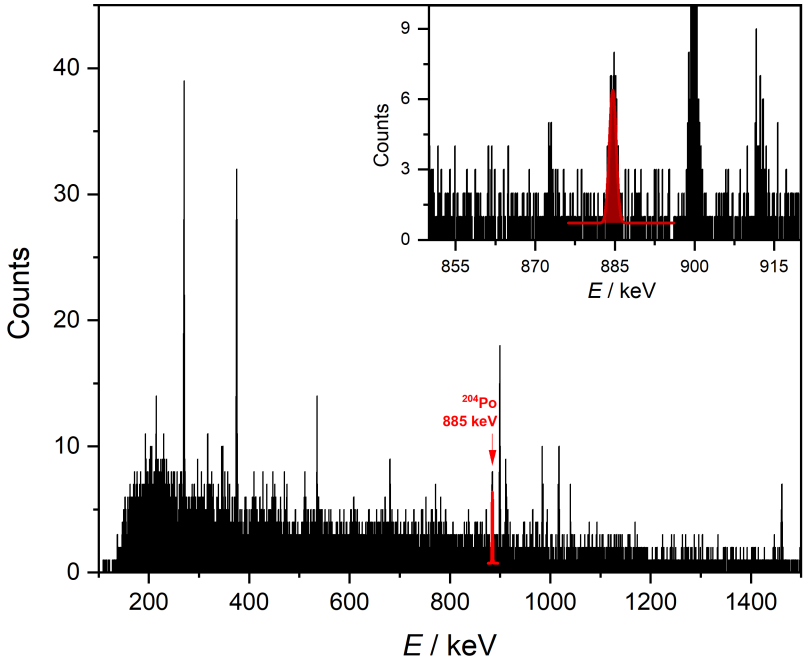

Figure 4.2: γ-spectrum of the column piece of 62-64 cm, the Gauss fit of the 885 keV γ-line of ^{204}Po (I_γ = 29.9%) is shown in red. The inset shows an enlargement of the region of interest.

The net peak areas obtained in this way and the corresponding errors were then normalized to the measurement time (live time, mean dead time in all measurements about 3%). Since the γ-spectra were recorded over a period of several hours, they were additionally decay corrected using the exponential law of decay. For this purpose, the measured activity was extrapolated to the starting time of the first measurement. As the measurement time of a few minutes is very short compared to the half-life of the two isotopes ($t_{1/2}$ of ^{204}Po is 3.53 h and $t_{1/2}$ of ^{205}Po is 1.66 h),[21] the decay during the measurement was not taken into account. The error of the measurement time and the start time of the respective measurements were assumed to be of one second or less and were therefore neglected.
As the column pieces were broken by hand, not every piece is exactly 2 cm long, but has an uncertainty of about $\pm$ 2 mm. The resulting error in the activity per two centimetres was added to the error of the net area of the peak obtained from the Gaussian fit.
The sum of the determined activities of all column segments was then used to calculate the relative deposition per two centimetres.

The ratio of the activity per two centimetres to the highest activity per two centimetres was determined for each γ-line and compared with the other γ-lines of polonium. If the ratio of the activity is the same, it can be ensured that no other impurities are present and that only the activity of the corresponding polonium isotope was evaluated. Since the ratio was roughly the same for all evaluated γ-lines, activities of underlying nuclei could be ruled out.

Only the strongest line of the longer-lived and obtained in higher yields ^{204}Po (885 keV, I_γ = 29.9%) was selected for the thermochromatogram in figure 4.3.

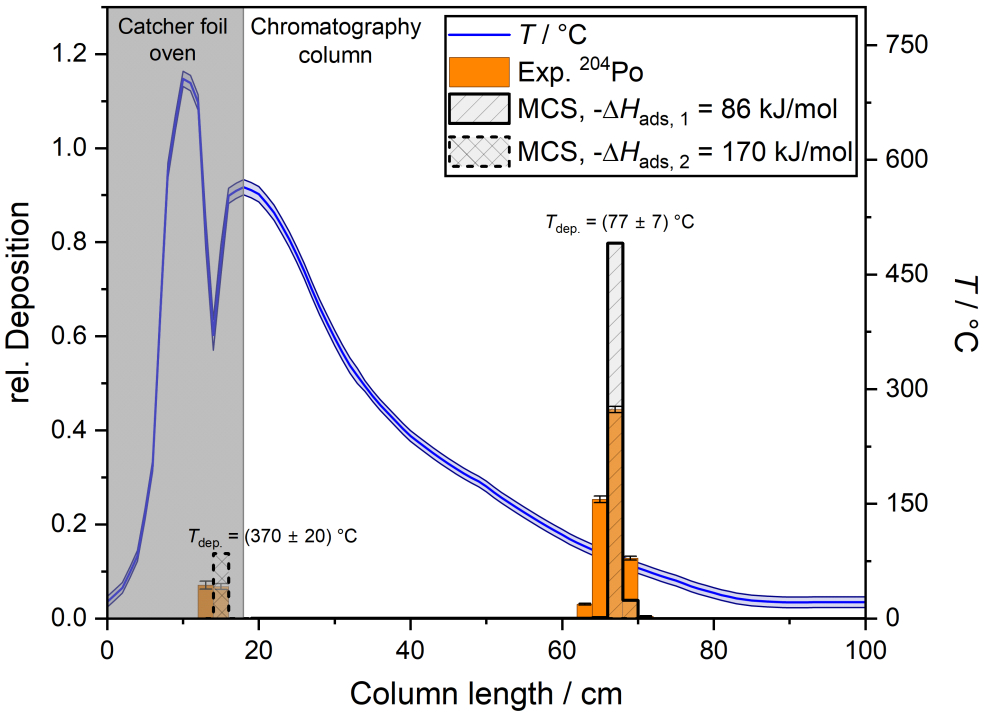

Figure 4.3: Thermochromatogram of the deposition of ^{204}Po (the 885 keV γ-line with an intensity of 29.9% has been analysed) on quartz glass with previous heat treatment in helium atmosphere. The experimentally measured deposition is shown in orange, the simulated deposition using the Monte Carlo method by Zvára is shown hatched and grey and the temperature is shown in blue. The deposition temperature in the column was determined on the basis of the peak maximum, the deposition temperature of the peak between the catcher foil furnace and the chromatography column corresponds to the temperature minimum. No activity was measured in the filter downstream of the column. To better compare the simulation with the experimental data, the simulated activity was multiplied by the ratio of the activity of the respective experimental peak to the total experimental activity.

Figure 4.3 shows a single deposition in the chromatography column at (77 ± 7) °C, as well as a deposition at the temperature minimum ((370 ± 20) °C) between the catcher foil furnace and the first gradient furnace. The best agreement between the experimental data and the Monte Carlo simulation was achieved with an adsorption enthalpy of -86 kJ/mol for the deposition in the column and -170 kJ/mol for the deposition in the transport line to the column (for further details such as input parameters of the simulation and error evaluation see below).

In addition to the deposition of polonium, figure 4.3 also shows the measured temperature gradient. The temperature error was determined on the basis of the error specified by the manufacturer of the read-out unit for the thermocouple (± 5 °C without thermocouple) and the additional error of the thermocouple. As the thermocouple was only 50 cm long, the temperature gradient had to be measured from both sides. This meant that two values were obtained for the temperature at 50 cm (once by measuring from the hot side and once from the cold side). The

difference between the two measurements was about 2 °C, which can be explained on the one hand by different bends in the thermocouple and thus a different length of the thermocouple or by the gas flow being switched off when measuring from the hot end. An additional error of ± 2 °C was therefore assumed for temperatures below 300 °C and an additional error of ± 5 °C for temperatures above 300 °C as the temperature gradient was steeper and the gradient could only be measured without the gas flow running. Especially between the furnace that heated the catcher foil and the first furnace for the temperature gradient of the actual column, the temperature changed very strongly with only a slight shift of the thermocouple, which is why an error of ± 20 °C was assumed here. In addition, the heating of the oven for the catcher foil during the experiment also influenced the temperature gradient in the whole column (especially at high temperatures), which is why comparatively large error bars are justified.

For further evaluation, the adsorption enthalpy of both depositions was determined using a Monte Carlo simulation according to Zvára (the code written in C++ can be found in the appendix). The input parameters selected for the simulation can be found in table 4.2. The simulation was initially only carried out for the actual column (highlighted in white in figure 4.3) and not for the transport route from the catcher foil furnace (highlighted in grey in figure 4.3). Since the temperature was only measured every two centimetres, it was interpolated in the remaining parts of the column using the method *Akima spline* (for measured and interpolated temperatures see table 7.5 to 7.7).[98]

Table 4.2: Input parameters used in the Monte Carlo simulation for determining the adsorption enthalpy of the ^{204}Po deposition on heat treated quartz glass in helium at (77 ± 7) °C in the column and between the catcher foil oven and the chromatography column. Here, T is the temperature, p the pressure, M the molar mass, F the proportion of helium in the gas phase, ρ the density at the boiling point, Q the gas flow, r the inner radius of the column, τ_0 the period of oscillation at the surface and t_{exp} is the experiment time.

input parameter	value for deposition in column	value for deposition before column	Reference
M_{Po} / g/mol	204	204	-
M_{He} / g/mol	4	4	-
F_{He}	1	1	
ρ_{Po} / g/cm^3	9.2	9.2	[78]
ρ_{He} / g/cm^3	0.125	0.125	[99]
Q / sccm/min	51	49	-
r / cm	0.20	0.21	-
p / bar	1.0	1.2	-
τ_0 / s^{-1}	$0.2 \cdot 10^{-12}$	$0.2 \cdot 10^{-12}$	[60]
T / °C	See appendix table 7.5 to 7.7	See appendix table 7.5 to 7.7, lower limit	-
t_{exp} / s	3600	1800	-

The best fit of the Monte Carlo simulation to the deposition at (77 ± 7) °C (also shown in figure 4.3) with an adsorption enthalpy of -86 kJ/mol deviates from the experimentally obtained data in the peak form as the experimental peak is significantly wider. On the one hand, this can be explained by the underlying assumptions of the Monte Carlo simulation: The simulation assumes that the equilibrium between the adsorbed state and the desorbed state is reached immediately. The adjustment is in reality however not immediate simply due to the time required for the carrier gas to reach thermal equilibrium. In addition, longitudinal diffusion is also neglected in the simulation which would also lead to broader peaks.[60] However, the greatest influence originates from the selected lifetime of the simulated atoms.
In the measurement carried out here, the lifetime corresponds to the duration of the experiment, as atoms that decay before the end of the experiment cannot be detected by the offline measurement. Longer-lived atoms are frozen at their respective position after the end of the experiment due to the removal of the column from the temperature gradient. However, the heating-out of the atoms from the catcher foil is not instantaneous but depends on the time. Atoms that are heated out of the foil later thus have less time in the column until the end of the experiment. In addition, the catcher foil was placed in a cold oven, which further leads to a dependency of the atoms evaporated on the temperature. The exact function of the heating-out of the polonium atoms therefore generates a distribution of different residence times in the column, which, however, cannot be taken into account in the simulation, as the exact dependence of the number of heated-out atoms on time and temperature is not known. The peak shape can therefore not be represented correctly in the simulation, but the influence of the different residence time of the atoms in the column on the adsorption enthalpy was taken into account in the error analysis.

To determine the error of the adsorption enthalpy of the main peak in the column, the experimental input parameters were varied according to their respective errors.
First, the influence of the gas flow was investigated. The error of the mass flow meter used was specified by the manufacturer as 1%. In addition, the narrowing in the column after the catcher foil can also lead to a higher gas velocity. Furthermore, the flow shown on the mass flow meter fluctuated between 50 and 52 sccm/min. The simulation was therefore carried out with a gas flow of 49 sccm/min and 53 sccm/min as the lower and upper limits. However, varying the gas flow did not change the adsorption enthalpy.
Next, the residence (experiment) time of the atoms in the column was examined. As described above, the residence time in the column depends on the time at which the atoms were baked out of the catcher foil. In the first simulation run (see table 4.2), an average experiment and therefore residence time in the column of 1 h was selected for the simulation. This time is based on the consideration that at the beginning of the measurement in the still cold catcher foil furnace, little to no atoms are heated out of the foil since the diffusion of atoms out of the foil is greatly dependent on the temperature. After a certain temperature is reached after a specific time (here estimated to be one hour), the atoms begin to diffuse from the foil to the surface, where they can then finally be heated out. In order to determine the influence of the residence and thus experiment time on the adsorption enthalpy, further simulation runs were carried out. A residence time of 2 h was chosen as the upper limit as this time corresponds to the full experiment duration between placing the catcher foil in the still cold oven and removing the column from the ovens at the end of the experiment. This simulation thus covers atoms which are immediately heated out from the foil after the beginning of the experiment. As a

lower limit, a residence time of 30 min was chosen based on the consideration that thermal equilibrium in the catcher foil oven is reached after 1.5 h at the latest, leaving 30 min left from the total duration of the experiment. At longer residence and thus experiment times, the atoms can move further in the column, whereby the best fit with the experimental data yields a more negative adsorption enthalpy (best agreement with -88 kJ/mol). The same applies conversely for the shorter residence time (best fit -84 kJ/mol).
In the next simulation run, the influence of the pressure in the column was investigated. As the column is basically an open system (open towards a fume hood), a pressure of 1 bar (atmospheric pressure) was assumed in the first simulation run. However, the gas flow (through thin capillaries) creates a pressure difference in the experimental setup. In addition, the activated carbon filter can act as a resistance for the gas flow, which can cause pressure to build up in the column. The simulation was therefore carried out again with a pressure of 1.2 bar. This led to a more positive adsorption enthalpy of 1 kJ/mol.
Subsequently, the radius of the chromatography column was also varied based on the inaccuracies of the diameter of the column specified by the manufacturer. A smaller radius of 1.9 mm lead to a more negative adsorption enthalpy of 1 kJ/mol, whereas a radius of 2.1 mm did not lead to a change in the adsorption enthalpy.
One of the biggest errors in the adsorption enthalpy is caused by uncertainty in the temperature. The simulation was carried out on the basis of the deviations in temperature determined above at the lower and upper ends of the error. Higher temperatures cause the atom to fly further and the adsorption enthalpy obtained gets more negative (best fit obtained for -88 kJ/mol). Conversely, the same applies to lower temperatures (best fit obtained for -84 kJ/mol).

In table 4.3, the deviations caused by varying the different experimental parameters in the simulation are shown. In order to obtain the error of the adsorption enthalpy, all deviations of the enthalpy when varying the experimental inputs were summed up.

Table 4.3: Varied experimental parameters, their input value for the simulation and the adsorption enthalpy obtained with the best match to the experiment (deposition of ^{204}Po on heat treated quartz glass in helium). The deviation of the adsorption enthalpy determined with the inputs used here from the adsorption enthalpy obtained with the inputs from table 4.2 is shown as well.

Varied parameter	input	$-\Delta H_{\mathrm{ads}}$ / kJ/mol	$\Delta\Delta H_{\mathrm{ads}}$ / kJ/mol
Q / sccm/min	49	86	0
Q / sccm/min	53	86	0
t_{exp} / s	7200	88	2
t_{exp} / s	1800	84	-2
p / bar	1.2	85	-1
r / mm	1.9	87	1
r / mm	2.1	86	0
T_{high} / °C	see table 7.5 to 7.7	88	2
T_{low} / °C	see table 7.5 to 7.7	84	-2

The lower and upper limit of the adsorption enthalpy determined in this way covers the entire experimental deposition peak in the simulation.

Considering everything described above, the adsorption enthalpy of polonium on quartz glass in helium was determined by the Monte Carlo simulation to be

$$-\Delta H_{\mathrm{ads},1} = (86 \pm 5)\,\mathrm{kJ/mol}.$$

Finally, in the last simulation run, the section between the catcher foil furnace and the first gradient furnace was also taken into account. However, no deposition could be observed in this part for the determined adsorption enthalpy.
In order to determine the adsorption enthalpy of the possible second species in the transport line from the catcher foil furnace, further simulations with more negative enthalpies were carried out while also considering the column part between the catcher foil furnace starting from the position of the catcher and the first gradient furnace. Since no atoms can pass the temperature minimum at a certain adsorption enthalpy, only the lower limit of the enthalpy can be estimated. Due to the error analysis described above, it is already known that lower temperatures and residence times, as well as a higher pressure, lead to the lower limit of the adsorption enthalpy. The input parameters of the simulation where therefore chosen as shown in table 4.2.

Based on the simulation, the lower limit of the adsorption enthalpy of the possible second species trapped in the transport line was determined to be

$$-\Delta H_{\mathrm{ads},2} \geq\ 170\,\frac{\mathrm{kJ}}{\mathrm{mol}}.$$

4.1.3 Determination of the adsorption enthalpy of ^{204}Bi in pure helium atmosphere (Rez2023-Po204-Bi204-TC-He)

As the catcher foil was irradiated overnight at the cyclotron and left to decay for some time after irradiation, $^{204}\mathrm{Bi}$ was formed from the EC-decay of $^{204}\mathrm{Po}$. When analysing the γ-spectra of the individual column sections, it was found that a significant amount of the bismuth was also heated-out from the catcher foil and deposited in column pieces without any polonium. Since bismuth is also interesting as a homologue of the superheavy element moscovium, and there is no experimental data of the deposition of bismuth on a quartz surface, the deposition of bismuth was also evaluated as described above for polonium using the measured γ-spectra.
For the thermochromatogram shown in figure 4.4, the 901 keV γ-line with an intensity of 98% was analysed. Since polonium was also deposited in the transport line in this experiment, the proportion of $^{204}\mathrm{Po}$ which had already decayed to $^{204}\mathrm{Bi}$ at the time of measurement was calculated and subtracted from the $^{204}\mathrm{Bi}$ activity.

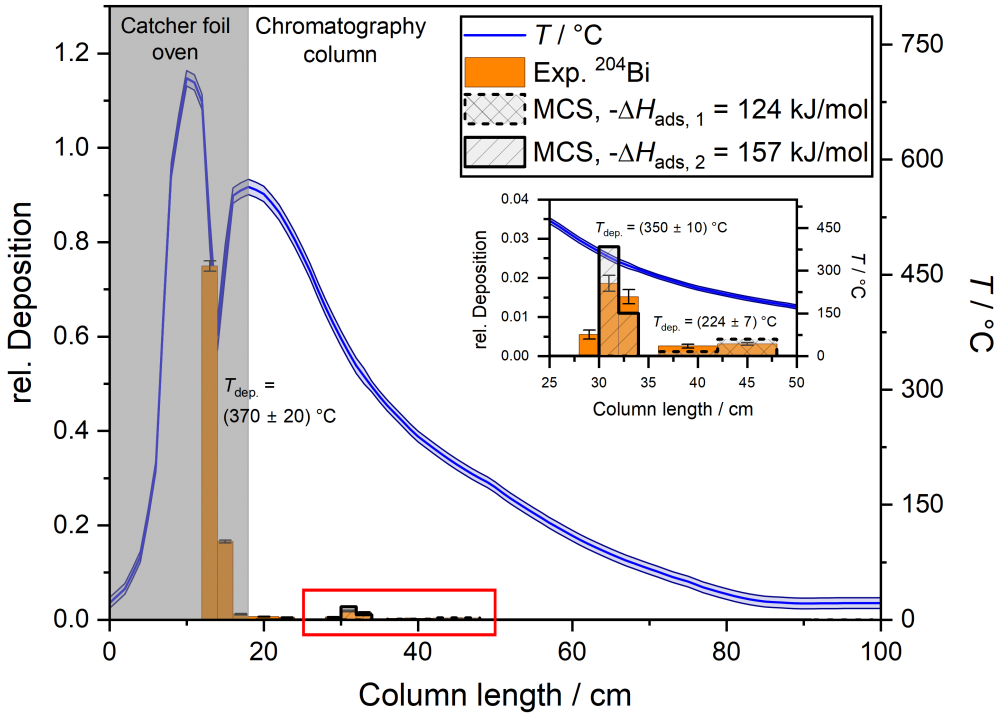

Figure 4.4: Thermochromatogram of the deposition of ^{204}Bi (the 901 keV γ-line with an intensity of 98% has been analysed) on quartz glass with previous heat treatment in helium atmosphere. The experimentally measured deposition is shown in orange, the simulated deposition using the Monte Carlo method by Zvára is shown hatched and grey and the temperature is shown in blue. The deposition temperature in the column was determined on the basis of the peak maximum, the deposition temperature of the peak between the catcher foil furnace and the chromatography column corresponds to the temperature minimum. No activity was measured in the filter downstream of the column. The area marked in red is shown enlarged at the top right. To better compare the simulation with the experimental data, the simulated activity was multiplied by the ratio of the activity of the respective experimental peak to the total experimental activity.

Figure 4.4 shows that a large part of the bismuth was trapped in the transport line between the catcher foil furnace and the column. However, a small amount of the ^{204}Bi was also deposited in the actual chromatography column. Two peaks can be detected in the chromatography column at (350 $\pm$ 10) °C and (224 $\pm$ 7) °C, whereby the minimum temperature of the transport line between the catcher foil furnace and the chromatography column ((370 $\pm$ 20) °C) matches the temperature of the high-temperature peak within the range of the error. No ^{204}Bi activity was found in the filter behind the column.
Again, the adsorption enthalpy of both peaks in the chromatography column was determined using the Monte Carlo simulation. Table 4.4 shows the input parameters used in order to obtain the adsorption enthalpy. In the first simulation run, only the actual chromatography column without the transport line was considered.

Table 4.4: Input parameters used in the Monte Carlo simulation for determining the adsorption enthalpies of the ^{204}Bi depositions on heat treated quartz glass at (350 ± 10) °C and (224 ± 7) °C. Here, T is the temperature, p the pressure, M the molar mass, F the proportion of helium in the gas phase, ρ the density at the boiling point, Q the gas flow, r the inner radius of the column, τ_0 the period of oscillation at the surface and t_{exp} is the experiment time.

Input parameter	value	reference
M_{Po} / g/mol	204	-
M_{He} / g/mol	4	-
F_{He}	1	-
ρ_{Po} / g/cm^3	9.78	[78]
ρ_{He} / g/cm^3	0.125	[99]
Q / sccm/min	51	-
r / cm	0.20	-
p / bar	1.0	-
τ_0 / s^{-1}	$0.2 \cdot 10^{-12}$	[60]
T / °C	Can be derived from table 7.5 to 7.7	-
t_{exp} / s	3600	-

The adsorption enthalpies that showed the greatest agreement to the experimental depositions are shown in figure 4.4 in grey ($-\Delta H_{\mathrm{ads},1}$ = 124 kJ/mol and $-\Delta H_{\mathrm{ads},2}$ = 157 kJ/mol).

A significant amount of bismuth was lost in the temperature minimum between the catcher foil furnace and the first gradient oven. The temperature of this temperature minimum ((370 ± 20) °C) is the same in the range of the error as the temperature of the deposition at (350 ± 10) °C. In order to determine whether the deposition in the transport line and the deposition in the chromatography column belong to the same species, the transport line was also taken into account in a second simulation run with the same inputs as in table 4.4. Figure 4.5 shows the thermochromatogram of ^{204}Bi on quartz glass in helium and the Monte Carlo simulation where the transport line to the column is also considered.

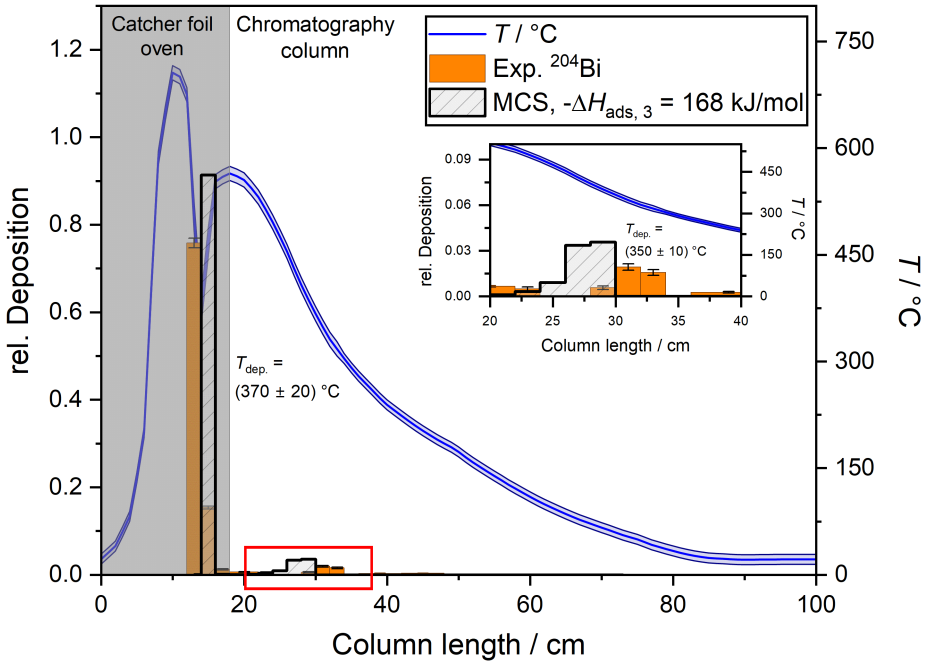

Figure 4.5: Thermochromatogram of the deposition of ^{204}Bi (the 901 keV γ-line with an intensity of 98% has been analysed) on quartz glass with previous heat treatment in helium atmosphere. The experimentally measured deposition is shown in orange, the simulated deposition which also considers the transport line from the catcher oven using the Monte Carlo method by Zvára is shown hatched and grey and the temperature is shown in blue. The deposition temperature in the column was determined on the basis of the peak maximum, the deposition temperature of the peak between the catcher foil furnace and the chromatography column corresponds to the temperature minimum. No activity was measured in the filter downstream of the column. To better compare the simulation with the experimental data, the simulated activity was multiplied by the ratio of the activity of the respective experimental peak to the total experimental activity.

The adsorption enthalpy of the simulation was chosen such that the ratio of the amount of deposition between the catcher foil furnace and the chromatography column to the amount of deposition in the column corresponds to the experiment. The enthalpy for the high-temperature species determined in the first simulation run ($-\Delta H_{\mathrm{ads},2}$ = 157 kJ/mol) does not lead to any deposition in the transport line, significant deposition only occurs at more negative adsorption enthalpies. However, more negative adsorption enthalpies lead to a shift of the peak in the column to higher temperatures and thus to a deviation from the experiment. In this case, the simulation is therefore not able to correctly represent the experimental result with the transport line between the catcher foil oven and the chromatography column. As can be seen below, both adsorption enthalpies that were determined in the two simulation runs with and without the transport line to the column are the same within the range of the error.

The error of the adsorption enthalpies of the two depositions was determined as described for the deposition of ^{204}Po, the deviations of the adsorption enthalpies with variation of the individual experimental parameters can be derived from table 4.5.

Table 4.5: Varied experimental parameters, their input value for the simulation and the adsorption enthalpy obtained with the best match to the experiment (deposition of ^{204}Bi on heat treated quartz glass in helium). The deviation of the adsorption enthalpy determined with the inputs used here from the adsorption enthalpy obtained with the inputs from table 4.4 is shown as well. Here, $-\Delta H_{\mathrm{ads},1}$ is the adsorption enthalpy of the peak at (224 ± 7) °C, $-\Delta H_{\mathrm{ads},2}$ is the adsorption enthalpy of the peak at (350 ± 10) °C without consideration of the transport line from the catcher foil furnace and $-\Delta H_{\mathrm{ads},3}$ is the adsorption enthalpy of the high-temperature peak obtained with consideration of the transport line.

Varied parameter	input	$-\Delta H_{\mathrm{ads},1}$ / kJ/mol	$\Delta\Delta H_{\mathrm{ads},1}$ / kJ/mol	$-\Delta H_{\mathrm{ads},2}$ / kJ/mol	$\Delta\Delta H_{\mathrm{ads},2}$ / kJ/mol	$-\Delta H_{\mathrm{ads},3}$ / kJ/mol	$\Delta\Delta H_{\mathrm{ads},3}$ / kJ/mol
Q / sccm/min	49	124	0	157	0	168	0
Q / sccm/min	53	124	0	157	0	168	0
t_{exp} / s	7200	127	3	161	4	172	4
t_{exp} / s	1800	121	-3	153	-4	164	-4
p / bar	1.2	123	-1	156	-1	167	-1
r / mm	1.9	124	0	157	0	168	0
r / mm	2.1	123	-1	156	-1	167	-1
T_{high} / °C	see table 7.5 to 7.7	125	1	159	2	173	5
T_{low} / °C	see table 7.5 to 7.7	122	-2	155	-2	163	-5

The simulations with and without transport line suggest that the deposition between the catcher foil furnace and the first gradient furnace, as well as the deposition at (350 ± 10) °C are caused by the same species, since the adsorption enthalpies determined with both methods ($-\Delta H_{\mathrm{ads},2} = 157^{+6}_{-8}$ kJ/mol without considering the transport line and $-\Delta H_{\mathrm{ads},3} = 168^{+9}_{-11}$ kJ/mol while also considering the transport line) are the same within the range of the error. Due to the large temperature uncertainty in the transport line, the simulation which determines the adsorption enthalpy from the ratio of the amount of deposition between the catcher foil oven and the chromatography column leads to greater inaccuracies. Therefore, the adsorption enthalpy of the high-temperature species is determined through the simulation which only considers the chromatography column.
The lower and upper limit of the adsorption enthalpies determined as described above cover the entire experimental deposition peaks in the simulation.

Using the Monte Carlo simulation and the error considerations described above, the adsorption enthalpy of the low-temperature species was determined to be

$$-\Delta H_{\mathrm{ads},1} = 124^{+4}_{-7}\,\mathrm{kJ/mol}$$

and the adsorption enthalpy of the high-temperature species (which also deposited in the transport line between the catcher foil furnace and the first gradient oven) was found to be

$$-\Delta H_{\mathrm{ads},2} = 157^{+6}_{-8}\,\mathrm{kJ/mol}.$$

4.1.4 Determination of the adsorption enthalpy of ^{204}Po in helium/hydrogen atmosphere (Rez2023-Po204-TC-H2)

In a second experiment, the enthalpy of adsorption of ^{204}Po on non-pretreated quartz glass in a helium/hydrogen atmosphere was determined as described in section 3.2.1.
The recorded γ-spectra of the individual column sections were analysed as described in section 4.1.2 and the temperature errors are also subject to the same considerations as described in this section. As the mass flow controller for reactive gases and the mass flow meter downstream of the column were calibrated to nitrogen and helium respectively, the flow was adjusted to the applied hydrogen mixture using the gas correction factors specified by the manufacturer of the mass flow controllers.
The thermochromatogram of the deposition of ^{204}Po on quartz glass without previous heat treatment in helium/hydrogen atmosphere obtained is shown in figure 4.6.

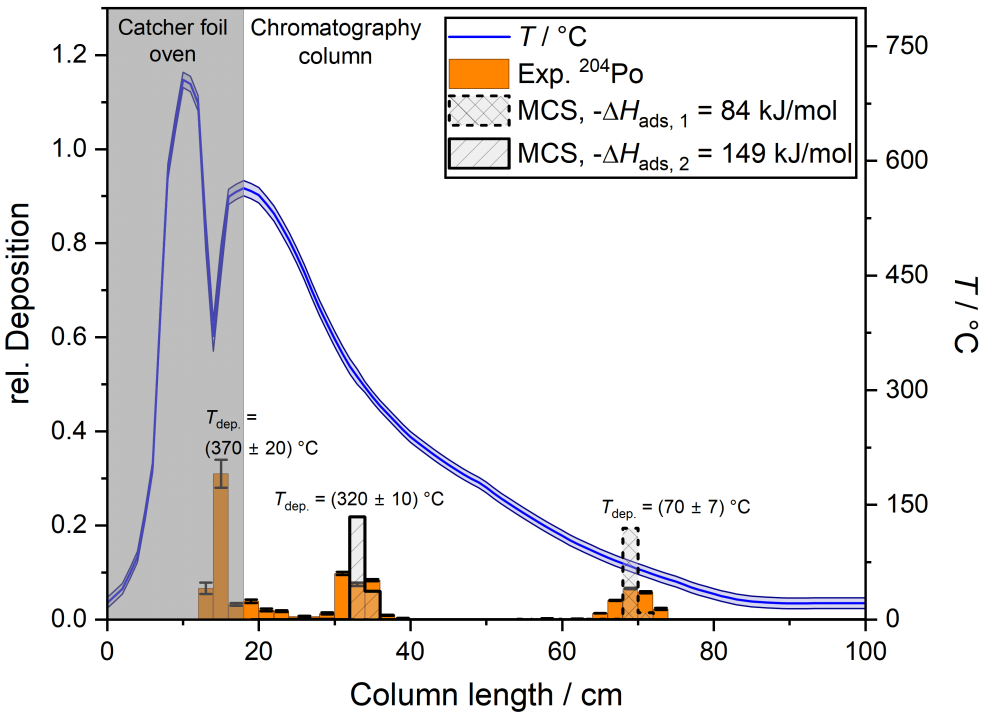

Figure 4.6: Thermochromatogram of the deposition of ^{204}Po (the 885 keV γ-line with an intensity of 29.9% has been analysed) on quartz glass without previous heat treatment in helium and hydrogen atmosphere. The experimentally measured deposition is shown in orange, the simulated deposition using the Monte Carlo method by Zvára is shown hatched and grey and the temperature is shown in blue. The deposition temperature in the column was determined on the basis of the peak maximum, the deposition temperature of the peak between the catcher foil furnace and the chromatography column corresponds to the temperature minimum. No activity was measured in the filter downstream of the column. To better compare the simulation with the experimental data, the simulated activity was multiplied by the ratio of the activity of the respective experimental peak to the total experimental activity.

Two peaks can be recognised in the chromatography column, one at (70 ± 7) °C and one at (320 ± 10) °C, as well as further deposition between the catcher foil furnace and the chromatography column. It can be concluded that at least two species were observed in the experiment. No activity was found in the filter behind the column.

Again, the adsorption enthalpy of both species was determined by the Monte Carlo method for further evaluation. Table 4.6 shows the experimental input parameters of the Monte Carlo simulation for the first simulation run of both species without considering the column part between the catcher foil furnace and the chromatography column.

Table 4.6: Input parameters used in the Monte Carlo simulation for determining the adsorption enthalpy of the ^{204}Po deposition on non-pretreated quartz glass in helium/hydrogen atmosphere at (320 ± 10) °C and (70 ± 7) °C. Here, T is the temperature, p the pressure, M the molar mass, F the proportion of helium in the gas phase, ρ the density at the boiling point, Q the gas flow, r the inner radius of the column, τ_0 the period of oscillation at the surface and t_{exp} is the experiment time.

Input parameter	value	reference
M_{Po} / g/mol	204	-
M_{He} / g/mol	4	-
$M_{\mathrm{H_2}}$ / g/mol	2	-
F_{He}	0.88	-
ρ_{Po} / g/cm^3	9.2	[78]
ρ_{He} / g/cm^3	0.125	[99]
$\rho_{\mathrm{H_2}}$ / g/cm^3	0.0708	[100]
Q / sccm/min	53	-
r / cm	0.20	-
p / bar	1.0	-
τ_0 / s^{-1}	$0.2 \cdot 10^{-12}$	[60]
T / °C	Can be derived from table 7.5 to 7.7	-
t_{exp}	3600 s	-

The adsorption enthalpies that showed the greatest agreement to the experimental deposition ($-\Delta H_{\mathrm{ads},1}$ = 86 kJ/mol and $-\Delta H_{\mathrm{ads},2}$ = 149 kJ/mol) are shown in figure 4.6 in grey.

As for bismuth, a significant amount of polonium was also deposited in the transport line from the catcher foil oven to the chromatography column. As the temperature in the transport line ((370 ± 20) °C) and the deposition temperature of the high-temperature species ((320 ± 10) °C) are quite similar, the area between the catcher foil oven and the chromatography column was also taken into account in a second simulation run with the same inputs as in table 4.6 to determine whether the two depositions belong to the same species. Again, the adsorption enthalpy was adjusted so that the ratios of the amount of activity in the column and in the transport line of the experiment and the simulation where in agreement with each other (see figure 4.7).

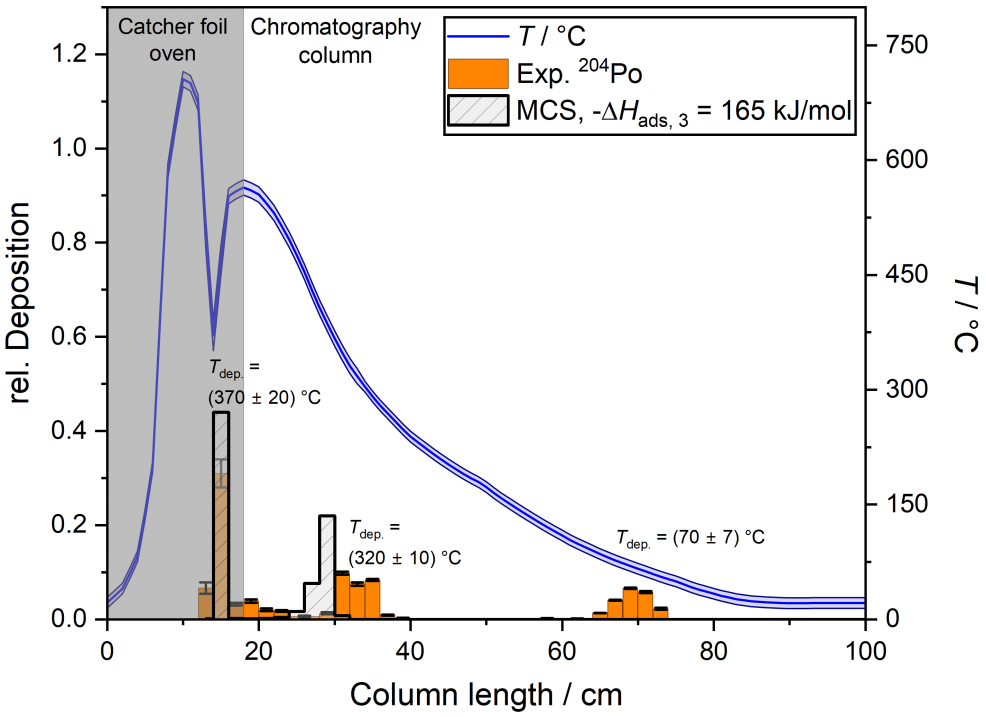

Figure 4.7: Thermochromatogram of the deposition of ^{204}Po (the 885 keV γ-line with an intensity of 29.9% has been analysed) on quartz glass without heat treatment in helium and hydrogen atmosphere. The experimentally measured deposition is shown in orange, the simulated deposition which also considers the transport line from the catcher oven using the Monte Carlo method by Zvára is shown hatched and grey and the temperature is shown in blue. The deposition temperature in the column was determined on the basis of the peak maximum, the deposition temperature of the peak between the catcher foil furnace and the chromatography column corresponds to the temperature minimum. No activity was measured in the filter downstream of the column. To better compare the simulation with the experimental data, the simulated activity was multiplied by the ratio of the activity of the respective experimental peak to the total experimental activity.

As with bismuth, the simulation with the previously determined adsorption enthalpy ($-\Delta H_{\mathrm{ads},2} = 149$ kJ/mol) of the high-temperature species without the transport line does not lead to deposition between the catcher foil furnace and the first gradient furnace. Only at more negative adsorption enthalpies does significant deposition occur in the transport line. This again leads to a shift of the peak in the column to higher temperatures. Again, the simulation which also considers the transport line to the column therefore cannot reproduce the experimental deposition between the catcher foil furnace and the chromatography column. However, as will be shown below, the adsorption enthalpy determined of the deposition at (320 $\pm$ 10) °C and in the temperature minimum ((370 $\pm$ 20) °C) in both simulation runs (with and without considering the transport line) is the same within the range of the error.

To determine the error of the adsorption enthalpies, the experimental input parameters of the simulation were varied according to the same considerations as described in section 4.1.2. The influence of the varied experimental parameters can be found in table 4.7. As the experiment du-

ration in this experiment was only 1.5 h, the upper limit of the experiment time in the simulation was adjusted accordingly.

Table 4.7: Varied experimental parameters, their input value for the simulation and the adsorption enthalpy obtained with the best match to the experiment (deposition of ^{204}Po on non-pretreated quartz glass in helium/hydrogen atmosphere). The deviation of the adsorption enthalpy determined with the inputs used here from the adsorption enthalpy obtained with the inputs from table 4.6 is shown as well. Here, $-\Delta H_{\mathrm{ads},1}$ is the adsorption enthalpy of the peak at (70 ± 7) °C, $-\Delta H_{\mathrm{ads},2}$ is the adsorption enthalpy of the peak at (320 ± 10) °C without consideration of the transport line from the catcher foil furnace and $-\Delta H_{\mathrm{ads},3}$ is the adsorption enthalpy of the high-temperature peak obtained with consideration of the transport line.

Varied parameter	input	$-\Delta H_{\mathrm{ads},1}$ kJ/mol	$\Delta\Delta H_{\mathrm{ads},1}$ / kJ/mol	$-\Delta H_{\mathrm{ads},2}$ / kJ/mol	$\Delta\Delta H_{\mathrm{ads},2}$ / kJ/mol	$-\Delta H_{\mathrm{ads},3}$ / kJ/mol	$\Delta\Delta H_{\mathrm{ads},3}$ / kJ/mol
Q / sccm/min	49	84	0	149	0	165	0
Q / sccm/min	56	84	0	149	0	165	0
t_{exp} / s	5600	86	2	151	2	167	2
t_{exp} / s	1800	82	-2	146	-3	161	-4
p / bar	1.2	83	-1	148	-1	164	-1
r / mm	1.9	84	0	149	0	165	0
r / mm	2.1	84	0	149	0	164	-1
T_{high} / °C	see table 7.5 to 7.7	86	2	151	2	170	5
T_{low} / °C	see table 7.5 to 7.7	82	-2	147	-2	160	-5

The error analyses show that deposition in the transport line and the deposition at (320 ± 10) °C are probably caused by the same species. Since the simulation with the transport line again leads to larger errors, the adsorption enthalpy of the high-temperature deposition was, as with bismuth, determined by the simulation of the chromatography column alone.
The lower and upper limit of the adsorption enthalpies determined cover the entire experimental deposition peaks in the simulation.

The Monte Carlo simulation and the error considerations described above enabled the adsorption enthalpies of the two observed species to be determined as

$$-\Delta H_{\mathrm{ads},1} = 84^{+4}_{-5}\,\mathrm{kJ/mol}$$

for the low-temperature deposition and

$$-\Delta H_{\mathrm{ads},2} = 149^{+4}_{-6}\,\mathrm{kJ/mol}$$

for the high-temperature deposition.

4.1.5 Determination of the adsorption enthalpy of ^{204}Po in helium/oxygen atmosphere (Rez2023-Po204-TC-O2)

In a final TC experiment, the adsorption enthalpy of ^{204}Po on quartz glass without previous heat treatment in a helium/oxygen atmosphere was determined as described in section 3.2.1.
The evaluation was carried out in exactly the same way as described in section 4.1.2, and the temperature errors were also chosen according to the same considerations as in this section. As the mass flow controller for reactive gases and the mass flow meter downstream of the column were calibrated to nitrogen and helium respectively, the flow was adjusted to the applied oxygen mixture using the gas correction factors specified by the manufacturer of the mass flow controllers.
Figure 4.8 shows the measured thermochromatogram for the deposition of ^{204}Po on quartz glass without previous heat treatment in helium and oxygen atmosphere.

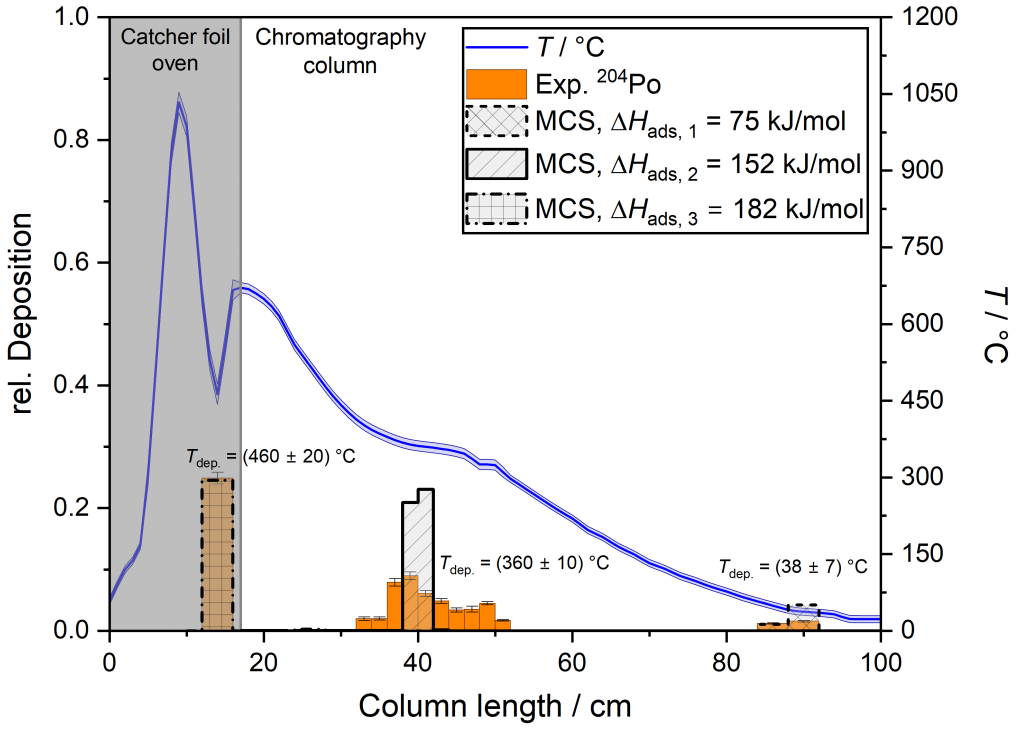

Figure 4.8: Thermochromatogram of the deposition of ^{204}Po (the 885 keV γ-line with an intensity of 29.9% has been analysed) on quartz glass without previous heat treatment in helium and oxygen atmosphere. The experimentally measured deposition is shown in orange, the simulated deposition using the Monte Carlo method by Zvára is shown hatched and grey and the temperature is shown in blue. The deposition temperature in the column was determined on the basis of the peak maximum, the deposition temperature of the peak between the catcher foil furnace and the chromatography column corresponds to the temperature minimum. No activity was measured in the filter downstream of the column. To better compare the simulation with the experimental data, the simulated activity was multiplied by the ratio of the activity of the respective experimental peak to the total experimental activity.

As in the previous experiment, two species were observed in the column, one at a temperature

of (360 ± 10) °C and the other at a temperature of (38 ± 7) °C. In addition, there is a significant amount of activity between the catcher foil oven and the actual chromatography column. Again, no polonium was found in the filter behind the column.

The adsorption enthalpy was determined using the Monte Carlo method to further analyse the deposition. The following table (table 4.8) shows the used input parameters for the first simulation run of both species. The column part between the catcher foil furnace and the first gradient oven was not considered in the first simulation run. As the total experiment duration in this experiment was only 1 h, the input for the simulation as well as the upper and lower limit of the input were adjusted accordingly.

Table 4.8: Input parameters used in the Monte Carlo simulation for determining the adsorption enthalpy of the ^{204}Po deposition on non-pretreated quartz glass in helium/oxygen atmosphere at (360 ± 10) °C and (38 ± 7) °C in the column and between the catcher foil oven and the chromatography column. Here, T is the temperature, p the pressure, M the molar mass, F the proportion of helium in the gas phase, ρ the density at the boiling point, Q the gas flow, r the inner radius of the column, τ_0 the period of oscillation at the surface and t_{exp} is the experiment time.

Input parameter	value for deposition in column	value for deposition before column	reference
M_{Po} / g/mol	204	204	-
M_{He} / g/mol	4	4	-
$M_{\mathrm{O_2}}$ / g/mol	32	32	-
F_{He}	0.90	0.90	-
ρ_{Po} / g/cm^3	9.2	9.2	[78]
ρ_{He} / g/cm^3	0.125	0.125	[99]
ρ_{O2} / g/cm^3	1.141	1.141	[101]
Q /sccm/min	50	49	-
r / cm	0.20	0.21	-
p / bar	1.0	1.2	-
τ_0 / s^{-1}	$0.2 \cdot 10^{-12}$	$0.2 \cdot 10^{-12}$	[60]
T / °C	Can be derived from table 7.5 to 7.7	Can be derived from table 7.5 to 7.7, low end	-
t_{exp}	2700 s	1800 s	-

The adsorption enthalpies that showed the greatest agreement to the experimental deposition are shown in figure 4.8 in grey.

Again, the input parameters of the simulation were varied in the range of their respective errors in order to determine the error of the adsorption enthalpies. The influence of the individual experimental variables on the adsorption enthalpy can be obtained from table 4.9.

Table 4.9: Varied experimental parameters, their input value for the simulation and the adsorption enthalpy obtained with the best match to the experiment (deposition of ^{204}Po on non-pretreated quartz glass in helium/oxygen atmosphere). The deviation of the adsorption enthalpy determined with the inputs used here from the adsorption enthalpy obtained with the inputs from table 4.8 is shown as well. Here, $-\Delta H_{\mathrm{ads},1}$ is the adsorption enthalpy of the peak at (38 ± 7) °C, $-\Delta H_{\mathrm{ads},2}$ is the adsorption enthalpy of the peak at (360 ± 10) °C without consideration of the transport line from the catcher foil furnace.

Varied parameter	input	$-\Delta H_{\mathrm{ads},1}$ / kJ/mol	$\Delta\Delta H_{\mathrm{ads},1}$ / kJ/mol	$-\Delta H_{\mathrm{ads},2}$ / kJ/mol	$\Delta\Delta H_{\mathrm{ads},2}$ / kJ/mol
Q / sccm/min	49	75	0	151	-1
Q / sccm/min	56	75	0	152	0
t_{exp} / s	3600	76	1	153	1
t_{exp} / s	1800	74	-1	149	-3
p / bar	1.2	75	0	151	-1
r / mm	1.9	75	0	152	0
r / mm	2.1	74	-1	151	-1
T_{high} / °C	see table 7.5 to 7.7	77	2	154	2
T_{low} / °C	see table 7.5 to 7.7	73	-2	149	-3

As the upper and lower ends of the adsorption enthalpy still do not cover the very broad deposition peak at (360 ± 10) °C, the error was extended downwards by 2 kJ/mol and upwards by 3 kJ/mol. This error interval covers the entire deposition in the simulation.

The simulation and the considerations above led to an adsorption enthalpy of

$$-\Delta H_{\mathrm{ads},1} = 75^{+3}_{-4}\,\mathrm{kJ/mol}$$

for the low-temperature species, and to an adsorption enthalpy of

$$-\Delta H_{\mathrm{ads},2} = 152^{+6}_{-11}\,\mathrm{kJ/mol}$$

for the high-temperature species.

In the last simulation run, the transport line from the catcher foil furnace to the column was also taken into account. Since in this case the temperature between the catcher foil furnace and the first gradient furnace ((460 ± 20) °C) and the deposition temperature of the high-temperature deposition ((360 ± 10) °C) differ significantly, only the lower limit of the adsorption enthalpy of a possible third species was determined. The reason for this is that above a certain adsorption enthalpy, no atom or molecule can pass through this temperature minimum in the transport line. The input parameters were selected according to the above error considerations in such a way that the lower limit of the adsorption enthalpy is determined by the simulation (see table 4.8).

By simulating the column part between the catcher foil oven and the chromatography column,

the adsorption enthalpy of a possible third species trapped in the transport line (see figure 4.8) could be determined to be

$$-\Delta H_{\mathrm{ads},3} \geq 182\,\mathrm{kJ/mol}.$$

4.2 Isothermal measurements of ^{216}Po on quartz glass and Teflon

The previously described experiments investigate ^{204}Po as a chemical homologue of livermorium. The significantly longer half-life of the isotope (3.53 h compared to 57 ms of ^{293}Lv),[37] however, leads to a longer residence time in the column and thus to different deposition temperatures than would be expected for an equally volatile but shorter-lived isotope. Consequently, in addition to the thermochromatography experiments with ^{204}Po, isothermal studies were also carried out with the short-lived ^{216}Po (half-life 145 ms)[21] as both the chemical and nuclear homologue of livermorium. The isotope was obtained as described in section 3.1.2 from a ^{224}Ra source, from which ^{220}Rn first emanates and then decays to ^{216}Po in-flight. Since radon as a noble gas populates the entire gas loop and continuously decays into ^{216}Po, a constant background of ^{220}Rn activity and its daughter ^{216}Po results within the COMPACT detector with a similar rate. In addition to the constant background of ^{216}Po from decay in-flight, ^{216}Po is formed from radon in the decay volume upstream of the column and is then transported with the gas flow through the column into the detector. This ^{216}Po activity will then be deposited in the detector in an exponential, diffusion-controlled manner (see figure 4.9).

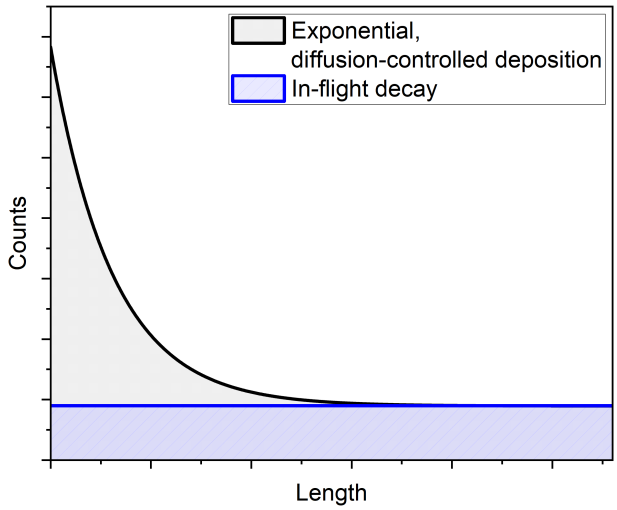

Figure 4.9: Schematic comparison of the ^{216}Po activity formed in the decay volume, which is deposited on the detector in a diffusion-controlled manner (grey), and the ^{216}Po activity formed from the in-flight decay of ^{220}Rn, which leads to a constant background (blue, modified from [102]).

In order to determine the total activity of ^{216}Po behind the decay volume as a reference for following experiments, the COMPACT detector was connected directly to this volume via a very

short (about 4 cm) Teflon capillary (GSI2024-Po216-IC-DC). Figure 4.10 shows the measurement time corrected, integrated α-peaks of $^{220}\mathrm{Rn}$ (6288.1 keV) and $^{216}\mathrm{Po}$ (6778.3 keV) in each detector element (left), as well as the α-spectrum of the detector with number 37 as an example for the selected integration limits (right).[21]

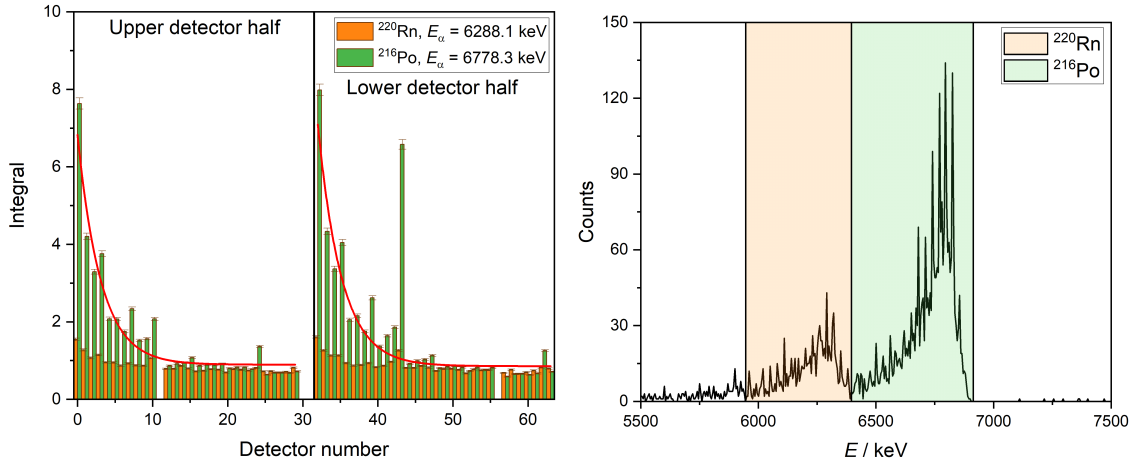

Figure 4.10: Plot of the integrals of the α-peaks of $^{220}\mathrm{Rn}$ (orange) and $^{216}\mathrm{Po}$ (green) normalised to the measurement time in the COMPACT detector against the detector number. An exponential fit of the integrals is shown in red, both detector halves were separated from each other by a vertical line (left). On the right side, an α-spectrum of detector number 37 with selected integration limits is shown.

The statistical error of the integral was assumed to be the respective root of the amount of the integral. This error takes into account the lower statistics and thus the greater error with small peaks. The error of the measurement time was neglected due to its low significance.
Figure 4.10 shows that the detectors numbered 11 and 56 are missing and that an unusually high activity was measured in detectors 24, 43 and 62. The artefacts in the detectors 11, 24, 43 and 56 have a technical background and can probably be explained by unintentional electrical contact between the detectors on the upper and lower side of the COMPACT. As a result, activity that was actually measured on the lower half of the detector for example, may be passed on to the upper half of the detector so that the activity is zero on one side and twice as high on the other. The unusually high activity in detector 62 can probably be explained by turbulence in the gas flow at the outlet of the detector. All the artefacts mentioned above can be found in all the measurements carried out and were not taken into account for the evaluation.
Figure 4.10 left also shows that the activity of $^{220}\mathrm{Rn}$ is higher in the first detector elements than in the rear detectors. This is due to the very large $^{216}\mathrm{Po}$ peak, whose tail at low energies overlaps with the $^{220}\mathrm{Rn}$ peak. The tailing towards lower energies can be explained by α-particles entering the detector at very shallow angles.[96]
In order to determine the activity of the $^{216}\mathrm{Po}$ formed in the decay volume, the mean value of the $^{216}\mathrm{Po}$ activity from $^{220}\mathrm{Rn}$ decayed in-flight was determined in the rear detector elements. The thus determined activity of $^{216}\mathrm{Po}$ from the decay in-flight of $^{220}\mathrm{Rn}$ was then subtracted as background. The error of the subtracted background resulted from the standard deviation. The remaining $^{216}\mathrm{Po}$ activity was then summed up, representing a total activity of

$$(48 \pm 2)\,\text{a.u.}$$

produced in the decay volume (while also considering the error of the integrals determined above).
This value is used in the following as the 100% breakthrough reference for determining the relative breakthrough.

4.2.1 Isothermal measurement of ^{216}Po on quartz glass (GSI2024-Po216-IC-Quartz)

In order to determine the adsorption enthalpy of ^{216}Po on quartz glass, the quartz column was connected to the COMPACT detector using the shortest possible Teflon capillary (about 4 cm). Initial tests showed that longer Teflon capillaries between the quartz column and the detector led to a significant loss of ^{216}Po transported from the column. The shortest possible transport routes are therefore essential for the investigation of this short-lived isotope.

Figure 4.11 again shows the measurement time corrected integrals of the α-peaks of ^{216}Po and ^{220}Rn in all detector elements. The error of the integral was determined as described in the previous section.

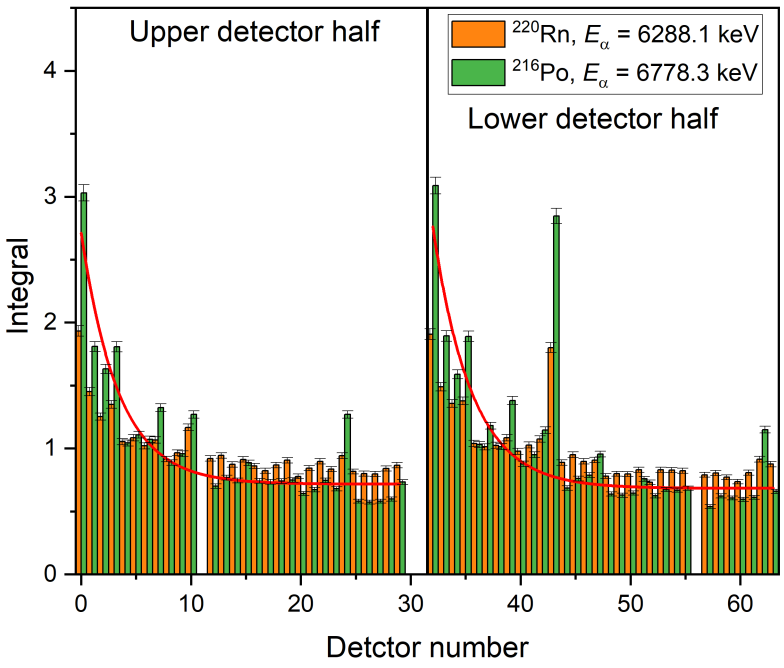

Figure 4.11: Plot of the integrals of the α-peaks of ^{220}Rn (orange) and ^{216}Po (green) normalised to the measurement time in the COMPACT detector after a quartz column against the detector number. An exponential fit of the integrals is shown in red, both detector halves were separated from each other by a vertical line.

To evaluate the activity transported through the column, the $^{216}\mathrm{Po}$ formed from the in-flight decay of the $^{220}\mathrm{Rn}$ in the rear detector elements was determined and subtracted from all measured peaks as background. The error again resulted from the standard deviation of the mean value, as well as the previously determined error of the integrals. Finally, all background-corrected peaks were totalled. An activity of

$$(17 \pm 2)\,\mathrm{a.u.}$$

was found behind the quartz column.
Since both the value for 100% breakthrough and the proportion of activity behind the column are subject to errors, an error propagation must be carried out. Since both errors are independent of each other, a gaussian error propagation is chosen (equation 4.1).

$$\Delta x = \pm\sqrt{\left(\frac{\partial x}{\partial I_0}\cdot\Delta I_0\right)^2 + \left(\frac{\partial x}{\partial I}\cdot\Delta I\right)^2} = \pm\sqrt{\left(-\frac{I}{I_0^2}\cdot\Delta I_0\right)^2 + \left(\frac{1}{I_0}\cdot\Delta I\right)^2} \tag{4.1}$$

Where x is the breakthrough through the column, I_0 is the activity directly behind the decay chamber and I is the activity behind the column.
The breakthrough through the quartz column was therefore determined to be

$$(35 \pm 4)\,\%.$$

4.2.2 Isothermal measurement of ^{216}Po on Teflon (GSI2024-Po216-IC-Teflon)

In a second experiment, the deposition of $^{216}\mathrm{Po}$ on a Teflon capillary was investigated. Figure 4.12 shows the measured activity determined from the integrals of the α-peaks of $^{220}\mathrm{Rn}$ and $^{216}\mathrm{Po}$ in all detector elements.

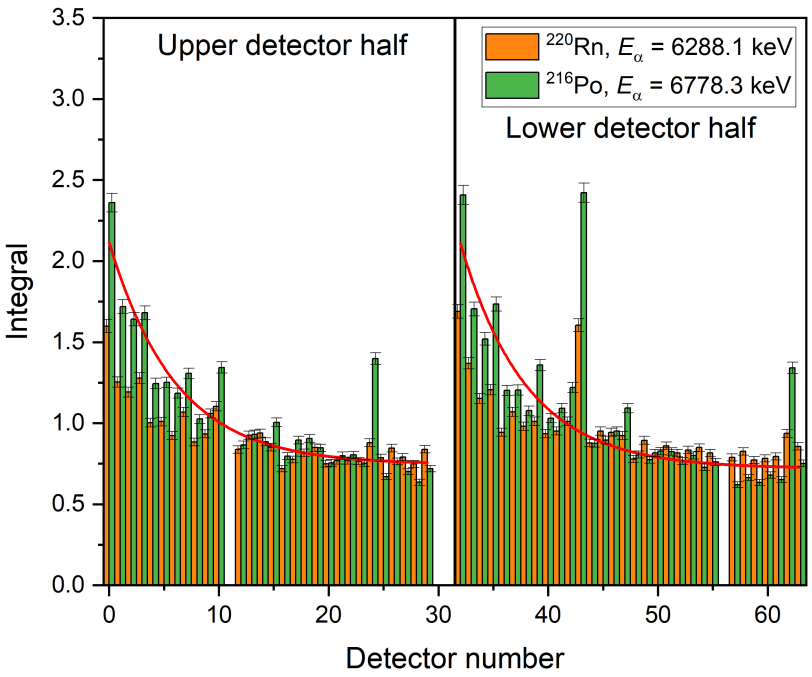

Figure 4.12: Plot of the integrals of the α-peaks of $^{220}\mathrm{Rn}$ (orange) and $^{216}\mathrm{Po}$ (green) normalised to the measurement time in the COMPACT detector after a Teflon column against the detector number. An exponential fit of the integrals is shown in red, both detector halves were separated from each other by a vertical line.

Again, the activity was normalised to the measurement time and the activity due to the in-flight decay of radon was subtracted. By adding up all the peaks, a total activity of

$$(14 \pm 2)\,\mathrm{a.u.}$$

was obtained, which corresponds to a breakthrough of

$$(28 \pm 4)\,\%.$$

The error was again derived from the Gaussian error propagation in equation 4.1.

5

Interpretation and discussion of the results

5.1 Thermochromatographic studies of ^{204}Po and ^{204}Bi on quartz glass

5.1.1 Determination of the adsorption enthalpy of ^{204}Po in pure helium atmosphere (Rez2023-Po204-Bi204-TC-He)

As described in section 2.3.1, polonium is a very reactive metal that forms compounds with many elements. According to the literature, titanium polonide is produced at a temperature of 570 °C by heating titanium in polonium vapour for half an hour.[103] Here, a titanium catcher foil which contained polonium atoms was heated to temperatures up to (720 ± 20) °C. As the catcher foil was placed in the cold oven and the oven was only heated up afterwards, it can be assumed that elemental polonium was evaporated from the catcher foil before the reaction temperature was reached. However, once the reaction temperature has been reached, the reaction to titanium polonide (TiPo) can no longer be ruled out. As TiPo is an intermetallic, relatively heavy compound, it can be assumed that it would be of low volatility, therefore depositing at higher temperatures. It would not even be unlikely that TiPo would be so low volatile that it would not be removed from the catcher foil in the first place. This is confirmed by the thermochromatographic studies of traces of polonium in titanium columns by S. Hübener and I. Zvára, who measured a deposition temperature of (1100 ± 50) °C (adsorption enthalpy of (-330 ± 30) kJ/mol). This high enthalpy was explained by the formation of titanium polonides.[92]
Titanium polonide dissociates at around 700 °C, so once the thermal equilibrium has been fully reached (temperature of (720 ± 20) °C), the compound can be assumed to dissociate and elemental polonium becomes the predominant species again (reaction in the gas phase (helium) and with the previously annealed quartz surface can be excluded). Based on the considerations above, two deposition peaks would be expected in the column if TiPo is formed, whereby the deposition at higher temperatures would be asigned to TiPo.

The results of the experiment in figure 4.3 show one large deposition peak at the relatively

low temperature of (77 ± 7) °C with an adsorption enthalpy of (-86 ± 5) kJ/mol and an additional deposition in the transport line between the catcher foil furnace and the first gradient oven at (370 ± 20) °C with an adsorption enthalpy of at least -170 kJ/mol. Since TiPo as an intermetallic compound is assumed to be of low-volatility, the low temperature peak most probably belongs to elemental polonium. The presence of the dimer (Po_2) can also be ruled out due to the low concentration of polonium.
The determined adsorption enthalpy of elemental ^{204}Po on quartz glass is in excellent agreement with the adsorption enthalpy of polonium on quartz published by the Paul Scherrer Institut in the annual report from 1996 (-85 kJ/mol, no error given) and with the observation of more current publications that polonium is a rather volatile metal.[76,94]

The temperature of the peak in front of the column differs significantly from the deposition temperature of the main peak. It can therefore not be ruled out that TiPo was also produced during the experiment. However, by placing the catcher foil in the column, turbulence is created in the gas flow at the beginning of the column which is expected to lead to more wall contacts of the polonium atoms and thus to a longer residence time of the atoms on the surface. Since TiPo is an intermetallic compound, it seems unlikely that it was heated out of the titanium catcher foil during the experiment. On the contrary, it seems more likely that produced titanium polonide would have remained on the unreacted titanium foil which would then be visible in the γ-spectrum of the catcher foil after the experiment. As this is not the case, the deposition between the catcher foil oven and the chromatography column is expected to result from effects such as more wall contacts from turbulences that cannot be taken into account by the Monte Carlo simulation.

5.1.2 Determination of the adsorption enthalpy of ^{204}Po in helium/hydrogen atmosphere (Rez2023-Po204-TC-H2)

The observed deposition at (70 ± 7) °C and the corresponding adsorption enthalpy of $-84^{+4}_{-5}\,\mathrm{kJ/mol}$ are in very good agreement with the deposition measured in the previous experiment in pure helium atmosphere (Rez2023-Po204-Bi204-TC-He), which was assigned to elemental polonium. Accordingly, the deposition measured in this experiment can also be assumed to be caused by elemental polonium.

Due to the fact that two species where observed (second high-temperature deposition at (320 ± 10) °C with an adsorption enthalpy of 149^{+4}_{-6} kJ/mol), the assumption quickly arises that polonium could have reacted with the added hydrogen to form H_2Po. However, it is known from studies with ^{210}Po produced in a reactor (by neutron capture of ^{209}Bi and subsequent β^--decay of the resulting ^{210}Bi) that elemental polonium does not react with molecular hydrogen (see also section 2.3.1 and figure 2.7 within this section). In addition, the hydride is thermally unstable and the known high volatility for the hydride does not match the measured deposition temperature and the corresponding adsorption enthalpy.[74,75,78,87,90] Therefore, the observation of H_2Po can be ruled out.

Hydrogen cannot have reacted with the polonium, but hydrogen can react with the quartz

surface and make it more reactive by forming silanol groups (Si-OH) on the surface, therefore enabling a reaction of polonium with the surface of the column.[104–107]
Quartz glass can, in general, be described by the chemical formula SiO_2 and is formed by slow cooling of molten crystalline quartz (also SiO_2). The cooling produces an increasingly viscous liquid which, in contrast to crystalline quartz, forms a structure with a near-range order but no long-range order. Like crystalline quartz, quartz glass also consists of SiO_4-tetrahedra (with a silicon atom in the centre and four oxygen atoms on the corners of the tetrahedron), which, in contrast to crystalline quartz, differ in the way they are linked to each other. The structure of the glass is "more disordered" in comparison to the crystalline structure of quartz and therefore often called "random-network" (see figure 5.1 for a comparison).[2,60,78,88,108,109] Two main end groups, the siloxane groups and the silanol groups, can occur on the surface of quartz glass (see figure 5.1).[109,110] Furthermore, up to three monolayers of water can be chemisorbed on silanol groups in particular.[60,105,109,110]

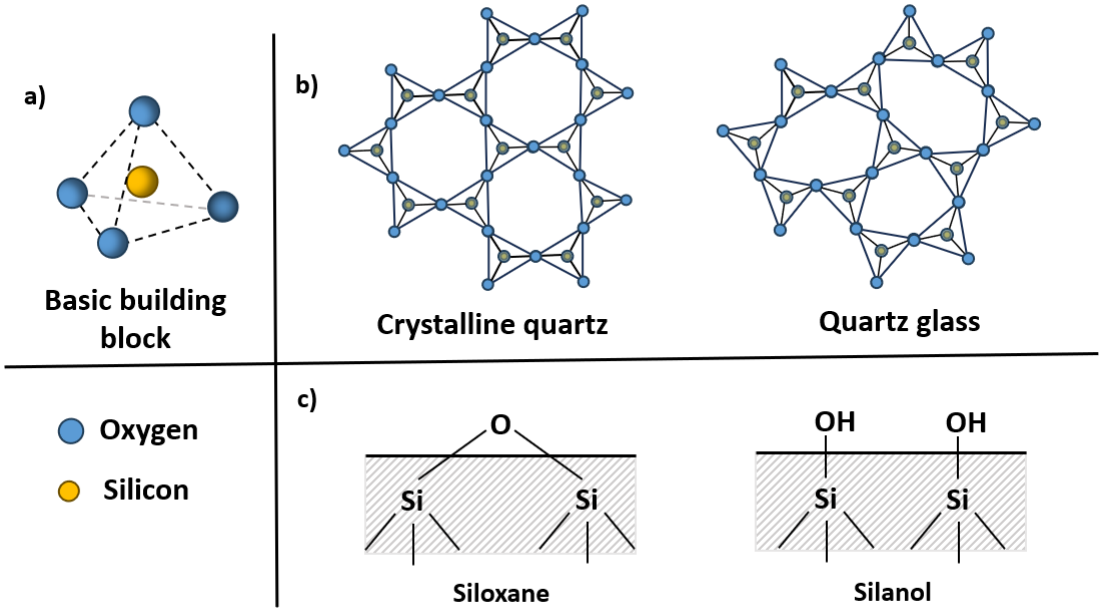

Figure 5.1: Basic building block of quartz glass and crystalline quartz (a), comparison between crystalline quartz and quartz glass (b) and functional groups on the surface of quartz glass (c).

The exact nature of the surface depends above all on the manufacturing process of the quartz glass and on its thermal history. If an oxygen-hydrogen flame is used to melt the quartz granulate for the production of the glass, the quartz glass contains a very high concentration of hydroxyl groups, even in the bulk material. By electro-melting the crystalline quartz in a vacuum on the other hand, the quartz glass contains a very small concentration of hydroxyl groups and is therefore significantly less reactive.[105,111] If the quartz glass, independently of the manufacturing process, is heated to high temperatures (800-1000 °C) in a vacuum after production, the hydroxyl content of the quartz glass can be reduced further.[105,110,111] The reformation of the hydroxyl groups lost is very slow at room temperature (several months to years depending on the storage) and can only take place in the presence of water (as in moisture in the air). Heating at

moderate temperatures (200 to 300 °C), only leads to a loss of the water adsorbed on the surface. The reformation of the water layer on the surface is reversible after the quartz glass has cooled down.[110]
Heating quartz glass in the presence of water or hydrogen to high temperatures above 300 °C however, leads to an increase in the hydroxyl concentration, especially in the case of fused silica which previously had a very low hydroxyl content.[105–107,111] The mechanism of the reactions, especially the reaction of quartz glass with hydrogen, is debated. The following reactions are discussed in the literature.

Water can react with the siloxane groups present on the surface at temperatures above 300 °C, forming two silanol groups in each case (see reaction 5.1).[105,111]

$$H_2O + -Si-O-Si- \longrightarrow 2SiOH \tag{5.1}$$

If both hydrogen (in the gas atmosphere) and oxygen (dissolved in the quartz glass) are present, these components can also react with each other to form water, which then reacts further according to the above reaction. This mechanism would be dependent on the diffusion of the dissolved oxygen which in turn would be dependent on the applied temperature.[105]
J. E. Shelby et al. treated quartz glass, which was produced by different manufacturing methods and thus contains different hydroxyl concentrations, with water. By analysing the hydroxyl-bands with vibrational spectroscopy, they found that quartz glass with an originally very high proportion of hydroxyl groups lost hydroxyl groups during treatment, and quartz glass with a very low proportion of silanol gained many hydroxyl groups. After 180 h of treatment, all glasses reached an equilibrium state with the same amount of hydroxyl groups.[105]

Another discussed mechanism for the formation of silanol groups is based on a direct reaction of hydrogen with the siloxane groups of the quartz surface (see equation 5.2).[104–106]

$$H_2 + -Si-O-Si- \longrightarrow SiOH + SiH \tag{5.2}$$

The confirmation of this reaction mechanism can be achieved by following the product formation (with for example infra-red or Raman spectroscopy), since always as many Si-OH groups as Si-H groups would be formed. However, this could not be proven for all quartz glasses analysed (differences due to the manufacturing process, among other things), which is why a third reaction mechanism was proposed.[105,106]

The last proposed mechanism assumes a reaction with peroxy-defects at the surface (see equation 5.3).[105,107,112]

$$H_2 + -Si-O-O-Si- \longrightarrow 2SiOH \tag{5.3}$$

The possible number of silanol groups formed on the surface would be limited by the existing number of peroxy groups and only hydroxyl and no hydride groups would be formed on the surface. However, as with the above mechanism, this was not the case for every quartz glass analysed. Consequently, the mechanism presumably depends on the exact nature of the treated quartz glass and therefore also on the manufacturing process.[105,107,112]
Regardless of the mechanism involved, hydroxyl groups are always formed when water or

hydrogen reacts with the surface of fused silica. As the siloxane groups are comparatively inert due to the π-component in the bond, the surface becomes more reactive due to the formation of silanol groups.[110]
To summarise, it can be said that the reactivity of the quartz surface is influenced by the following aspects.

- The quantity of silanol groups on the surface in relation to the siloxane groups determines the reactivity of the surface.
- The manufacturing process of the quartz glass determines the initial concentration of hydroxyl groups on the surface.
- By annealing the quartz glass at 1000 °C in an inert gas atmosphere, the proportion of silanol groups and therefore the reactivity of the surface can be reduced.
- Heating the quartz glass to temperatures above 300 °C in the presence of water or hydrogen increases the proportion of hydroxyl groups and makes the surface more reactive.

In the experiment discussed here, hydrogen was used as a reactive gas and the temperature gradient applied to the column had a maximum temperature of (720 $\pm$ 20) °C. It can therefore not be ruled out that the quartz surface was modified by a reaction of the quartz with hydrogen. The associated formation of silanol groups on the surface would allow the polonium to react with the quartz surface. However, the depositions of polonium obtained in helium and hydrogen atmosphere ($-\Delta H_{\mathrm{ads},1} = 84^{+4}_{-5}\,\mathrm{kJ/mol}$ and $-\Delta H_{\mathrm{ads},2} = 149^{+4}_{-6}\,\mathrm{kJ/mol}$) and in helium and oxygen atmosphere ($-\Delta H_{\mathrm{ads},1} = 75^{+3}_{-4}\,\mathrm{kJ/mol}$ and $-\Delta H_{\mathrm{ads},2} = 152^{+6}_{-11}\,\mathrm{kJ/mol}$) are strikingly similar to each other. In the range of the error, about the same adsorption enthalpies were found for both species in both experiments. This raises the question of whether it was really the hydrogen that made the surface more reactive, or whether the surface of the quartz glass in both experiments was already more reactive in itself, therefore making a reaction with the quartz possible. This theory is supported by the consideration that the reaction of hydrogen with the quartz surface is very slow.[105]
The quartz glass used in the experiment in pure helium atmosphere ((Rez2023-Po204-Bi204-TC-He)) was annealed under helium at a temperature of 1000 °C some months before the experiment, therefore leading to a reduction of the silanol groups. The quartz glass used in the experiment with hydrogen and oxygen was not pretreated and should therefore have significantly more silanol groups on the surface. It is therefore plausible that a reaction of the polonium with the surface of the quartz glass was made possible by the fact that the quartz glass used in the experiments with hydrogen and oxygen was not thermally pretreated.
Since the reaction of polonium with hydrogen in the gas phase is excluded as described above, the most plausible explanation for the deposition at higher temperatures is a reaction with the more reactive quartz surface.

In addition to physisorption, reactive silanol groups on the surface open up the possibility of chemisorption, i.e. a reaction of polonium with the surface. As described in section 2.2.2, chemisorption is an irreversible process in which a new species is formed, and adsorption is significantly stronger compared to physisorption due to the formation of a chemical bond with the surface.[50,60,61,64]

To investigate further, the energy barrier of chemisorption was calculated using the extended Monte Carlo simulation proposed by D. Dietzel et al.[65] The experimental parameters from table 4.6 and the previously determined adsorption enthalpies of both species were used as inputs, and the energy barrier was varied until the best match with the experimental data was found. The ratio of the experimentally determined depositions of the peaks of the two species was therefore compared with the ratio of the simulated depositions of the two species. To determine the error of the energy barrier, the upper and lower limits of the previously determined adsorption enthalpies were then used as inputs and the energy barrier was again determined with the best agreement to the experimental data.
An energy barrier of

$$(144 \pm 4)\,\mathrm{kJ/mol}$$

allowed the experimental data to be reproduced very well (see also figure 7.2 in the appendix).

In addition to the depositions in the column, another deposition can be observed between the catcher foil oven and the actual chromatography column. As shown in section 4.1.4, this deposition, as well as the high temperature deposition at (320 ± 10) °C in the chromatography column, belong to the same species from the reaction with the quartz surface.
The formation of TiPo seems unlikely due to the high-temperature in the catcher foil oven, at which the polonide already dissociates.[103,113]

The above considerations clearly show that polonium is reactive towards the quartz surface if the surface has enough reactive sites due to silanol groups. It is not trivial to infer exactly which reaction could have taken place on the surface. However, the assumption of an oxide species is, in view of the reactive groups on the quartz surface, reasonable.
The experiments carried out as part of this thesis show that a reaction with the surface of the column is just as important as reactions in the gas phase. Nevertheless, reactions with the surface have often been dismissed as unimportant in the past and the surface used has not been further specified in many publications. However, as the studies of the superheavy element flerovium have already shown,[67] this is a misconception that can lead to misinterpretations of the data obtained.

The comparison of the adsorption enthalpy of the species formed by surface reaction determined here ($-149^{+4}_{-6}\,\mathrm{kJ/mol}$) is of a similar order of magnitude in the range of the error to the adsorption enthalpy of $^{211\mathrm{m}}$Po on quartz glass determined by H. Gäggeler et al. ((-123 ± 11) kJ/mol).[92] It is therefore conceivable that a more reactive quartz glass was also used in their study.

5.1.3 Determination of the adsorption enthalpy of ^{204}Po in helium/oxygen atmosphere (Rez2023-Po204-TC-O2)

As described in section 4.1.5, two species were measured in the column in helium and oxygen atmosphere. The adsorption enthalpy of the low-temperature species ($-75^{+3}_{-4}\,\mathrm{kJ/mol}$) corresponds to the adsorption enthalpy assigned to elemental polonium in the previously discussed experiments in helium and helium/hydrogen atmosphere within the range of the error. Consequently, it is likely that the deposition at (38 ± 7) °C is also elemental polonium.

It is known from classical chemical studies of polonium that the metal can be slowly oxidized at room temperature in air to form the dioxide, in which the polonium is found in its most stable oxidation state +4. The reaction is most rapid at temperatures of 250 °C, the dioxide is stable up to very high temperatures.[74,75,77,90,114] Consequently, the possibility that PoO_2 was formed in this experiment seems very plausible. However, as already discussed in the previous section, the adsorption enthalpies of both species are identical in the experiment with oxygen (($-\Delta H_{\mathrm{ads},1} = 75^{+3}_{-4}\,\mathrm{kJ/mol}$ and $-\Delta H_{\mathrm{ads},2} = 152^{+6}_{-11}\,\mathrm{kJ/mol}$)) to those in the experiment with hydrogen (($-\Delta H_{\mathrm{ads},1} = 84^{+4}_{-5}\,\mathrm{kJ/mol}$ and $-\Delta H_{\mathrm{ads},2} = 149^{+4}_{-6}\,\mathrm{kJ/mol}$)) which was explained in the previous section by a reaction with the quartz surface, as in both experiments a quartz glass with a high amount of silanol groups was used. Since the formation of PoO_2 is very likely under the experimental conditions, the question arises as to whether the PoO_2 formed was deposited upstream of the chromatography column in the transport line between the catcher foil oven and the first gradient oven, or whether the species formed on the surface is in fact PoO_2. Unlike hydrogen, oxygen does not react with the quartz surface but can only diffuse into the glass.[115,116]

From studies of the sublimation behaviour of PoO_2 from metal surfaces, the sublimation temperature of the compound was determined to be 885 °C.[114] Chromatographic studies in which polonium was vaporised from an UO_2 ceramic in an oxygen atmosphere at high temperatures (950-1140 °C) confirm the low volatility of the compound.[117] It can therefore be assumed that PoO_2 is deposited at high temperatures, which would rather indicate a deposition of PoO_2 in the temperature minimum before the chromatography column.
A closer look at the deposition at (360 ± 10) °C shows that the peak extends over a wide temperature range. This underlines the theory of a surface reaction, as these are known to lead to broader peaks.[60,118] The deposition of the high-temperature species begins at temperatures of (400 ± 10) °C, which is not far from the temperature between the catcher foil furnace and the first gradient furnace ((460 ± 20) °C). If one also considers that the turbulence in the gas flow through the catcher foil leads to significantly more wall contacts of the molecule which are not taken into account by the Monte Carlo simulation, it cannot be ruled out that the deposition in the column at (360 ± 10) °C and the deposition in front of the column are caused by the same species.
The presence of TiPo seems unlikely due to the high temperature in the catcher foil oven at which the compound already dissociates.[103]

It is therefore conceivable that the reaction in the gas phase as well as the simultaneous surface reaction both lead to the formation of PoO_2 (in this case, the deposition in the transport line and the deposition at (360 ± 10) °C would both be caused by polonium dioxide), or that both reactions lead to different products and thus three species were observed in the column. To answer this question, a further experiment would be necessary in which polonium is analysed thermochromatographically on an unreactive quartz surface (to exclude surface reactions) in a helium and oxygen atmosphere.

In order to further investigate the surface reaction in this experiment, the extension of the Monte Carlo simulation by D. Dietzel et al. with the inputs from table 4.8 was used to determine the energy barrier between physisorption and chemisorption. As in the previous experiment, the adsorption enthalpies were varied in the range of the determined error in order to also determine

the error of the energy barrier. The best agreement between the simulation and the experimental data was found at an energy barrier of

$$(136 \pm 4)\,\mathrm{kJ/mol}$$

(see also figure 7.3 in the appendix).

The determined energy barrier matches the energy barrier of the thermochromatography experiment in helium and hydrogen atmosphere (Rez2023-Po204-TC-H2) within the scope of the error which further emphasises that surface effects are the decisive factor in this experiment as well.

5.1.4 Determination of the adsorption enthalpy of ^{204}Bi in pure helium atmosphere (Rez2023-Po204-Bi204-TC-He)

Two deposition temperatures were observed in the column during thermochromatographic analysis of bismuth. As shown in section 4.1.3, a large part of the species deposited at (350 ± 10) °C was also deposited in the temperature minimum of the transport line ((370 ± 20) °C). This species with an adsorption enthalpy of $-157^{+6}_{-8}\,\mathrm{kJ/mol}$ is therefore the predominant species. As no reactions in the gas phase or with the surface are expected under the chosen experimental conditions, these depositions are most likely due to elemental bismuth. Although the formation of intermetallic bismuth-titanium compounds such as Ti_2Bi, Ti_3Bi or Ti_4Bi cannot be ruled out, it is assumed that such a molecule would not be heated-out form the catcher foil at the selected temperature due to the high mass and the low volatility of this compound.[93,119,120]
As already explained in section 2.3.2, there are no experimentally determined adsorption enthalpies of bismuth on quartz, only theoretically calculated values. However, the value calculated by V. Pershina et al. using the computation suite ADF BAND (-153 kJ/mol (revPBE)) is in excellent agreement with the adsorption enthalpy determined experimentally here.[95] This supports the assumption that the deposition is in fact caused by elemental bismuth.

Since reactions in the gas phase are excluded due to the lack of reactive gases, as well as reactions on the surface due to the choice of an unreactive quartz glass, the question arises as to what could have caused the deposition at (224 ± 7) °C. Due to the very low intensity of the peak, it is conceivable that traces of impurities in the gas phase could have led to the formation of a second species. It is also conceivable that the deposition was originally ^{204}Po, which was possibly heated-out from the catcher foil very late, then froze at this temperature after the end of the experiment and then decayed to ^{204}Bi before the measurement. In addition, it cannot be ruled out that both depositions measured for bismuth are actually the same peak with a larger tailing, as due to the very low intensity of the deposition, it could only be found in the first place because 4 cm pieces were measured in this area of the column instead of 2 cm pieces. As it seems likely that the deposition at (224 ± 7) °C was caused by (unwanted) secondary effects, it is almost impossible to assign a chemical form to this deposition.

5.2 Isothermal measurements of ^{216}Po on quartz glass and Teflon

5.2.1 Isothermal measurement of ^{216}Po on quartz glass (GSI2024-Po216-IC-Quartz)

In order to gain insight into the adsorption enthalpy of $^{216}\mathrm{Po}$ on quartz glass from the relative breakthrough through the column, the expected integrated chromatogram (see figure 5.2) was simulated using the Monte Carlo simulation assuming the adsorption enthalpy determined in the thermochromatography experiment of elemental $^{204}\mathrm{Po}$ on quartz glass in helium (Rez2023-Po204-Bi204-TC-He, section 4.1.2). This is justified, since under the selected experimental conditions neither reactions in the gas phase nor with the selected unreactive quartz glass are to be expected, which is why elemental polonium can be assumed. The input parameters used are shown in table 5.1 on the right, the errors resulted from the determined error of the adsorption enthalpy ((-86 $\pm$ 5) kJ/mol). Since the detection in this experiment takes place online, the lifetime of the simulated atoms is determined based on the half-life and not by the duration of the experiment.

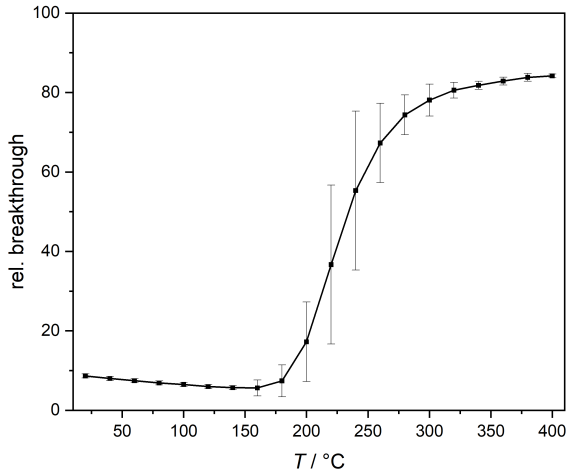

Figure 5.2: Relative breakthrough against temperature for elemental ^{216}Po after a 34 cm unreactive quartz column simulated using the Monte Carlo method.

Table 5.1: Selected input parameters for the simulation of the integrated chromatogram in figure 5.2. Here, T is the temperature, p the pressure, M the molar mass, F the proportion of helium in the gas phase, ρ the density at the boiling point, Q the gas flow, r the inner radius of the column, τ_0 the period of oscillation at the surface, $t_{1/2}$ is the half-life and L the length of the column.

Input parameter	value	reference
ΔH_{ads} / kJ/mol	86 ± 5	see section 4.1.2
M_{Po} / g/mol	204	-
M_{He} / g/mol	4	-
F_{He}	1	-
ρ_{Po} / g/cm^3	9.2	[78]
ρ_{He} / g/cm^3	0.125	[99]
Q / sccm/min	2900	-
r / cm	0.20	-
p / bar	1.252	-
τ_0 / s^{-1}	$0.2 \cdot 10^{-12}$	[60]
T / °C	20-400	-
$t_{1/2}$ / s	0.145	[21]
L / cm	34	-

The simulation shows that significantly higher temperatures than the deposition temperature observed for elemental ^{204}Po in the thermochromatography experiments are required to achieve a measurable breakthrough through the column. This is due to the significantly shorter half-life of ^{216}Po (145 ms) compared to ^{204}Po (3.53 h).[21]

The high measured breakthrough of $(35 \pm 4)\%$ is somewhat surprising in view of the simulation in figure 5.2, as even with the selected gas flow of 2900 sccm/min, a breakthrough of only around 10% would be expected at room temperature.
If one considers the average jump length of about 4 cm calculated in the simulation, it becomes clear that a simulated atom in the column has only very few (less than ten) wall contacts after a "long jump". This is necessary in order not to lose too much activity due to the decay of ^{216}Po. The simulation assumes that every contact with the wall leads to adsorption, but this does not correspond to reality as atoms can also be elastically scattered from the surface. The value that indicates the probability that a wall contact leads to adsorption is called the sticking coefficient. In reality this coefficient is less than one, but is assumed to be unity in the simulation. Consequently, the number of atoms decaying in the column is overestimated by the simulation and the real breakthrough by atoms that have had few wall contacts, which in turn do not all lead

to adsorption, is greater than the simulation suggests. This plays a particularly important role in the isothermal measurements of the short-lived ^{216}Po carried out within this thesis, as the gas flow is significantly higher and therefore the number of wall contacts is much smaller than in the conducted thermochromatography experiments. In addition, there is the well-known problem of the diffusion coefficient, which cannot be calculated accurately enough at every temperature using Gilliland's formula.[60,72,73] Therefore, imprecise diffusion coefficients can also lead to a miscalculation of the amount of contacts with the wall.
Since the adsorption enthalpy of elemental polonium on quartz glass could be reproduced in three different experiments in the scope of this thesis, it can be assumed that an adsorption enthalpy of similar magnitude and thus no breakthrough would be expected in this experiment at room temperature. It follows, that the breakthrough measured here only involves those atoms that have shown very little interaction with the surface. Those which did have longer interaction times with the column, all decayed within it. Due to the assumption of the simulation that every wall contact leads to adsorption, as well as possible further influences due to not exactly calculated diffusion coefficients, it is not possible to reproduce the experimental result in the simulation. The measured "background breakthrough" of atoms with little to no interactions with the surface should be mostly independent of the material, as long as the affinity to the surface is high enough at room temperature.

Based on the above considerations, it can be assumed that in this measurement every atom that was able to interact with the quartz surface long enough has decayed in the column. From this consideration, a lower limit of the adsorption enthalpy can be determined using the Monte Carlo simulation. All experimental input parameters were chosen so that the lower limit of the adsorption enthalpy is obtained (see table 5.2).

Table 5.2: Inputs for the Monte Carlo simulation to determine the lower limit of the adsorption enthalpy of ^{216}Po on quartz glass and Teflon. Here, T is the temperature, p the pressure, M the molar mass, F the proportion of helium in the gas phase, ρ the density at the boiling point, Q the gas flow, r the inner radius of the column, τ_0 the period of oscillation at the surface and $t_{1/2}$ is the half-life.

Input parameter	value	reference
M_{Po} / g/mol	204	-
M_{He} / g/mol	4	-
F_{He}	1	-
ρ_{Po} / g/cm^3	9.2	[78]
ρ_{He} / g/cm^3	0.125	[99]
Q / sccm/min	2870	-
r / cm	0.21	-
p / bar	1.258	-
τ_0 / s^{-1}	$0.2 \cdot 10^{-12}$	[60]
T / °C	20	-
$t_{1/2}$ / s	0.145	[21]

Up to an adsorption enthalpy of

$$-\Delta H_{\mathrm{ads}} \geq 58\,\mathrm{kJ/mol},$$

the simulation shows a breakthrough of less than 10% through the column, which therefore represents the lower limit of the adsorption enthalpy.

In order to better narrow down the adsorption enthalpy of $^{216}\mathrm{Po}$ on quartz glass, the column must be heated to temperatures of up to 300-350 °C (complete breakthrough). To this end, initial tests at 130 °C were carried out with the setup used here. However, the hot helium, which was fed directly into the detector led to a significant increase in noise, which meant that measurements were no longer possible. Active cooling of the detector would probably only provide a remedy at moderate temperatures, as the hot helium could not be cooled down enough in the short flow time through the cooled detector. The design of a different experimental setup or the use of different detectors, for example more resistant polycrystalline CVD (chemical vapour deposition) diamond detectors, is therefore required to be able to heat the quartz column.[121]

To obtain an estimate of the magnitude of the sticking coefficient, the Monte Carlo simulation was modified so that not every wall contact leads to adsorption. For this purpose, the sticking coefficient was introduced as a new parameter and varied, assuming the adsorption enthalpy determined in the thermochromatography experiment in pure helium ((86 ± 5) kJ/mol), until the best agreement of the breakthrough with the experiment was achieved. The error in the sticking coefficient resulted from the uncertainty of the breakthrough. Using the modified Monte Carlo simulation (with the inputs from table 5.1, the simulation was only conducted for 20 °C), a sticking coefficient of

$$33^{+5}_{-4}\%$$

was determined.
Sticking coefficients have been measured for various simpler molecules such as N_2, O_2 or H_2O and even complex molecules such as proteins on different surfaces. It was found that the sticking coefficient generally seems to depend on the nature of the surface and the substrate, as well as on the temperature, the angle of incidence and the kinetic energy of the substrate before the wall contact. Sticking coefficients from close to zero to unity have been measured and predicted for different systems. Therefore, the here determined sticking coefficient seems plausible.[122–125]

5.2.2 Isothermal measurement of ^{216}Po on Teflon (GSI2024-Po216-IC-Teflon)

The determined breakthrough after the 34 cm Teflon column ((28 ± 4) %) is a little smaller but still in the range of the error identical to the breakthrough measured on quartz. On the one hand, this supports the theory of "background breakthrough" described above and, at the same time, means that polonium has a similar affinity towards Teflon as to quartz. It can be deduced that in experiments with not only $^{216}\mathrm{Po}$ but also in future experiments with livermorium, long Teflon capillaries upstream of the column must be avoided at all costs.

Since in this experiment it can be suspected that all atoms that had sufficient interaction with

the surface decayed in the column as well, only the lower limit of the adsorption enthalpy can be determined by the simulation. With the input parameters from table 5.2 (only the pressure was adjusted to 1266 mbar), the lower limit of the adsorption enthalpy of $^{216}\mathrm{Po}$ on Teflon in helium was determined to be

$$-\Delta H_{\mathrm{ads}} \geq 58\,\mathrm{kJ/mol}.$$

It is not possible to estimate the sticking coefficient of polonium on Teflon because the adsorption enthalpy is not known with sufficient accuracy.

6

Summary and outlook

As part of this thesis, the adsorption enthalpy of elemental ^{204}Po on quartz glass in helium atmosphere was determined in a thermochromatography experiment and confirmed in two further experiments with hydrogen and oxygen as reactive gases. The determined adsorption enthalpy is in very good agreement with the adsorption enthalpy of elemental polonium on quartz glass published in the annual report from the Paul Scherrer Institut from 1996.[94] In the thermochromatography experiments with hydrogen and oxygen, a less volatile species could be observed, which is formed from the reaction of polonium with the quartz surface. It was suspected that this species is an oxide, possibly PoO_2.
The possibility of polonium reacting with quartz with a high amount of silanol groups on the surface clearly shows the importance of reactions with the solid phase and not just the gas phase in chromatography experiments with both homologues and superheavy elements. This discovery thus contributes to a better understanding of future chromatography experiments and underlines the importance of knowing the exact surface structure of the solid phase.
Due to the determined adsorption enthalpies, the chemical experiments of the homologue of livermorium carried out here lay the foundation for future investigations of the still chemically uncharacterised superheavy element.
The surface reaction of ^{204}Po was further investigated as part of another beam time, which was not part of this thesis. In three different (not yet fully evaluated) thermochromatography experiments in helium atmosphere, but with differently reactive quartz surfaces, it was possible to reproduce the deposition of the low-volatile species observed in this thesis in the experiments with hydrogen and oxygen on those surfaces with many silanol groups. The experiments carried out on the basis of this thesis thus clearly prove the surface reaction of polonium. Furthermore, a thermochromatography experiment with helium and oxygen on unreactive quartz has probably shown that the species formed on the surface is most likely PoO_2, since the same peaks as seen through the surface reaction could be reproduced.
Following, in future chromatography experiments on quartz glass, the production process used and the entire thermal history of the quartz glass must always be known. In addition, suitable analytical methods should be established with which the OH-content of the glass on the surface can always be verified. This also applies to coated detectors such as the COMPACT detector.

The decay of ^{204}Po to ^{204}Bi made it possible to determine the adsorption enthalpy of elemental bismuth on quartz glass, for which no experimental data had previously been available. The determined enthalpy is in excellent agreement with the theoretically by V. Pershina et al. predicted one.[95] The new obtained experimental data will thus provide a better understanding of the chemistry of the superheavy homologue moscovium.
As a large part of the bismuth was trapped in front of the chromatography column, the experiments had comparatively low statistics. It would therefore make sense to investigate bismuth (and any surface reactions of bismuth) in separate experiments.

The isothermal studies of the short-lived isotope ^{216}Po show that the adsorption enthalpy of polonium on Teflon must be of a similar order of magnitude to that on quartz glass. This must be taken into account not only for the design of an apparatus for further investigations of ^{216}Po, but also for the investigation of the superheavy homologue livermorium. The investigations of the short-lived isotope done within this thesis therefore lay the foundation for the development of a new chromatography apparatus with which isotopes with extremely short half-lives can also be chemically analysed.
In order to be able to better limit the adsorption enthalpy of ^{216}Po on quartz glass and Teflon, it is necessary to heat the chromatography column. For this purpose, a new detection system must be designed that can cool down the hot helium quickly enough, so that the noise in the detector can be reduced. Several ideas are already being worked on to achieve this goal.

A summary of all the adsorption enthalpies determined in this thesis can be found in table 6.1.

Table 6.1: Summary of the adsorption enthalpies determined for each species in all experiments. Depositions before the chromatography column are not shown.

Experiment abbreviation	nuclide	$-\Delta H_{\mathrm{ads},1}$ / kJ/mol	$-\Delta H_{\mathrm{ads},2}$ / kJ/mol
Rez2023-Po204-Bi204-TC-He	^{204}Po	86 ± 5	-
Rez2023-Po204-Bi204-TC-He	^{204}Bi	124^{+4}_{-7}	157^{+6}_{-8}
Rez2023-Po204-TC-H2	^{204}Po	84^{+4}_{-5}	149^{+4}_{-6}
Rez2023-Po204-TC-O2	^{204}Po	75^{+3}_{-4}	152^{+6}_{-11}
GSI2024-Po216-IC-Quartz	^{216}Po	≥ 58	-
GSI2024-Po216-IC-Teflon	^{216}Po	≥ 58	-

Bibliography

[1] D. Mendeleev, *Z. Chem.* **1869**, *12*, 405–406.

[2] M. Binnewies, M. Finze, M. Jäckel, P. Schmidt, H. Willner, G. Rayner Canham, *Allgemeine und Anorganische Chemie*, Springer Spektrum, Berlin, 3rd ed., **2016**.

[3] E. Scerri, *The periodic table - Its story and its significance*, Oxford University Press, New York, 2nd ed., **2020**.

[4] A. Türler, V. Pershina, *Chem. Rev.* **2013**, *113*, 1237–1312.

[5] M. Schädel, *Angew. Chem. Int. Ed.* **2006**, *45*, 368–401.

[6] M. Schädel, *Philos. Trans. Royal Soc. A* **2015**, *373*, 1–15.

[7] S. Hofmann, *The chemistry of superheavy elememts - Properties and syntheses of superheavy elements*, Kluwer Academic Publishers, Dordrecht, 1st ed., **2004**.

[8] D. C. Hoffman, D. A. Shaughnessy, *Handbook of Nuclear Chemistry - Elements and isotopes: Formation, transformation, distribution - Superheavy elements*, *Vol. 2*, Springer, Dordrecht, 2nd ed., **2011**.

[9] C. E. Düllmann, *Nuclear- and radiochemistry - Modern applications - Radioelements: Transactinides*, *Vol. 2*, De Gruyter, Berlin, 1st ed., **2016**.

[10] S. L. Glashow, *Interactions: A journey through the mind of a particle physicists and the matter of this world*, Warner Books, New York, 1st ed., **1988**.

[11] P. A. M. Dirac, *Proc. Math. Phys. Eng. Sci.* **1929**, *123*, 714–733.

[12] P. Pyykkö, *Chem. Rev.* **1988**, *88*, 563–594.

[13] P. Pyykkö, J.-P. Desclaux, *Acc. Chem. Res.* **1979**, *12*, 276–281.

[14] K. S. Pitzer, *Acc. Chem. Res.* **1979**, *12*, 271–276.

[15] F. Calco, E. Pahl, M. Wormit, P. Schwerdtfeger, *Angew. Chem. Int. Ed.* **2013**, *52*, 7583–7585.

[16] P. Schwerdtfeger, *Heteroatom Chem.* **2002**, *13*, 578–584.

[17] A. Carrington, I. R. McNab, C. A. Montgomerie, *J. Phys. B: At. Mol. Opt. Phys.* **1989**, *22*, 3551–3586.

[18] J.-V. Kratz, K. H. Lieser, *Nuclear and radiochemistry - fundamentals and applications*, Wiley-VCH, Weinheim, 3rd ed., **2013**.

[19] B. Eichler, R. Eichler, *The chemistry of superheavy elememts - Gas-phase adsorption chromatographic determination of thermochemical data and empirical methods for their estimation*, Kluwer Academic Publishers, Dordrecht, 1st ed., **2004**.

[20] A. F. Novgorodov, F. Rösch, N. A. Korolev, *Handbook of Nuclear Chemistry - Instrumentation, separation techniques, enviromental issues - Radiochemical separations by thermochromatography*, *Vol. 2*, Springer, Dordrecht, 2nd ed., **2011**.

[21] S. Y. F. Chu, L. P. Ekström, R. B. Firestone, *The Lund/LBNL nuclear data search*, **1999**, `http://nucleardata.nuclear.lu.se/toi/`, last accessed on 24.04.24 at 18:19.

[22] A. Yakushev, Y. Wei, C. E. Düllmann, *Towards chemistry beyond moscovium (Mc, Z = 115)*, **2022**, `https://indico.gsi.de/event/13786/`, last accessed on 09.05.24 at 11:17.

[23] F. Rösch, *Nuclear-and radiochemistry*, *Vol. 1: Introduction*, De Gruyter, Berlin, 2nd ed., **2022**.

[24] T. Fényes, *Handbook of nuclear chemistry - Basics of nuclear science - Basic properties of the atomic nucleus*, *Vol. 1*, Springer, Dordrecht, 2nd ed., **2011**.

[25] E. Caurier, G. Martínez-Pinedo, F. Nowacki, A. Poves, A. P. Zuker, *Rev. Mod. Phys.* **2005**, *77*, 428–483.

[26] C. F. v. Weizsäcker, *Z. für Phys.* **1935**, *96*, 431–458.

[27] M. G. Mayer, *Phys. Rev.* **1969**, *75*, 1969–1970.

[28] O. Haxel, J. H. D. Jensen, H. E. Suess, *Phys. Rev.* **1949**, *75*, 1766.

[29] Y. T. Oganessian, V. K. Utyonkov, *Rep. Prog. Phys.* **2015**, *78*, 036301.

[30] P. Möller, *Eur. Phys. J. A* **2023**, *59*, 1–15.

[31] M. Schädel, *Radiochim. Acta* **2012**, *100*, 579–604.

[32] S. A. Giuliani, Z. Matheson, W. Nazarewicz, E. Olsen, P.-G. Reinhard, J. Sadhukhan, B. Schuetrumpf, N. Schunck, P. Schwerdtfeger, *Rev. Mod. Phys.* **2019**, *91*, 011001.

[33] C. E. Düllmann, *Angew. Chem. Int. Ed.* **2019**, *58*, 4070–4072.

[34] D. Ackermann, C. Theisen, *Phys. Scripta* **2017**, *92*, 083002.

[35] G. Münzberg, *Lecture notes in physics - Extended density functionals in nuclear structure physics - The structure of heavy nuclei - from lead to superheavy elements*, *Vol. 641*, Springer Nature, Berlin, 1st ed., **2004**.

[36] C. E. Düllmann, M. Block, F. P. Heßberger, J. Khuyagbaatar, B. Kindler, J. V. Kratz, B. Lommel, G. Münzenberg, V. Pershina, D. Renisch, M. Schädel, A. Yakushev, *Radiochim. Acta* **2022**, *110*, 417–439.

[37] J. Magill, R. Dreher, Z. Sóti, *Karlsruher Nuklidkarte*, Nucleonica, Karlsruhe, 10th ed., **2018**.

[38] S. Raeder, D. Ackermann, H. Backe, R. Beerwerth, J. C. Berengut, M. Block, A. Borschevsky, B. Cheal, P. Chhetri, C. E. Düllmann, V. A. Dzuba, E. Eliav, J. Even, R. Ferrer, V. V. Flambaum, S. Fritzdche, F. Giacoppo, S. Götz, F. P. Heßberger, M. Huyse, U. Kaldor, O. Kaleja, J. Khuyagbaatar, P. Kunz, M. Laatiaoui, F. Lautenschläger, W. Lauth, A. K. Mistry, E. M. Ramirez, W. Nazarewicz, S. G. Porsev, M. S. Safronova, U. I. Safronova, B. Schuetrumpf, P. V. Duppen, T. Walther, C. Wraith, A. Yakushev, *Phys. Rev. Lett.* **2018**, *120*, 232503.

[39] O. R. Smits, C. E. Düllmann, P. Indelicato, W. Nazarewicz, P. Schwerdtfeger, *Nat. Rev. Phys.* **2024**, *6*, 86–98.

[40] V. Pershina, *C R Chim* **2020**, *23*, 255–265.

[41] L. G. Sobotka, V. E. Viola, *Handbook of nuclear chemistry - Basics of nuclear science - Nuclear Reactions*, *Vol. 1*, Springer, Dordrecht, 2nd ed., **2011**.

[42] G. Münzberg, M. Gupta, *Handbook of Nuclear Chemistry - Elements and isotopes: Formation, transformation, distribution - Production and identification of transactinide elements*, *Vol. 2*, Springer, Dordrecht, 2nd ed., **2011**.

[43] A. Nasirov, K. Kim, G. Mandaglio, G. Giardina, A. Muminov, Y. Kim, *Eur. Phys. J. A* **2013**, *49*, 1–14.

[44] V. I. Zagrebaev, Y. Aritomo, M. G. Itkis, Y. T. Oganessian, *Phys. Rev. C* **2001**, *65*, 014607.

[45] D. J. Hinde, M. Dasgupta, E. C. Simpson, *Prog. Part. Nucl. Phys.* **2021**, *118*, 103856.

[46] S. Hofmann, *Radiochim. Acta* **2011**, *99*, 405–428.

[47] M.-S. Bertrams, K. Hermainski, J.-M. Mörsdorf, J. Ballmann, C. Kerzig, *Chem. Sci.* **2023**, *14*, 8583–8591.

[48] V. Pershina, *Radiochim. Acta* **2011**, *99*, 459–476.

[49] V. Pershina, *The chemistry of superheavy elememts - Theoretical chemistry of the heaviest elements*, Kluwer Academic Publishers, Dordrecht, 1st ed., **2004**.

[50] P. Atkins, J. Paula, *Atkins' physical chemistry*, Oxford University Press, Oxford, 8th ed., **2006**.

[51] R. Guillaumont, J. P. Adloff, A. Peneloux, *Radiochim. Acta* **1989**, *46*, 169–176.

[52] R. J. Borg, G. J. Dienes, *J. inorg. nucl. Chem.* **1981**, *43*, 1129–1133.

[53] J. M. Gates, C. E. Düllmann, M. Schädel, A. Yakushev, A. Türler, K. Eberhardt, J. V. Kratz, D. Ackermann, L.-L. Andersson, M. Block, W. Brüchle, J. Dvorak, H. G. Essel, P. A. Ellison, J. Even, U. Forsberg, J. Gellanki, A. Gorshkov, R. Graeger, K. E. Gregorich, W. Hartmann, R.-D. Herzberg, F. P. Heßberger, D. Hild, A. Hübnrt, E. Jäger, J. Khuyagbaatar, B. Kindler, J. Krier, N. Kurz, S. Lahiri, D. Liebe, B. Lommel, M. Maiti, H. Nitsche, J. P. Omtvedt, E. Parr, D. Rudolph, J. Runke, H. Schaffner, B. Schausten, E. Schimpf, A. Semchenkov, J. Steiner, P. Thörler-Pospiech, J. Uusitalo, M. Wegrzecki, N. Wiehl, *Phys. Rev. C* **2011**, *83*, 054618.

[54] H. W. Gäggler, D. T. Jost, U. Baltensperger, A. Weber, A. Kovacs, D. Vermeulen, A. Türler, *Nucl. Instrum. Methods Phys. Res. Sect. A* **1991**, *309*, 201–208.

[55] A. Türler, G. V. Buklanov, B. Eichler, H. W. Gäggeler, M. Grantz, S. Hübener, D. T. Jost, V. Y. Lebedev, D. Piguet, S. N. Timokhin, A. B. Yakushev, I. Zvara, *J. Alloy. Compd.* **1998**, *271*, 287–291.

[56] C. E. Düllmann, W. Brüchle, R. Dressler, K. Eberhardt, B. Eichler, R. Eichler, H. W. Gäggler, F. Glaus, K. E. Gregorich, D. C. Hoffmann, E. Jäger, D. T. Jost, U. W. Kirbach, D. M. Lee, H. Nitsche, J. B. Patin, V. Pershina, D. Piguet, Z. Qin, M. Schädel, B. Schausten, E. Schimpf, H.-J. Schött, S. Soverna, R. Sudowe, P. Thörle, S. N. Timokhin, N. Trautmann, A. Türler, A. Vahle, G. Wirth, A. B. Yakushev, P. M. Zlelinski, *Nature* **2002**, *418*, 859–862.

[57] D. Borodin, I. Rahinov, P. R. Shirhatti, M. Huang, A. Kandratsenka, D. J. Auerbach, T. Zhong, H. Guo, D. Schwarzer, T. N. Kitsopoulos, A. M. Wodtke, *Science* **2020**, *369*, 1461–1465.

[58] M. Huang, X. Zhou, Y. Zhang, L. Zhou, M. Alducin, B. Jiang, H. Guo, *Phys. Rev. B* **2019**, *100*, 201407.

[59] I. Zvára, *Radiochim. Acta* **1985**, *38*, 95–101.

[60] I. Zvára, *The inorganic radiochemistry of heavy elements*, Springer Science, Luxembourg, 1st ed., **2008**.

[61] M. Králik, *Chem. Zvesti* **2014**, *68*, 1625–1638.

[62] F. Huber, J. Berwanger, S. Polesya, S. Mankovsky, H. Ebert, F. J. Giessibl, *Science* **2019**, *366*, 235–238.

[63] S. T. Ceyer, *Ann. Rev. Phys. Chem.* **1988**, *39*, 479–510.

[64] A. Dąbrowski, *Adv. Colloid Interface Sci.* **2001**, *93*, 135–224.

[65] D. Dietzel, A. Yakushev, C. E. Düllmann, *J. Radioanal. Nucl. Chem. (accepted)* **2024**.

[66] C. Gerhard, R. Köhler, *Appl. Surf. Sci.* **2024**, *644*, 158669.

[67] A. Yakushev, L. Lens, C. E. Düllmann, J. Khuyagbaatar, E. Jäger, J. Krier, J. Runke, H. M. Albers, M. Asai, M. Block, J. Despotopulos, A. D. Nitto, K. Eberhardt, U. Forsberg, P. Golubev, M. Götz, S. Götz, H. Haba, L. Harkness-Brennan, R.-D. Herzberg, F. P. Heßberger, D. Hinde, A. Hübner, D. Judson, B. Kindler, Y. Komori, J. Konki, J. V. Kratz, N. Kurz, M. Laatiaoui, S. Lahiri, B. Lommel, M. Maiti, A. K. Mistry, C. Mokry, K. J. Moody, Y. Nagame, J. P. Omtvedt, P. Papadakis, V. Pershina, D. Rudolph, L. G. Samiento, T. K. Sato, M. Schädel, P. Scharrer, B. Schausten, D. A. Shaughnessy, J. Steiner, P. Thörle-Pospiech, A. Toyoshima, N. Trautmann, K. Tsukada, J. Uusitalo, K.-O. Voss, A. Ward, M. Wegrzecki, N. Wiehl, E. Williams, V. Yakusheva, *Front. Chem.* **2022**, *10*, 976635.

[68] J. Even, A. Yakushev, C. E. Düllmann, H. Haba, M. Asai, T. K. Sato, H. Brand, A. D. Nitto, R. Eichler, F. L. Fan, W. Hartmann, M. Huang, E. Jäger, D. Kaji, J. Kanaya, Y. Kaneya, J. Khuyagbaatar, B. Kindler, J. V. Kratz, J. Krier, Y. Kudou, N. Kurz, B. Lommel, S. Miyashita, K. Morimoto, K. Morita, M. Murakami, Y. Nagame, H. Nitsche, K. Ooe, Z. Qin, M. Schädel, J. Steiner, T. Sumita, M. Takeyama, K. Tanaka, A. Toyoshima, K. Tsukada, A. Türler, I. Usoltsev, Y. Wakabayashi, Y. Wang, N. Whiel, S. Yamaki, *Science* **2014**, *345*, 1491–1493.

[69] R. Eichler, N. V. Aksenov, A. V. Belozerov, G. A. Bozhikov, V. I. Chepigin, S. N. Dmitriev, R. Dressler, H. W. Gäggler, V. A. Gorshkov, F. Haenssler, M. G. Itkis, A. Laube, V. Y. Lebedev, O. N. Malyshev, Y. T. Oganessian, O. V. Petrushkin, D. Piguet, P. Rasmussen, S. V. Shishkin, A. V. Shutov, A. I. Svirikhin, E. E. Tereshatov, G. K. Vostokin, M. Wegrzecki, A. V. Yeremin, *Nature* **2007**, *447*, 72–75.

[70] C. Z. Mooney, *Monte Carlo simulation*, *Vol. 116*, Sage publications, Thousand Oaks, 1st ed., **1997**.

[71] E. R. Gilliland, *J. Ind. Eng. Chem.* **1934**, *26*, 681–685.

[72] J. C. Giddings, *Dynamics of chromatography - principles and theory*, *Vol. 1*, Marcel Dekker, New York, 1st ed., **1965**.

[73] P. J. Gardner, S. R. Preston, *J. Chem. Eng. Data* **1992**, *37*, 500–502.

[74] K. W. Bagnall, *Comprehensive inorganic chemistry*, *Vol. 2*, Pergamon Press, Oxford, 1st ed., **1973**.

[75] N. N. Greenwood, A. Earnshaw, *Chemistry of the elements*, Elsevier, Amsterdam, 2nd ed., **1997**.

[76] P. Thakur, A. L. Ward, *J. Radioanal. Nucl. Ch.* **2020**, *323*, 27–49.

[77] K. W. Bagnall, *Radiochim. Acta* **1983**, *32*, 153–161.

[78] H. Wiberg, *Lehrbuch der Anorganischen Chemie*, Walter de Gruyter, Berlin, 102nd ed., **2007**.

[79] A. J. Bard, R. Parsons, J. Jordan, *Standard potentials in aqueous solution*, IUPAC, New York, 1st ed., **1985**.

[80] B. Eichler, *Die Flüchtigkeitseigenschaften des Poloniums*, Paul Scherrer Insitut - Forschungsbereich Teilchen und Materie - Labor für Radio- und Umweltchemie, Villigen, **2002**.

[81] C. Housecroft, A. Sharpe, *Inorganic chemistry*, Pearson Education Limited, Harlow, 5th ed., **2018**.

[82] H. Sicius, *Handbuch der chemischen Elemente*, Springer Spektrum, Dormagen, 1st ed., **2020**.

[83] S. Notarrigo, P. Parisi, R. Ricamo, A. Rubbino, *Nucl. Phys.* **1962**, *29*, 507–514.

[84] E. A. Maugeri, J. Neuhausen, R. Eichler, R. Dressler, K. Rijpstra, S. Cottenier, D. Piguet, A. Vögele, D. Schumann, *Radiochim. Acta* **2016**, *104*, 757–767.

[85] E. A. Maugeri, J. Neuhausen, R. Misiak, R. Eichler, R. Dressler, D. Piguet, A. Vögele, D. Schumann, *Radiochim. Acta* **2016**, *104*, 769–779.

[86] E. A. Maugeri, J. Neuhausen, B. G. Prieto, A. Aertes, T. M. Mendonça, T. Stora, R. Eichler, *Radiochim. Acta* **2018**, *106*, 125–134.

[87] A. S. Abakumov, *Russ. Chem. Rev.* **1982**, *51*, 1091–1102.

[88] E. Riedel, C. Janiak, *Anorganische Chemie*, Walter de Gruyter, Berlin, 7th ed., **2007**.

[89] C. E. Mortimer, U. Müller, *Chemie - Das Basiswissen der Chemie*, Georg Thieme Verlag, Stuttgart, 8th ed., **2003**.

[90] F. Weigel, *Angew. Chem-ger. Edit.* **1959**, *71*, 289–316.

[91] B. Eichler, H. Gäggler-Koch, H. Gäggler, *Radiochim. Acta* **1979**, *26*, 193–195.

[92] H. Gäggler, H. Dornhöfer, N. Greulich, B. Eichler, *Radiochim. Acta* **1985**, *38*, 103–106.

[93] S. Hübener, I. Zvára, *Radiochim. Acta* **1980**, *27*, 157–160.

[94] A. Vogt, H. W. Gäggler, A. Türler, *Adsorption gas chromatography with 150-ms 216-Po*, Paul Scherrer Insitut - Forschungsbereich Teilchen und Materie - Labor für Radio- und Umweltchemie, Villingen, **1996**.

[95] V. Pershina, M. Iliaš, A. Yakushev, *Inorg. Chem.* **2021**, *60*, 9796–9804.

[96] A. Yakushev, *Chemical characterization of element 108, hassium and synthesis of new hassium isotopes*, Technische Universität München, München, **2009**.

[97] C. Andre, H. Gauvin, Y. L. Beyec, N. T. Porile, *J. Phys. IV* **1976**, *37*, 5–15.

[98] H. Akima, *J. ACM* **1970**, *17*, 580–602.

[99] J. Satterly, *Rev. Mod. Phys.* **1936**, *8*, 347–357.

[100] *Saturation properties for hydrogen - pressure increments*, **2023**, https://webbook.nist.gov/cgi/fluid.cgi?Action=Load&ID=C1333740&Type=SatT&Digits=5&PLow=.5&PHigh=1.5&PInc=.1&RefState=DEF&TUnit=K&PUnit=atm&DUnit=kg/m3&HUnit=kJ/mol&WUnit=m/s&VisUnit=uPa*s&STUnit=N/m, last accessed on 5.04.24 at 10:14.

[101] A. V. Itterbeek, O. Verbeke, *Cryogenics (Guildf)* **1960**, *1*, 77–80.

[102] D. Dietzel, *Studien zu Flüchtigkeit und Reaktivität kurzlebiger Bi-Radioisotope als Homologe des superschweren Elements Moscovium*, Johannes Gutenberg-Universität Mainz, Mainz, **2021**.

[103] E. S. Prokin, B. S. Aksenov, N. T. Chebotarev, Z. V. Ershova, *Sov. radiochem.* **1979**, *20*, 588–590.

[104] J. Stone, *J. Light. Technol.* **1987**, *5*, 712–733.

[105] J. E. Shelby, *J. Non-cryst. Solids* **1994**, *179*, 138–147.

[106] B. C. Schmidt, F. M. Holtz, J.-M. Bény, *J. Non-Cryst. Solids* **1998**, *240*, 91–103.

[107] J. E. Shelby, *J. Appl. Phys.* **1980**, *51*, 2589–2593.

[108] R. H. Doremus, *Annu. Rev. Mater. Sci.* **1972**, *2*, 93–120.

[109] G. A. Parks, *J. Geophys. Res.* **1984**, *89*, 3997–4008.

[110] H.-P. Boehm, *Angew. Chem. Int. Ed.* **1966**, *5*, 533–622.

[111] A. P. Velmuzhov, M. V. Sukhanov, M. F. Churbanov, T. V.Kotereva, L. V. Shabarova, Y. P. Kirillov, *Inorg. Mater.* **2018**, *54*, 925–930.

[112] A. R. Silin, P. J. Bray, J. C. M. Jr., *J. Non-Cryst. Solids* **1984**, *64*, 185–193.

[113] V. S. Zrerev, A. S. Abakumov, T. N. Ananina, A. D. Khokhlov, *Sov. Radiochem.* **1980**, *22*, 109–113.

[114] K. W. Bagnall, R. W. M. D'Eye, *J. Chem. Soc.* **1954**, *1*, 4295–4299.

[115] M. A. Lamkin, F. L. Riley, R. J. Fordham, *J. Eur. Ceram. Soc.* **1992**, *10*, 347–368.

[116] E. L. Williams, *J. Am. Ceram. Soc.* **1995**, *48*, 190–194.

[117] B. Eichler, V. P. Domanov, *J. Radioanal. Chem.* **1975**, *28*, 143–152.

[118] B. Eichler, *Radiochim. Acta* **1996**, *72*, 19–26.

[119] S. Maruyama, Y. Kado, T. Uda, *J. Phase Equilib. Diff.* **2013**, *34*, 289–296.

[120] G. P. Vassilev, *Cryst. Res. Technol.* **2006**, *41*, 349–357.

[121] H. Kagan, A. Alexopoulos, M. Artuso, F. Bachmair, L. Bäni, M. Bartosik, J. Beacham, H. Beck, V. Bellini, V. Belyaev, B. Bentele, P. Bergonzo, A. Bes, J.-M. Brom, M. Bruzzi, G. Chiodini, D. Chren, V. Cindro, G. Claus, J. Collot, J. Cumalat, A. Dabrowski, R. D'Alessandro, D. Dauvergne, W. de Boer, S. Dick, C. Dorfer, M. Dunser, V. Eremin, G. Forcolin, J. Forneris, L. Gallin-Martel, A. Golubev, A. Gorišek, E. Grigoriev, J. Grosse-Knetter, A. Grummer, B. Gui, M. Guthoff, I. Haughton, B. Hiti, D. Hits, M. Hoeferkamp, T. Hofmann, J. Hosslet, R. Kass, F. Kassel, M. Kis, G. Kramberger, S. Kuleshov, A. Lacoste, S. Lagomarsino, A. L. Giudice, E. Lukosi, C. Maazouzi, I. Mandic, C. Mathieu, M. Menichelli, M. Mikuž, A. Morozzi, J. Moss, R. Mountain, S. Murphy, , M. Muškinja, A. Oh, P. Olivero, D. Passeri, H. Pernegger, R. Perrino, F. Picollo, M. Pomorski, R. Potenza, A. Quadt, A. Re, M. Reichmann, G. Riley, S. Roe, D. Sanz, M. Scaringella, D. Schaefer, C. J. Schmidt, D. S. Smith, S. Schnetzer, S. Sciortino, K. Stenson, R. Stone, C. Sutera, A. Taylor, B. Tannewald, M. Traeger, D. Tromson, W. Trischuk, C. Tuve, J. Velthuis, N. Venturi, E. Vittone, S. Wagner, R. Wallny, J. C. Wang, J. Weingarten, C. Weiss, T. Wengler, N. Wermes, M. Yamouni, M. Zavrtanik, *Nucl. Instrum. Methods Phys. Res.* **2019**, *924*, 297–300.

[122] M. Rose, J. W. Bartha, I. Endler, *Appl. Surf. Sci.* **2010**, *256*, 3778–3782.

[123] L. Vattuone, M. Rocca, C. Boragno, U. Valbusa, *J. Chem. Phys.* **1994**, *101*, 713–725.

[124] D. R. Weaver, W. G. Pitt, *Biomaterials* **1992**, *13*, 577–584.

[125] M.-T. Leu, *Geophys. Res. Lett.* **1988**, *15*, 17–20.

7

Appendix

List of abbreviations

SHE	Superheavy elements
LDM	Liquid drop model
IPM	Independent particle shell model
CN	Compound nucleus
EVR	Evaporation residue
ADS	Accelerator driven system
HSAB	Hard and soft acids and bases
fcc	face-centered cubic
SOC	Spin-orbit coupling
TASCA	Transactinide separator and chemistry apparatus
COLD	Cryo online detector
COMPACT	Cryo online multidetector for physics and chemistry of transactinides
IC	Isothermal chromatography
TC	Thermochromatography
MFC	Mass flow controller
PI	Pressure indicator
HPGe	High purity germanium
DPS	Dew point sensor
PTFE	Polytetrafluoroethylene
PIPS	Passivated implanted planar silicon
MCS	Monte Carlo simulation
EC	Electron capture
CVD	Chemical vapour deposition

List of experiments and experimental parameters

Table 7.2: Summary of all experiments with abbreviations and experimental parameters. Here, Q stands for the gas flow of helium or the reactive gas.

Experiment abbreviation	reactive gas	temperature gradient	Q_{He} / sccm/min	Q_{RG} / sccm/min	column material	quartz type	catcher/ source	isotope
Rez2023-Po204-Bi204-TC-He	-	maximum at (720 ± 20) °C	51	-	quartz glass	unreactive	catcher	^{204}Po ^{204}Bi
Rez2023-Po204-TC-H2	H_2	maximum at (720 ± 20) °C	37.5	12.5	quartz glass	reactive	catcher	^{204}Po
Rez2023-Po204-TC-O2	O_2	maximum at (1030 ± 20) °C	45	5	quartz glass	reactive	catcher	^{204}Po
GSI2024-Po216-IC-DC	-	RT	2900	-	-	-	source	^{216}Po
GSI2024-Po216-IC-Quartz	-	RT	2900	-	quartz glass	unreactive	source	^{216}Po
GSI2024-Po216-IC-Teflon	-	RT	2900	-	PTFE	-	source	^{216}Po

Calculated yields for various reactions

Table 7.3: Calculated yields and cross-sections for the reaction of $^{207}\mathrm{Pb}$ and $^{208}\mathrm{Pb}$ with $^{3}\mathrm{He}$ at various beam energies E_B using the software LISECute++ (Code PACE4, Michigan State University). The table only shows isotopes with yields above 3%. Here, σ symbolizes the cross-section.

Target	E_B / MeV	produced isotope	yield / %	σ / mb
$^{207}\mathrm{Pb}$	50 MeV	$^{205}\mathrm{Po}$	14.9	234
		$^{204}\mathrm{Po}$	66.9	1050
		$^{201}\mathrm{Pb}$	3.0	47.2
$^{207}\mathrm{Pb}$	49 MeV	$^{205}\mathrm{Po}$	18.5	290
		$^{204}\mathrm{Po}$	63.4	993
$^{207}\mathrm{Pb}$	48 MeV	$^{205}\mathrm{Po}$	22.8	356
		$^{204}\mathrm{Po}$	62.1	969
$^{207}\mathrm{Pb}$	47 MeV	$^{205}\mathrm{Po}$	32.8	510
		$^{204}\mathrm{Po}$	51.2	796
$^{207}\mathrm{Pb}$	46 MeV	$^{205}\mathrm{Po}$	39.9	618
		$^{204}\mathrm{Po}$	46.5	720
$^{208}\mathrm{Pb}$	50 MeV	$^{206}\mathrm{Po}$	9.6	151
		$^{205}\mathrm{Po}$	76.5	1210
$^{208}\mathrm{Pb}$	49 MeV	$^{206}\mathrm{Po}$	8.0	126
		$^{205}\mathrm{Po}$	77.9	1220
$^{208}\mathrm{Pb}$	48 MeV	$^{206}\mathrm{Po}$	14.4	226
		$^{205}\mathrm{Po}$	73.1	1150
$^{208}\mathrm{Pb}$	47 MeV	$^{206}\mathrm{Po}$	18.6	290
		$^{205}\mathrm{Po}$	71.8	1120
$^{208}\mathrm{Pb}$	46 MeV	$^{206}\mathrm{Po}$	25.4	395
		$^{205}\mathrm{Po}$	62.3	969

Table 7.4: Calculated yields and cross-sections for the reaction of ^{48}Ti with ^{3}He at various beam energies E_B using the software LISECute++ (Code PACE4, Michigan State University). The table only shows isotopes with yields above 3%. Here, σ symbolizes the cross-section.

Target	E_B / MeV	produced isotope	yield / %	σ / mb
^{48}Ti	50 MeV	^{47}Ti	26.1	228
		^{46}Sc	3.6	31.5
		^{44}Sc	26.0	227
		^{44}Ca	7.9	69.1
		^{43}Ca	3.3	28.9
		^{42}K	4.6	40.2
		^{38}Cl	3.1	27.1
^{48}Ti	49 MeV	^{48}V	4.7	41.2
		^{47}Ti	27.0	237
		^{46}Sc	3.8	33.3
		^{44}Sc	23.8	209
		^{44}Ca	9.0	79.0
		^{42}K	3.5	30.7
		^{41}K	3.9	34.2
^{48}Ti	48 MeV	^{48}V	5.3	46.7
		^{47}Ti	24.8	218
		^{46}Sc	4.2	37.0
		^{44}Sc	23.9	210
		^{44}Ca	7.9	69.6
		^{42}K	4.6	40.5
		^{41}K	3.7	32.6
		^{38}Cl	3.6	31.7
^{48}Ti	47 MeV	^{48}V	4.9	43.3
		^{47}Ti	24.8	219
		^{47}Sc	3.2	28.3
		^{44}Sc	24.2	214
		^{44}Ca	7.3	64.5
		^{42}Ca	3.1	27.4
		^{42}K	6.9	61.0
		^{41}K	3.1	27.4
		^{38}Cl	3.8	33.6
^{48}Ti	46 MeV	^{48}V	5.1	45.2
		^{47}Ti	26.5	235
		^{45}Sc	3.3	29.3
		^{44}Sc	24.4	216
		^{44}Ca	7.3	64.7
		^{42}K	5.8	51.4
		^{41}K	3.9	34.6

Temperature gradients for thermochromatography

Table 7.5: Measured (T_{exp}) and interpolated (T_{int}) temperatures using the method Akima spline applied to the chromatography column for the thermochromatography experiments in just helium and with hydrogen (Rez2023-Po204-Bi204-TC-He and Rez2023-Po204-TC-H2, index 1), as well as with oxygen (Rez2023-Po204-TC-O2, index 2) for the column from 0-33 cm.

L / cm	$T_{\mathrm{exp},1}$	$T_{\mathrm{int},1}$	$T_{\mathrm{exp},2}$	$T_{\mathrm{int},2}$
0	20 ± 7	20 ± 7	58 ± 7	58 ± 7
1		20 ± 7		90 ± 7
2	20 ± 7	20 ± 7	119 ± 7	119 ± 7
3		45 ± 7		137 ± 7
4	80 ± 7	80 ± 7	166 ± 7	166 ± 7
5		124 ± 7		310 ± 10
6	188 ± 7	188 ± 7	520 ± 10	520 ± 10
7		380 ± 10		730 ± 20
8	580 ± 20	580 ± 20	930 ± 20	930 ± 20
9		660 ± 20		1030 ± 20
10	710 ± 20	710 ± 20	990 ± 20	990 ± 20
11		720 ± 20		830 ± 20
12	700 ± 20	700 ± 20	660 ± 20	660 ± 20
13		520 ± 20		530 ± 20
14	370 ± 20	370 ± 20	460 ± 20	460 ± 20
15		450 ± 20		560 ± 20
16	550 ± 20	550 ± 20	670 ± 20	670 ± 20
17		560 ± 20		670 ± 10
18	570 ± 10	570 ± 10	670 ± 10	670 ± 10
19		560 ± 10		660 ± 10
20	560 ± 10	560 ± 10	650 ± 10	650 ± 10
21		550 ± 10		630 ± 10
22	530 ± 10	530 ± 10	620 ± 10	620 ± 10
23		520 ± 10		590 ± 10
24	500 ± 10	500 ± 10	560 ± 10	560 ± 10
25		480 ± 10		540 ± 10
26	460 ± 10	460 ± 10	520 ± 10	520 ± 10
27		440 ± 10		500 ± 10
28	410 ± 10	410 ± 10	480 ± 10	480 ± 10
29		390 ± 10		460 ± 10
30	370 ± 10	370 ± 10	440 ± 10	440 ± 10
31		350 ± 10		430 ± 10
32	340 ± 10	340 ± 10	410 ± 10	410 ± 10
33		320 ± 10		400 ± 10

Table 7.6: Measured (T_{exp}) and interpolated (T_{int}) temperatures using the method Akima spline applied to the chromatography column for the thermochromatography experiments in just helium and with hydrogen (Rez2023-Po204-Bi204-TC-He and Rez2023-Po204-TC-H2, index 1), as well as with oxygen (Rez2023-Po204-TC-O2, index 2) for the column from 34-66 cm.

L / cm	$T_{\mathrm{exp},1}$	$T_{\mathrm{int},1}$	$T_{\mathrm{exp},2}$	$T_{\mathrm{int},2}$
34	310 ± 10	310 ± 10	390 ± 10	390 ± 10
35		295 ± 7		390 ± 10
36	283 ± 7	283 ± 7	380 ± 10	380 ± 10
37		273 ± 7		370 ± 10
38	263 ± 7	263 ± 7	370 ± 10	370 ± 10
39		252 ± 7		360 ± 10
40	242 ± 7	242 ± 7	360 ± 10	360 ± 10
41		234 ± 7		360 ± 10
42	224 ± 7	224 ± 7	360 ± 10	360 ± 10
43		220 ± 7		360 ± 10
44	212 ± 7	212 ± 7	350 ± 10	350 ± 10
45		206 ± 7		350 ± 10
46	199 ± 7	199 ± 7	350 ± 10	350 ± 10
47		193 ± 7		340 ± 10
48	187 ± 7	187 ± 7	330 ± 10	330 ± 10
49		182 ± 7		330 ± 10
50	177 ± 7	177 ± 7	320 ± 10	320 ± 10
51		169 ± 7		310 ± 10
52	162 ± 7	162 ± 7	300 ± 10	300 ± 10
53		155 ± 7		287 ± 7
54	149 ± 7	149 ± 7	277 ± 7	277 ± 7
55		142 ± 7		267 ± 7
56	136 ± 7	136 ± 7	257 ± 7	257 ± 7
57		130 ± 7		247 ± 7
58	124 ± 7	124 ± 7	238 ± 7	238 ± 7
59		118 ± 7		229 ± 7
60	113 ± 7	113 ± 7	220 ± 7	220 ± 7
61		107 ± 7		208 ± 7
62	102 ± 7	102 ± 7	197 ± 7	197 ± 7
63		98 ± 7		190 ± 7
64	93 ± 7	93 ± 7	183 ± 7	183 ± 7
65		88 ± 7		173 ± 7
66	84 ± 7	84 ± 7	164 ± 7	164 ± 7

Table 7.7: Measured (T_{exp}) and interpolated (T_{int}) temperatures using the method Akima spline applied to the chromatography column for the thermochromatography experiments in just helium and with hydrogen (Rez2023-Po204-Bi204-TC-He and Rez2023-Po204-TC-H2, index 1), as well as with oxygen (Rez2023-Po204-TC-O2, index 2) for the column from 67-100 cm.

L / cm	$T_{\mathrm{exp},1}$	$T_{\mathrm{int},1}$	$T_{\mathrm{exp},2}$	$T_{\mathrm{int},2}$
67		77 ± 7		157 ± 7
68	74 ± 7	74 ± 7	150 ± 7	150 ± 7
69		72 ± 7		141 ± 7
70	70 ± 7	70 ± 7	133 ± 7	133 ± 7
71		65 ± 7		127 ± 7
72	62 ± 7	62 ± 7	121 ± 7	121 ± 7
73		58 ± 7		114 ± 7
74	55 ± 7	55 ± 7	107 ± 7	107 ± 7
75		52 ± 7		102 ± 7
76	49 ± 7	49 ± 7	97 ± 7	97 ± 7
77		45 ± 7		92 ± 7
78	41 ± 7	41 ± 7	86 ± 7	86 ± 7
79		39 ± 7		81 ± 7
80	36 ± 7	36 ± 7	77 ± 7	77 ± 7
81		33 ± 7		71 ± 7
82	30 ± 7	30 ± 7	66 ± 7	66 ± 7
83		28 ± 7		62 ± 7
84	26 ± 7	26 ± 7	58 ± 7	58 ± 7
85		25 ± 7		53 ± 7
86	24 ± 7	24 ± 7	177 ± 7	49 ± 7
87		23 ± 7		45 ± 7
88	22 ± 7	22 ± 7	41 ± 7	41 ± 7
89		22 ± 7		39 ± 7
90	21 ± 7	21 ± 7	37 ± 7	37 ± 7
91		21 ± 7		36 ± 7
92	21 ± 7	21 ± 7	35 ± 7	35 ± 7
93		21 ± 7		34 ± 7
94	22 ± 7	22 ± 7	32 ± 7	32 ± 7
95		22 ± 7		27 ± 7
96	22 ± 7	22 ± 7	23 ± 7	23 ± 7
97		22 ± 7		23 ± 7
98	22 ± 7	22 ± 7	23 ± 7	23 ± 7
99		22 ± 7		23 ± 7
100	22 ± 7	22 ± 7	23 ± 7	23 ± 7

Figure appendix

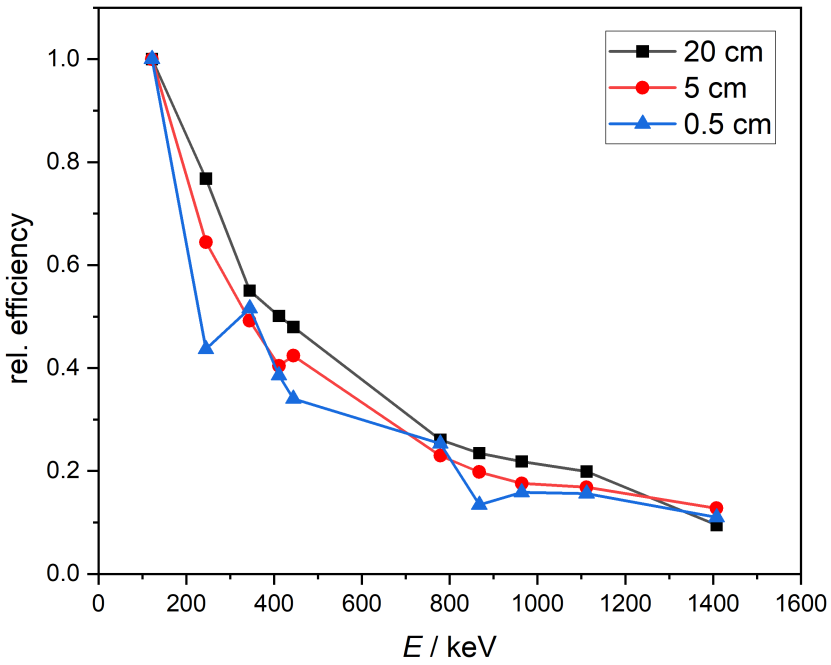

Figure 7.1: Releative efficiencies of the HPGe-detector (ORTEC, GMX20P4-70) used in the thermochromatography experiments at different distances to the detector (measured by Jochen Ballof, GSI).

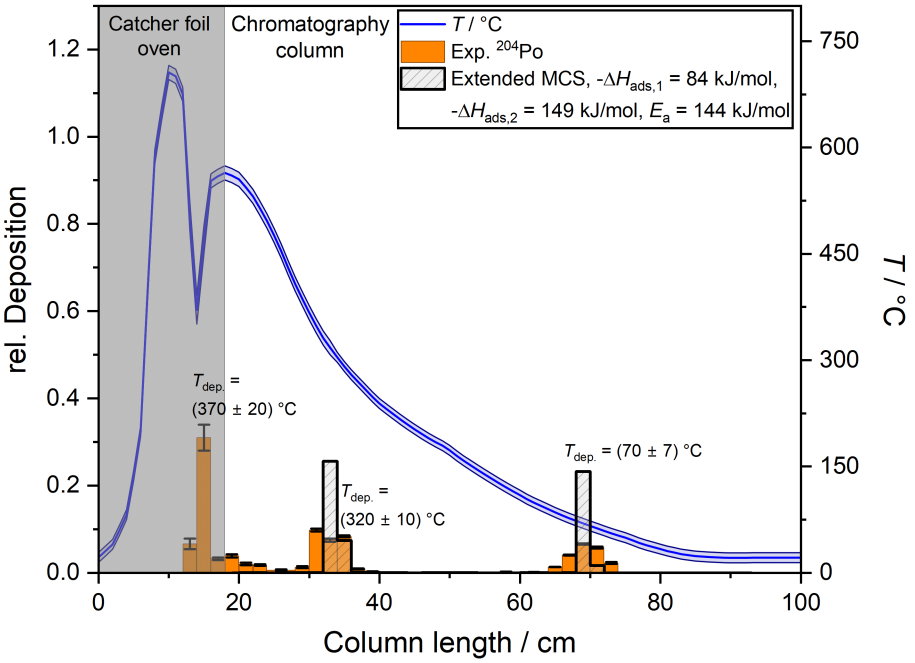

Figure 7.2: Thermochromatogram of the deposition of ^{204}Po (the 885 keV γ-line with an intensity of 29.9% has been analysed) on quartz glass without pre-treatment in helium and hydrogen atmosphere. The experimentally measured deposition is shown in orange, the simulated deposition using the extended Monte Carlo method by D. Dietzel is shown hatched and grey and the temperature is shown in blue.[65] The deposition temperature in the column was determined on the basis of the peak maximum, the deposition temperature of the peak between the catcher foil furnace and the chromatography column corresponds to the temperature minimum. No activity was measured in the filter downstream of the column. Here, E_a corresponds to the energy barrier between physisorption and chemisorption.

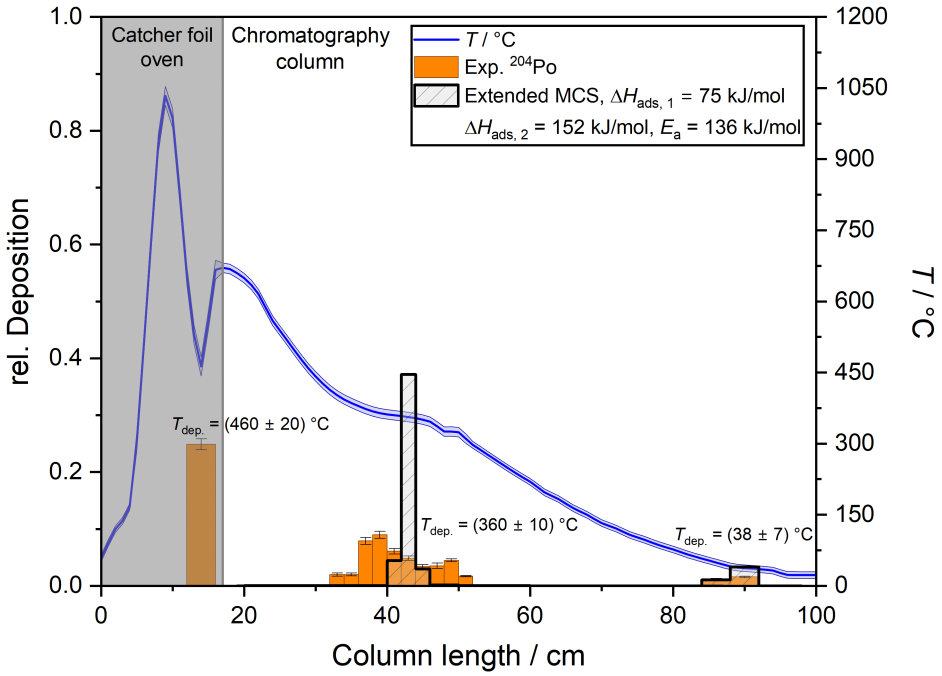

Figure 7.3: Thermochromatogram of the deposition of ^{204}Po (the 885 keV γ-line with an intensity of 29.9% has been analysed) on quartz glass without pre-treatment in helium and oxygen atmosphere. The experimentally measured deposition is shown in orange, the simulated deposition using the extended Monte Carlo method by D. Dietzel is shown hatched and grey and the temperature is shown in blue.[65] The deposition temperature in the column was determined on the basis of the peak maximum, the deposition temperature of the peak between the catcher foil furnace and the chromatography column corresponds to the temperature minimum. No activity was measured in the filter downstream of the column. Here, E_a corresponds to the energy barrier between physisorption and chemisorption.